Stony Brook University

Development and Characterization of High-Resolution Modular PET Imaging Systems

A Dissertation Presented

by

Michael Budassi

to

The Graduate School
in Partial Fulfillment of the
Requirements
for the degree of

Doctor of Philosophy
in

Biomedical Engineering

Stony Brook University

August 2015

Stony Brook University

The Graduate School

Michael Budassi

We, the dissertation committee for the above candidate for the
Doctor of Philosophy degree, hereby recommend
acceptance of this dissertation.

Paul Vaska, Ph.D. - Dissertation Advisor

Professor, Department of Biomedical Engineering, Stony Brook University

Terry Button, Ph.D. - Chairperson of Defense

Associate Professor, Department of Biomedical Engineering, Stony Brook University

David J. Schlyer, Ph.D.

Professor, Department of Biomedical Engineering, Stony Brook University

Craig Woody, Ph.D.

Senior Physicist, Physics Department, Brookhaven National Laboratory

This dissertation is accepted by the Graduate School.

Charles Taber

Dean of the Graduate School

Abstract of the Dissertation

Development and Characterization of High-Resolution Modular PET Imaging Systems

by

Michael Budassi

Doctor of Philosophy

in

Biomedical Engineering

Stony Brook University

2015

Engineering in positron emission tomography contains within it a design for its application. The compact modular detector technology used in the Rat Conscious Animal PET (RatCAP) is specifically designed for awake rat imaging, but is versatile enough for its use in the construction of different preclinical systems. PET scanners based on the RatCAP system include the PET Insert for PET / MR Studies, the Whole-Body Rodent PET Scanner, the BNL PET Imaging System for Plant Science, and the Wrist PET Scanner. This dissertation concerns the development and characterization of these scanners, both specific to their particular use, and common in their architecture. A discussion of the signal processing hardware, and the data acquisition and processing methods that accompany it, designed to be robust and unified across all imaging systems, is included. These advances are applied for the calibration of each scanner, enabling the creation of images that contain quantitative information on various physiological functions. In addition, the performance of the Plant Scanner is evaluated, and examples from imaging studies using our scanners are shown.

Dedicated to my mother, father, and sister.

Table of Contents

List of Figures

List of Tables

List of Abbreviations

RatCAP	Rat Conscious Animal PET
PET	Positron Emission Tomography
APD	Avalanche Photodiode
PMT	Photomultiplier Tube
SiPM	Silicon Photomultiplier
MRI or MR	Magnetic Resonance Imaging
BNL	Brookhaven National Laboratory
ASIC	Application Specific Integrated Circuit
LYSO	Lutetium Yttrium Oxyorthosilicate
FPGA	Field Programmable Gate Array
BNL-UPenn	The Whole-Body Rodent PET Scanner, developed in BNL with collaboration from the University of Pennsylvania
TSPM	Timestamp and Signal Processing Module
FOV	Field of View
RF	Radio Frequency
DAC	Digital-to-Analog Converter
LLD	Lower Level Discriminator
DAQ	Data Acquisition
PCI	Peripheral Component Interconnect
SFP	Small Form-Factor Pluggable
BASH	Bourne Again Shell
CERN	European Organization for Nuclear Research
PLL	Phase Lock Loop
UDP	User Datagram Protocol
TTL	Transistor-Transistor Logic
RCDAQ	Remote Call Data Acquisition
PHENIX	Pioneering High Energy Nuclear Interaction Experiment
PRDF	PHENIX Raw Data Format
PMonitor	PHENIX Monitor

GUI	Graphical User Interface
LOR	Line of Response
MLEM	Maximum Likelihood Expectation Maximization
OSEM	Ordered Subsets Expectation Maximization
MAP	Maximum A Posteriori
STIR	Software for Tomographic Image Reconstruction
OSMAPOSL	Ordered Subset version of the Maximum A Posteriori One Step Late algorithm
LZO	Lempel–Ziv–Oberhumer
SPI	Serial Programming Interface
PSF	Point Spread Function
FWHM	Full Width at Half Maximum
SVD	Single Value Decomposition
NECR	Noise Equivalent Count Rate
SNR	Signal-to-Noise Ratio
SimSET	Simulation System for Emission Tomography
^{18}F-FDG	Fluorine-18 Radiolabeled Fludeoxyglucose
SPIO	Superparamagnetic Iron Oxide
FIFO	First-in-first-out
I.V.	Intravenous
I.P.	Intraperitoneal
S.C	Subcutaneous
I.T.	Intrathecal

Acknowledgements

The RatCAP project is an effort that spans over a decade of research and engineering from many brilliant, hard-working scientists, engineers and collaborators. It has been a privilege for me to work with them, and to learn from them. I hope that my contribution will continue to serve the members of this group, old and new. In particular, I would like to thank:

My advisor, Dr. Paul Vaska, for guiding me through this exciting world of medical imaging research, with patience and resourcefulness; Dr. David Schlyer for showing me the potential of PET across the many fields of scientific inquiry; Dr. Craig Woody for making the investigative rigor of the PHENIX experiment the standard in our group; The committee chair, Dr. Terry Button, for being my first teacher in medical physics, and helping me throughout my graduate school years; Sean Stoll, for his invaluable help with everything from technical shop skills to high-energy physics; Jack Fried, for being the digital engineer par excellence who always had the answer; Dr. S. David Smith, for making the many possibilities of multi-modality imaging a reality, ready for application; Dr. Martin Purschke, to whom I owe my entire understanding of computer programming, software engineering, and everything in between; The graduate students past and present, Dr. Sri Lalan Krishnamoorthy, Dr. Sri Harsha Maramraju, Dr. Bosky Ravindranath, Dr. J-F Pratte, Dr. Sudeepti Southekal, Michael Salerno, David Ouellette, Bharat Kapoor, and Tuoyu Cao, whom I am proud to call labmates.

I would also like to thank our many collaborators: Dr. Benjamin Babst, Dr. Richard Ferrieri, Dr. Michael Schueller, and David Alexoff for their help with the Plant Scanner studies; Dr. Helene Benveniste, Dr. Hedok Lee, and Mei Yu for their help with the PET-MR studies; Dr. Sergio Rescia, Howard Hansen and Ron Angona for their help with RF coil development; Dr. Daniela Schultz and Dr. Eugenia Gold for their collaboration in the bird and rat studies using the RatCAP; Dr. Sven-Erik Strand and Dr. Renata Madru for their collaboration in the mouse studies using the PET Insert; Dr. Joel Karp, Dr. Eugene Gualtieri, Dr. Stephen Pickup, and Eric Blankemeyer for their collaboration in the Whole-Body Rodent PET studies; Dr. Richard Carson and Dr. Stephanie Groman for their collaboration in the maze studies using the RatCAP. Dr. Peter Thanos, Lisa Robison, and Melissa Vitale for their collaboration in the Ritalin studies using the RatCAP.

I would like to thank Çağla Taşdemir for her inexhaustible kindness and support. Finally, I would like to thank my family: my mother Alicia, my father Marcelo, and my sister Julia: With love and gratitude, this thesis is dedicated to them.

1. PET Physics and Instrumentation

1.1 INTRODUCTION

The successes in positron emission tomography (PET) have lead engineers not only to explore the improvement of the image modality, but to test its versatility in different dedicated functions. Compactness and compatibility with other modalities became desirable as new applications for PET were discovered, and newly developed technologies made them possible. The scintillation block detector addressed the issues attributed to the unwieldy light guides of early PET scanners[1]. The avalanche photodiode (APD) made it possible for one-to-one coupling with scintillator crystals in the millimeter scale and, unlike its photomultiplier tube (PMT) predecessor, can function within a magnetic resonance imaging (MRI) scanner[2].

In Brookhaven National Laboratory (BNL), an application specific integrated circuit (ASIC) was designed for a new miniature PET scanner designed for awake animal imaging[3,4]. The scanner uses Lutetium Yttrium Oxyorthosilicate (LYSO) scintillator block detectors, consisting of an array of 4x8, 2.22x2.22 mm discrete crystals that are one-to-one coupled with a Hamamatsu S8550 APD array. The crystal pitch for each discrete detector is 2.3 mm, and the packing fraction for the block detector is 0.93. Each detector module is read out by the custom made ASIC, which transmits its data to a field programmable gate array (FPGA) based communication module, known as the time stamp and signal processing module (TSPM), responsible for recording and packaging the singles list-mode data for the data acquisition computer[5].

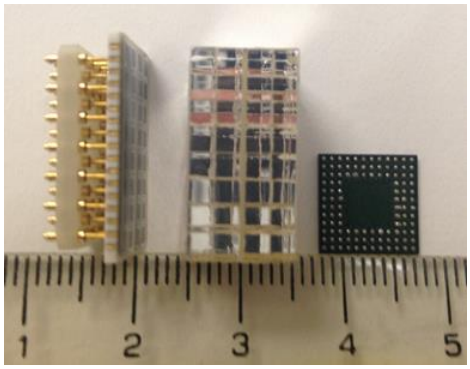

Figure 1: The Hamamatsu S8550 APD array, LYSO scintillator block, and custom ASIC

Expanding from its original use, the front-end electronics developed for the Rat conscious animal PET became a building block for other related scanners and applications. Because the architecture of the RatCAP based systems were similar, the data acquisition and processing firmware and software had the potential to work with the variety of associated scanners, and to be easily adaptable for any future versions or variations.

The current list of RatCAP based scanners include the PET Insert for simultaneous PET / MR Studies[6], the Whole-Body Rodent PET Scanner (abbreviated as the BNL-UPenn System because of the collaboration between BNL and the University of Pennsylvania)[7], the BNL PET imaging system for plant science[8], and the BNL Wrist Scanner[9]. (The BNL Breast PET System[10] prototypes have been repurposed as the wrist and plant scanners). The RatCAP and PET Insert both use one flexible circuit, which is rolled to form the detector gantry. The Plant Scanner and Wrist Scanner are comprised of two flexible circuits, but the Plant Scanner leaves an opening between the circuits, creating a slightly wider field of view (FOV). This gap is interpreted as a pair of virtual blocks during data processing. The base of the BNL-UPenn System is an annular motherboard, upon which 24 modular tower boards are connected, each tower board containing four block detectors. A summary of the systems' components and dimensions can be found in table 1.

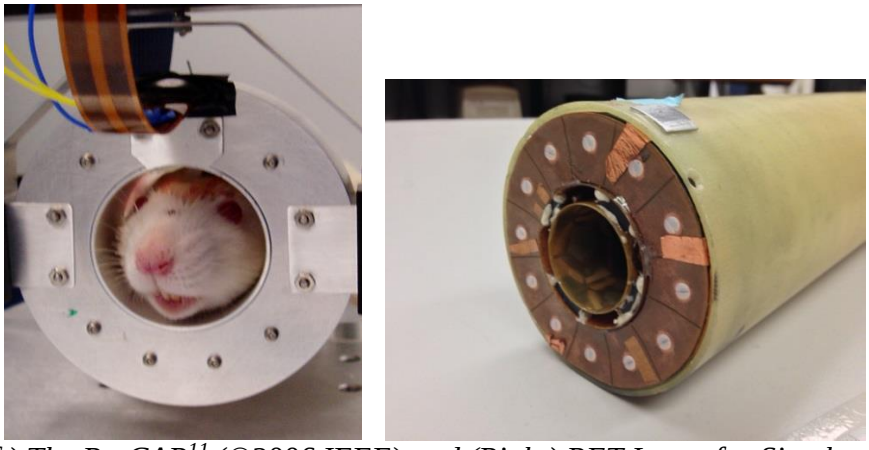

Figure 2: (Left) The RatCAP[11] (©2006 IEEE) *and (Right) PET Insert for Simultaneous PET/MR*

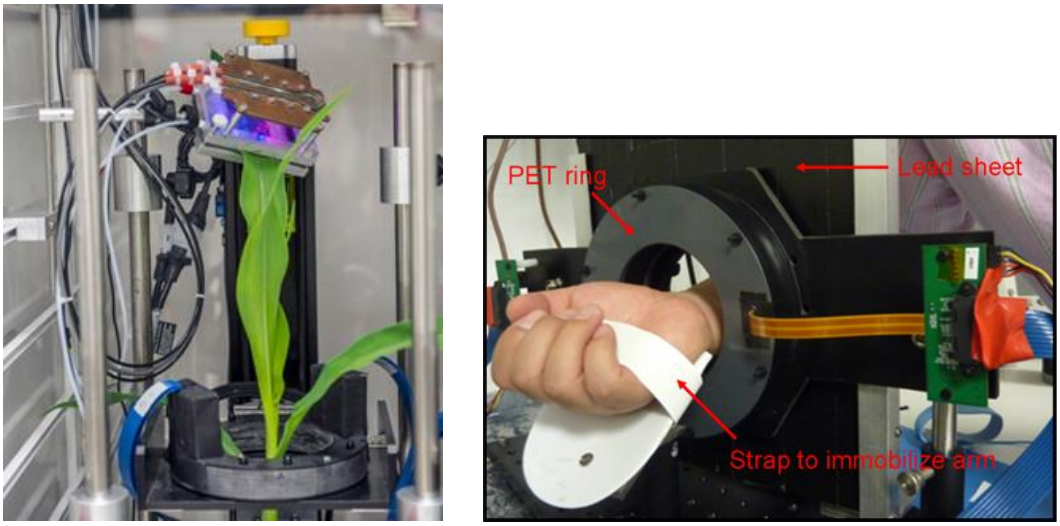

Figure 3: The BNL PET Imaging System for Plant Science, and the BNL Wrist Scanner[9] (©2009 IEEE)

Figure 4: The Whole-Body Rodent PET Scanner (BNL-UPenn System)[7] (©2012 IEEE)

	Number of Detectors	Number of Crystals	Axial FOV (mm)	Transaxial FOV (mm)	Crystal Length (mm)
RatCAP	12	384	18	38.4	8
PET Insert	12	384	18	44*	5
Wrist Scanner	24	768	18	100.8	20
Plant Scanner	26**	832**	18	112	15
Whole Body Rodent Scanner	96	3072	50	153	14

* Transaxial FOV with RF coil: 32 mm

** 2 virtual block detectors, 64 virtual crystals

Table 1: Summary of dimensions and components for PET systems

Except for the BNL-UPenn System, which directly connects to its four TSPMs, communication between the front end electronics and the TSPM is issued through a low voltage

differential signaling (LVDS) ribbon cable, made by Samtec. The high voltage (300–500V) required for the detector APDs is provided by two power sources, each comprising a rail of each detector module voltage divider, allowing the user to fine tune the gain for every block detector.

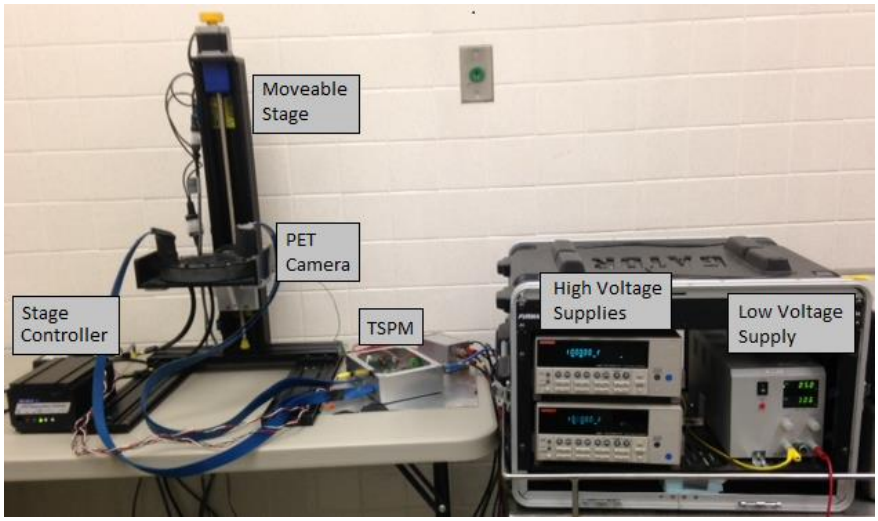

Figure 5: System setup for the Plant Scanner

The purpose of the study is to develop quantitative data acquisition and processing methods that are robust and unified across all systems, and to evaluate the performance of the scanners. The following will discuss the advances of the scanners and their software, and the characterization of the Plant Scanner PET System.

1.2 BASICS OF PET

1.2.1 What is PET?

Medical research, at its most fundamental, requires an understanding of the chemical interactions within physiological systems. The details of these interactions are often unseen and difficult to infer, especially without invasive means or methods that alter the chemical properties of the substances in question. In 1922, Georges de Hevesy circumvented these limitations through the use of radioactive materials, in an experiment which became the first use of radiolabeled tracers. The advantage of using radioactivity was that the physiological processes within an organism do not differentiate between the radioactive and stable isotopes of the same compound. It is possible then to label a given compound with radioactivity, so that its movement and distribution throughout the subject can be studied. In the case of de Hevesy, ^{212}Pb was used to study the uptake of lead nitrates in plants.[12] This tracer principle attained clinical relevance two years later, when Hermann Blumgart injected a solution of ^{214}Bi into a subject's arm and determined the speed the tracer took to reach the other arm[13].

The decay modes of the radionuclides would determine the way the tracers were detected. A positron, discovered by Carl Anderson in 1932, is emitted by some proton rich unstable atoms in beta plus decay, along with a neutrino. It is the positively charged, antimatter counterpart of the electron, which, once losing most of its kinetic energy, can interact with an electron to momentarily form a positronium, before the combination loses all its mass in an annihilation reaction. The products of annihilation are two gamma photons, both 511 keV as dictated by mass-energy equivalence, emitted nearly 180^{o} apart[14].

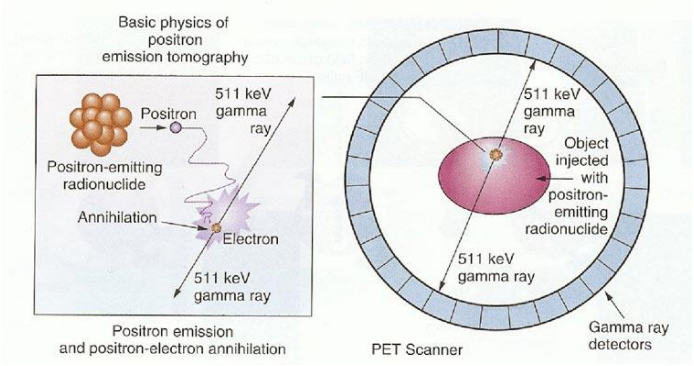

Figure 6: Positron Annihilation, and the detection of 511 keV photons within a PET camera[15]

The use of positron emitting radionucleotides is the basis of positron emission tomography. It implements a growing set of image reconstruction tools to determine the origin of the detected annihilation photons, so that the distribution of the radiotracer can be mapped in three dimensions. Improvements in radiochemistry have allowed investigators to label a variety of compounds for researching specific pathways in organisms with the aid of PET. Currently, the most popular PET tracer for clinical purposes is the glucose analog 2-Fluoro-2-deoxy-D-glucose (FDG), which uses the positron emitting ^{18}F for tracking tissue metabolism in tumors in cancer patients[16], the brain in psychological studies[17], and other areas of interest for the physician or medical scientist.

1.2.2 Coincidence Events

The PET scanner must be able to discriminate between the photons of annihilation reactions from spurious noise which may impoverish the quality of the image, while accurately identifying the location of the radiotracer in the subject. The simultaneous detection of two photons in different detectors is called a coincidence event, and it may contain positioning information that can later be used to create a tomographic image. In this instance, the coincidence event is qualified as a true coincidence, and the origin of the annihilation event is said to have occurred somewhere between the two detectors, on a line of response (LOR). However, a coincidence may instead contain erroneous information due to limitations, some unavoidable, in the imaging system.

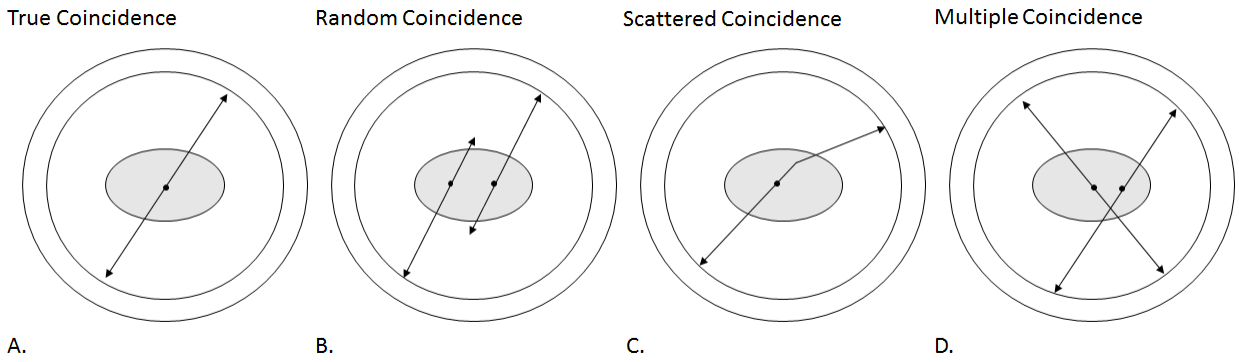

Figure 7: Different types of coincident events. Examples B, C, and D show instances of coincidences that do not accurately reflect the distribution of activity within the FOV

The detection of two photons, or two single events, is considered a prompt coincidence event if the photons are detected within a given amount of time of one another, known as the timing window. The timing window is set according to the time resolution of the system, and must be wide enough to accept true coincidences, while narrow enough to avoid interpreting photons from unrelated annihilation reactions as prompt coincidences. The latter case is an example of a random, or accidental, coincidence, and if unaccounted for, can result in a background of activity in the reconstructed image that is not reflective of the tracer distribution. If the count rate of the individual detectors is known, the random event count rate between two detectors can be calculated by:

$$2\tau N_1 N_2$$

Where 2τ is the width of the timing window, and N_1 and N_2 are the singles count rates of the two detectors[18].

The other two kinds of undesirable coincidence events are multiple and scatter coincidences. A multiple coincidence is the detection of more than two photons within the same time window. Because a LOR cannot be drawn between three or more detection sites, a multiple coincidence cannot contain valid positioning information[19]. Whereas a multiple coincidence can be found and removed from the data during processing, a scatter coincidence, like an accidental coincidence, cannot immediately be distinguished from a true coincidence. A scatter coincidence occurs when either one or both photons from an annihilation event change direction before detection. In this case, the assumption that the origin of an event occurs on a LOR between two detectors would be incorrect, and the failure to correct for scatter coincidences will result in an inaccurate distribution of activity in the final image[20].

1.2.3 Interactions of Light with Matter

511 keV gamma photons that change direction in the media after emission are the often result of a phenomenon known as Compton scatter. It occurs when a photon interacts with a loosely bound valence electron of an atom, and transfers a part of its energy to the electron, thereby causing the photon to change direction as dictated by the conservation of momentum.

The energy of the scattered photon is dependent on the scatter angle, as shown in following formula:

$$E_{sc} = \frac{m_e c^2}{\frac{m_e c^2}{E_o} + 1 - \cos\theta}$$

Where m_e is the mass of an electron, E_o is the energy of the photon before scatter, E_{sc} is the energy of the photon after scatter, c is the speed of light ($3 * 10^8$ m/s) and θ is the scattering angle[21].

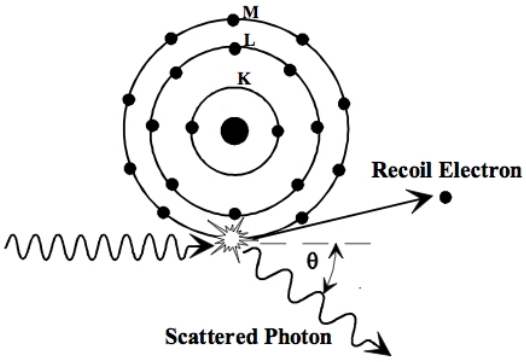

Figure 8: An example of Compton scatter, showing the interaction between an incident photon and the outer electron shells of a Bohr atomic model. The transfer of energy from the photon to a valence electron changes the direction of the photon[22]

Although Compton scatter is the dominant form of interaction of photons in tissue, and the primary component in the attenuation of gamma rays within tissue, another form of interaction that makes a smaller contribution to light attenuation is the photoelectric effect. In this phenomenon, the photon is completely absorbed by an atom in the medium, and transfers all of its energy to one of its orbital electrons. The electron is then ejected, and the remaining vacancy is filled by an outer orbital electron. The energy released by the electron falling into a lower energy state, along with the ejected electron, are often reabsorbed into the media[23].

Together, the attenuation coefficient (μ) due to Compton scatter and the photoelectric effect make up the linear attenuation coefficient, which can be used to determine the photon flux *I* of gamma rays passing through a given thickness of specific media *x*:

$$I(x) = I(0)e^{(-(\mu_{compton}+\mu_{photoelectric})x)}$$

An increase in the photon energy E results in a decrease both in the photoelectric component, proportional to E^3, and the Compton component, proportional to E. At certain energies, the photoelectric component shows a sudden increase, corresponding to the orbital

electron binding energies for specific atoms. Once the photon energy reaches 1.022 MeV, the pair-production component begins to contribute to the attenuation coefficient, and at higher energies, it becomes the dominant form of interaction. In this phenomenon, the photon interacts with an atom's electric field to create a positron-electron pair, with a kinetic energy equal to the remaining energy left after the rest mass energy of particle pair (2 x 511 keV = 1.022). Since PET involves the 511 keV photons created from the annihilation reactions of positrons emitted from radioactive atoms, the high energy photons needed for pair production interactions are less relevant in our attenuation calculations[24].

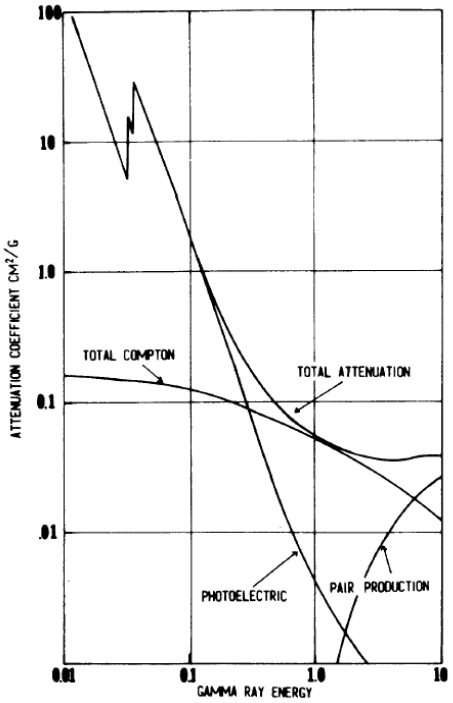

Figure 9: Attenuation coefficient as a function of photon energy for the CsI(Na) scintillator[25] (©1967 IEEE)

When determining the probability of photon detection in PET studies, the attenuation of light is calculated from the origin of the annihilation to the detector site (shown as *x* in the following equation). However, because the collection of PET data is only concerned with coincidences, the probability must include both photons[26], thus simplifying the attenuation distance to the length of the line of response *D*:

$$P_{det} = \left(e^{(-\mu x)}\right)\left(e^{(-\mu(D-x)}\right) = e^{(-\mu D)}$$

1.2.4 Components of PET

In most PET scanners, the photons that reach the detector are absorbed by a scintillator. Scintillators used in PET imaging are dense, inorganic crystalline materials which reemit the energy received from gamma photons in the form of visible light. The light emitted after excitation, known as florescence, quickly rises to a maximum intensity and decays exponentially, as defined by the scintillator's decay time constant. The effectiveness of a scintillator is determined by the crystal's ability to stop incoming annihilation photons and quickly reemit light that can pass through the crystal without being reabsorbed. Scintillators that majorly interact with light in the 511 keV range through the photoelectric effect, and have short decay constants are good candidates for detector designs. In addition, longer, denser crystals provide more attenuating thickness for photon absorption[27].

A longer decay constant will have a deleterious effect on the PET system time resolution because the time window must be widened correspondingly; Scintillators with low light output and slower emission times require longer detection times and can introduce statistical variation in the photodetector, necessitating more time in between single events to determine whether they are coincidental. As a result, a wider time window can increase the chance that photons from separate annihilation events will comprise a true coincidence. Conversely, high light output and a short decay constant results in an improved time resolution, a narrow time window, and a better signal-to-noise ratio (SNR). Even with the fastest possible scintillator however, the time resolution is ultimately limited by the travel time of gamma photons within the FOV of the scanner: if the tracer is closer to one edge of the scanner, one of the gamma rays must reach the opposite edge before the coincidence pair is detected[28].

	Sodium Iodide	Bismuth Germanate	Lutetium Oxyorthosilicate	Gadolinium Oxyorthosilicate	Barium Fluoride
	NaI(Tl)	BGO	LSO	GSO	BaF_2
Density (g/cc)	3.67	7.13	7.40	6.71	4.89
Effective atomic number Z	51	76	65	59	53
Decay constant (ns)	230	300	47	56	0.6, 630
Index of refraction	1.85	2.15	1.82	1.85	1.56
Light output (photons per 511 keV)	19400	4200	13000	4600	700, 4900
Linear attenuation at 511 keV	0.34	0.96	0.88	0.70	0.45
Ratio between photoelectric and compton	0.22	0.78	0.52	0.35	0.24

Table 2: Properties of scintillators used in PET[27,28]

Table 2 describes some of the scintillators most commonly used in PET. For a given photon energy, the photoelectric component of attenuation is proportional to the cube of the

atomic number Z of the absorber, while the Compton component only has a first-power relation[24]. A scintillator with higher effective atomic number is then generally preferred because of its superior absorption of 511 keV photons, while showing a smaller relative increase in scatter.

The critical angle:

$$\sin^{-1}\frac{n_1}{n_0}$$

Where n_0 and n_1 are the indices of refraction of the scintillator and surrounding medium respectively, is the angle above which light is completely reflected, and below is only partially reflected as it approaches zero. Though the reflection of escaping florescent light back into the scintillator is desirable, the reflection of reemitted light passing into the photon counter must be minimized to avoid diminishing the signal; it is for this reason that a smaller index of refraction is preferred. Reflector material around and between the detector crystal elements can be added to help direct light into the photodetector.

The fluorescent light from the scintillator is received by a photodetector, where it is converted into an electrical signal. The most popular photodetectors in PET are photomultiplier tubes and avalanche photodiodes. When coupling PMTs to a scintillator, the discrete crystals of the scintillator block are usually shared among a fewer number of PMTs (figure 12 shows four PMTs coupled to a scintillator block, known as light sharing)[29]. However, the ability to divide an APD into an array of smaller elements can allow for one-to-one coupling in APD based scanners.

The older of the technologies, the PMT, consists of a vacuum tube with an applied electric field. In a PMT, the scintillator photon hits the photocathode, which releases a photoelectron that accelerates in the direction of the field. The photoelectron is then multiplied with each successive positively charged electrode, or dynode, it strikes, until the collection of electrons reaches the anode, where a current is produced. The result of the emission of electrons from each dynode is an amplification of the signal by a factor exceeding 10^6. The main limitation of this technology is the efficiency of the photocathode, known as the quantum efficiency, which can be as low as 25%. In addition, PMT based PET detectors are incompatible with MRI, and require light guides to transmit the output of the scintillator to the PMT outside the magnet bore[28].

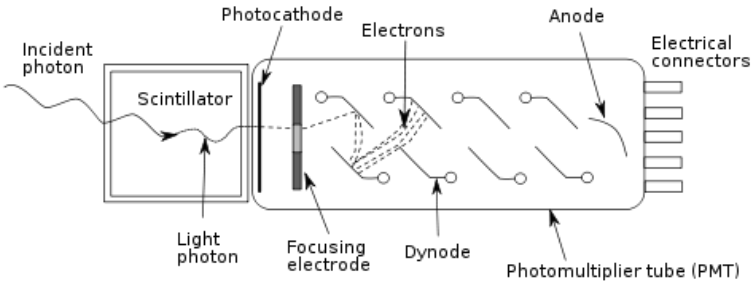

Figure 10: Diagram of photomultiplier tube[30]

An APD works by releasing an electron when a photon strikes the silicon entrance window, which collides with other silicon atoms while moving towards the cathode. The absorption of the photon in the entrance window initially produces one electron-hole pair. The released electron then drifts towards the multiplication region, where the high electric field pulls electrons to the n side of the p-n junction, and the holes are pulled to the p side. The pull on the released electron causes it to accelerate, causing impact ionizations with other silicon atoms and creating more electron-hole pairs. When the released electrons finally reach the cathode, they generate an amplified signal with much higher gain[26]. Because of the high voltage generating the field across the photodiode, the gain can increases by a factor of 10^2 to 10^3. Recently, the silicon photomultiplier, which operates as an array of silicon APDs in Geiger mode, has garnered interest because of its superior detection efficiency and timing response[31].

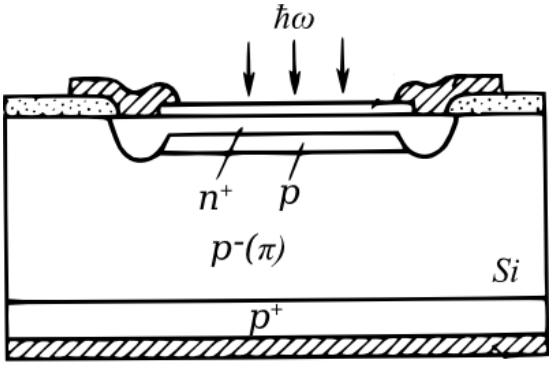

Figure 11: Diagram of an avalanche photodiode[32]

The signal produced by photodetector is proportional to the amount of light emitted by the scintillator, which in turn is proportional to the gamma photon energy. The energy resolution of a system is the measure of its ability to determine the energy of the detected gamma photons. In a PET system with ideal energy resolution, an energy spectrum generated from the detection of annihilation photons from a positron emitter would reveal a narrow photopeak of 511 keV.

However, the statistical fluctuations in converting the deposited photon energy into a signal widens the photopeak, and Compton scatter within the FOV and detectors contaminates the lower energies of the spectrum. For this reason, an energy window is employed, rejecting signals from photons above and below the specified energy thresholds. A PET system with poor energy resolution cannot effectively discriminate between different photon energies, and often uses a wider energy window to capture true coincidences. Such a setup is more likely to also accept photons which have lost energy in scatter reactions[33].

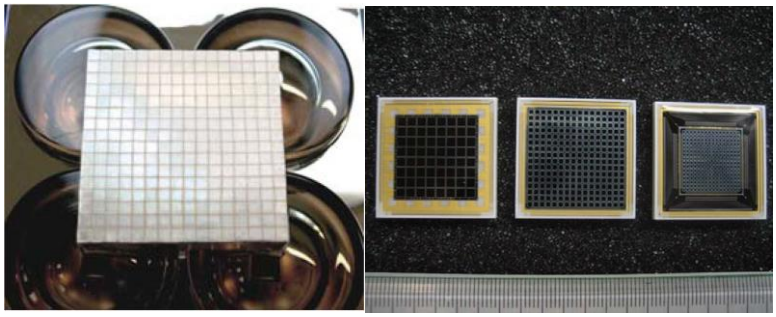

Figure 12: Examples of photon counters: (Left) Four photomultipier tubes coupled to PQS block detector[29] (©2012 IEEE) *(Right) Avalanche photodiodes[34]* (©2009 IEEE)

Individual detector modules, comprised of scintillators blocks coupled to photodetectors, can be assembled into a ring and surround the imaging subject, permitting the detection of coincidences from every angle (known as complete sampling). Other configurations involve the use of several flat panels of detectors that enclose or rotate around the subject. The blocks can be divided into discrete elements, enabling the assignment of projection bins to each LOR, which becomes essential for image reconstruction. The axial FOV is lengthened with the addition of more rows of detector rings, either by using more detector blocks, or using detector blocks that are cut to include more elements in the axial direction[28].

The photodetector signal is read by a data acquisition system, which records the time, position, and, depending on the front-end, energy information about the detected photon. The system may take the information of every detected photon, or apply a coincidence logic circuit, which determines whether the signal is part of a coincidence before saving it within the data.

1.3 PROJECTION DATA AND IMAGE RECONSTRUCTION

1.3.1 Data Sampling and Binning

Coincidence information is either written out in listmode or as a collection of sinograms. In listmode, the time of the coincidence, along with the location of the detectors is written out as a series of inputs for further processing. Listmode data can be later reprocessed into the latter form of recording coincidences, the sinogram, which is a graphical representation of detected activity. The sinogram plots prompt and random coincidences according to the projection angle across the scanner FOV, and the radial offset from each projection center[35].

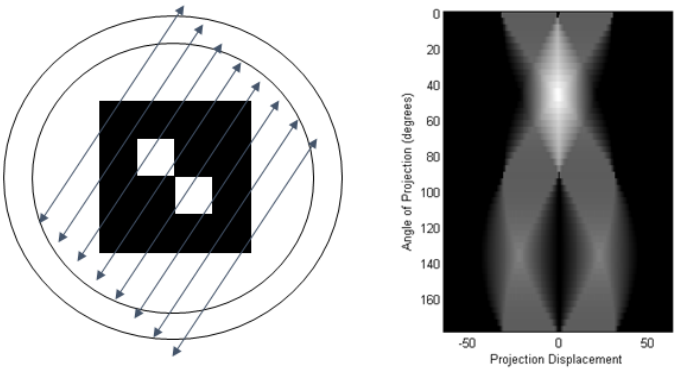

Figure 13: (Left) Parallel lines of response for a given projection angle. (Right) Sinogram, representing projection data from each angle[36]

The total number of projections depicted in a sinogram encompass 180^{o} of the scanner, accounting for the total possible number of pairs of detectors involved in coincidence detection. The sinogram, with azimuthal angle ϕ and radial offset r, relates to a coordinate x,y map of activity in the scanner FOV by the following[37]:

$$r = x\cos\phi + y\sin\phi$$

The set of parallel LORs drawn across directly opposing detectors at a given projection angle make up the number of radial samples for that angle; each successive LOR from one edge of the scanner to the other is plotted with an increasing radial offset. Although the samples are assumed to be equidistant from each other, the LORs at the scanner's edge are often closer to one another than in the center, due to the diminishing view of detector faces at the given angle. To increase the radial sample rate, quasi-parallel lines of response can be included among the strict

parallel lines of response. This process, known as interleaving, involves a detector forming a LOR both directly across the FOV (parallel), and with the detector adjacent (quasi-parallel) to the direct projection[38].

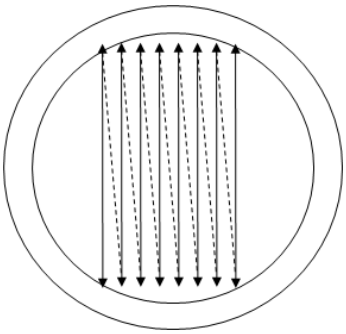

Figure 14: Example of interleaving

In strict 2D mode, recorded coincidences can only take place on different projections within the same ring of detectors, limiting the axial samples, and the number of sinograms, to the number of direct axial planes. The number of axial samples can be increased by considering the coincidences between rings of detectors on different planes, thus forming cross planes at different polar angles θ. In full 3D mode, a sinogram is written for every direct and cross plane, setting number of sinograms equal to the square of the number of rings. The increase in recorded coincidences greatly improves the sensitivity, especially towards the axial center of the PET scanner, where many of the planes intersect. Overall, the switch from 2D to 3D can improve the scanner sensitivity by a factor of seven[39]. However, towards the axial edges, the sensitivity is about equal to 2D PET cameras, where only direct planes, or cross planes that go across adjacent detector rings.

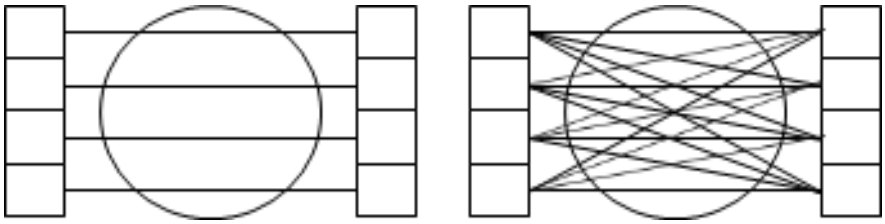

Figure 15: 2D and 3D PET acquisition

The advantages of 3D PET over 2D are offset by an increase in total amount of recorded noise. A higher sensitivity can impoverish the resolution, since the improved detection capability applies both to true and scattered coincidences. At the same time, an improvement in resolution

will often result in a lower sensitivity, since an attempt to reduce noise in the form of scatter and accidental coincidences can inadvertently reduce the signal as well.

The increase in amount of data due to these sampling methods has inspired space saving techniques. Sinograms from adjacent polar angles can be averaged into one sinogram, in an axial undersampling technique measured by the span. Similarly, the angular sampling can be truncated by transaxial mashing, which involves combining adjacent projection angles in the sinogram. The radial sampling rate is often too low for truncation, and is used as a baseline with which other undersampling techniques are based[37].

Ultimately, these recording methods are limited to projection data, which can only point activity to a LOR. In an attempt to narrow the activity distribution, time-of-flight PET addresses the issue of placing counts across a LOR for a single emission site by better approximating the origin of the annihilation photons. This is done by using the difference in arrival time of each of the coincident photons (Δt) to trace back where they were originally emitted:

$$\Delta d = \frac{\Delta t(c)}{2}$$

Where *c* is the speed of light and Δd is the distance from the point between the detectors. This requires that the scanner is able to detect time differences on the scale of 10^{-12} seconds, which may not possible for certain scintillators or photon detectors[40].

1.3.2 Image Reconstruction

Image reconstruction can be divided into two categories: analytic and iterative methods. Both these methods attempt to improve the linear superposition of backprojections, otherwise simply known as backprojection, which determines the pixel values of an image based on the projection values collected within the coincidence data. Alone, simple backprojection assigns a weighted value for each pixel within each LOR, for every projection angle in the data. The sum of the pixel values, divided by total number of projections, yields a blurred image of the activity distribution, its poor contrast a result of placing counts across a LOR, when the annihilation site encompasses only a point on the line[41].

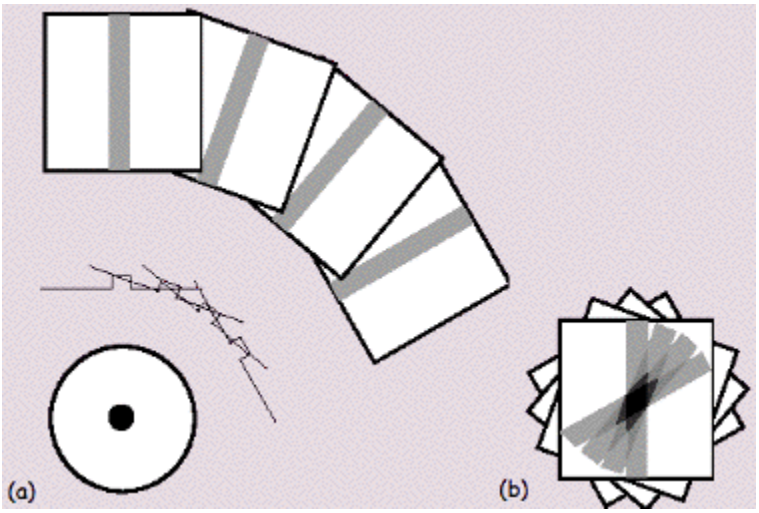

Figure 16: Back Projection: The sum of projection data (a) from four angles yields image (b)[42]

Analytic methods use different filters to improve the contrast of backprojection. The gold standard of analytical reconstruction techniques, filtered backprojection (FBP) maps the data of each projection angle into Fourier space, and applies filter functions to remove various interfering frequencies. The cut-off frequency sets the frequency limit in the Fourier transformed projection data, based on the highest image frequency that the system can reliably produce, known as the Nyquist frequency. Different filter functions apply different weights to the frequencies below the cut-off that balance the SNR and sensitivity to provide the best image. Figure 17 shows a number of filters that can be applied based on fractions of the Nyquist frequency[43].

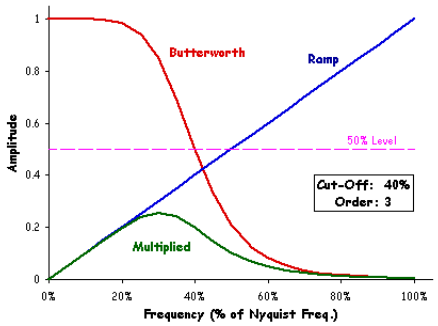

Figure 17: Examples of filter functions in FBP[44]

Iterative reconstruction, first developed for PET image formation by Shepp and Vardi[45] and Lange and Carson[46], involves the repeated transformation of the estimated activity within the FOV, as represented in a three dimensional image, onto the projection space, where it is compared against the coincidence data, and mapped back onto the image space. The projection

phase, known as forward projection, and the image mapping phase, known as back projection, make up the process of each iteration, which is repeated until the user is satisfied that the reconstruction algorithm has converged to an acceptable solution.

One of the most popular reconstruction methods is the application of the maximum likelihood expectation maximization algorithm (ML-EM). To attain the highest likelihood is to minimize the difference between the coincidence data and the projection of the image estimate, and each iteration of this algorithm produces an array of voxel values that maximizes the likelihood function. This requires a statistical model that accurately describes the probability distribution of radioactive decay and photon detection, both independent Bernoulli processes, to define the function[47].

The Poisson model is often used for this purpose, making the coincidence data a collection of independent Poisson random variables. The reconstruction then becomes a linear inverse problem, where the product of a matrix containing details regarding the PET system and a vector containing the voxel values yields the projection vector, set equal to the coincidence data. Each projection bin is equal to the sum of the voxels corresponding to that projection, with the details of each voxel described in the matrix[48].

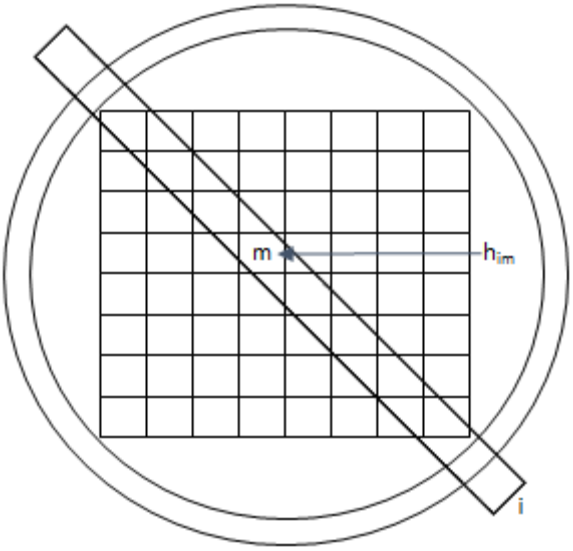

Figure 18: System matrix element h_{im} corresponds to the value in voxel m within the LOR i. The LOR is a line integral of the pixel values between the two given detectors

The matrix used in the problem is called a system matrix, and each of its element assigns a weight to each voxel in the image. The weighing factor is used to determine the voxel's contribution in a given LOR (If a voxel is not included in a particular LOR, the matrix element

for that voxel and projection bin is zero. Since a small fraction of an image's pixels make up one LOR, the system matrix is sparsely populated). The contribution of each voxel is determined for every LOR, making the dimensions of the matrix the total number of voxels by the total number of projection bins[45]:

$$g_i = \sum_m h_{im} f_m$$

Where g_i is the projection i, comprised of the sum of pixels m in image f. If the investigator has information regarding the detector efficiencies, or the attenuating properties within the scanned subject, then it can be included in the system matrix. By changing the weighing factors correspondingly, the various aforementioned effects can be considered in the scanner's ability to determine the tracer distribution in coincidence detection.

To derive the MLEM equation, we begin with the probability distribution of expected random photons detected in voxel *m* that contribute to a projection bin *i*, resulting in image **f**:

$$p(s; \boldsymbol{f}) = \prod_i \prod_m \frac{E[s_{im}]^{s_{im}} e^{-E[s_{im}]}}{s_{im}!}$$

Where *s* is the unknown complete data for the random photons. The expected value of s_{im} is then the product of the *m* voxel in the image, and the system matrix element in voxel *m*, projection bin *i*:

$$E[s_{im}] = h_{im} f_m$$

To ensure that the likelihood will be strictly concave, we take the natural logarithm of the probability distribution. (It is important that the likelihood is concave, so that each iteration approaches convergence.)

$$\ln p(s; \boldsymbol{f}) = \sum_i \sum_m [s_{im} \ln(h_{im} f_m) - h_{im} f_m - \ln(s_{im}!)]$$

We find the conditional expectation of the log-likelihood, given the actual coincidence data **g** and image estimate $\hat{\boldsymbol{f}}^{(n)}$:

$$\mathrm{E}[\ln p(s; \boldsymbol{f}) \mid \mathbf{g}; \hat{\boldsymbol{f}}^{(n)}] = \sum_i \sum_m [E[s_{im} \mid \mathbf{g}; \hat{\boldsymbol{f}}^{(n)}] \ln(h_{im} f_m) - h_{im} f_m - E[\ln(s_{im}!) \mid \mathbf{g}; \hat{\boldsymbol{f}}^{(n)}]]$$

We calculate the conditional expectation of random photons emitted in a voxel *j*, projection bin *i*, that contribute to the projection bin *i*, given the total number of current voxel

estimates and the actual coincidence data (treating the combined Poisson distribution as a multinomial distribution):

$$E[s_{ij} | \mathbf{g}; \hat{\boldsymbol{f}}^{(n)}] = \frac{h_{ij}\hat{f}_j^{(n)}}{\sum_k h_{ik}\hat{f}_k^{(n)}} g_i$$

This marks the end of the expectation step, which uses the data and current image estimate to create the likelihood function. The next step, known as the maximization step, finds the next image estimate that yields the highest value for that function. We set the partial derivative of the conditional expectation, with respect to the voxel values *j*, to zero, so that we can solve for the new parameter that maximizes the log-likelihood:

$$\frac{\partial(\mathrm{E}[\ln p(s; \boldsymbol{f}) \mid \mathbf{g}; \hat{\boldsymbol{f}}^{(n)}])}{\partial f_j} = 0 = \sum_i (E[s_{ij} | \mathbf{g}; \hat{\boldsymbol{f}}^{(n)}] \frac{1}{\hat{f}_j^{(n+1)}} - h_{ij})$$

Finally, the equations are combined and rearranged into its common form, and iterated for every voxel:

$$\hat{f}_j^{(n+1)} = \frac{\hat{f}_j^{(n)}}{\sum_i h_{ij}} \sum_i h_{ij} \frac{g_i}{\sum_k h_{ik}\hat{f}_k^{(n)}}$$

In practice, the denominator of the second term makes up the forward projection phase, finding the sum of the current voxel estimates. It is in this calculation where the scatter (*S*) and random (*R*) coincidences are included:

$$\hat{f}_j^{(n+1)} = \frac{\hat{f}_j^{(n)}}{\sum_i N_i h_{ij}} \sum_i N_i h_{ij} \frac{g_i}{\sum_k N_i h_{ik}\hat{f}_k^{(n)} + R_i + S_i}$$

Where N_i is the efficiency correction sinogram. The sum of the forward projected image, random coincidences, and scatter coincidences are the divisor for the coincidence data, seen in the numerator, in the back projection phase. The product of this ratio and the matrix element at the current voxel, is then summed across every projection bin.

The result of the back projection is multiplied by the current voxel estimate and divided by sum of the matrix projection bins for current voxel to yield the new voxel estimate.

Ordered subsets expectation maximization (OSEM), first implemented by Hudson and Larkin[49] uses the same MLEM algorithm, but it applies it to one subset of the data at a time. A subset is a fraction of the projection data, sampling a user-defined number of projection angles. After the forward and backprojection of one subset, known as a sub-iteration, the result is used as

the image estimate for the reconstruction of the next subset. In this context, one iteration is complete once every subset has undergone its own sub-iteration. Images reconstructed with OSEM reach convergence quicker than tradition MLEM, but use of more subsets used has shown to increase the amount of noise.

Maximum A Posteriori (MAP) is a form of maximum likelihood estimation, which applies a penalty function based on *a priori* mean values. In an effort to reduce the image artifact that may occur with an excess number of iterations in MLEM reconstruction, the likelihood function is reconsidered in a Bayesian framework: Incorporating an image prior into the likelihood using Bayes rule creates a new function to iteratively maximize. Levitan and Herman define their image prior using a Gaussian distribution in their seminal approach, but different models of both spatially independent and dependent priors have been proposed since then[50].

1.4 IMAGE QUALITY

1.4.1 Count Rate Performance

One important factor in the assessment of image quality is the noise equivalent count rate (NECR). Although scanners may support an increase in count rate with the detection of more radioactive tracer in the subject, the contribution to the rate from scatter and random coincidences can contaminate the signal from true coincidences. In addition, the scanner might gradually lose more counts to deadtime as the scanner approaches its count rate limits in even more radioactive subjects.

The NECR is defined as:

$$\frac{T^2}{T + S + 2fR}$$

Where T is the true coincidence rate, S is the scattered coincidence rate, R is the random coincidence rate, and the coefficient f is dependent on the method of calculating random coincidences. When it is plotted against activity or activity per unit concentration, it reveals an arc, the peak signifying its optimal performance in true coincidence detection, before further activity introduces more noise and impoverishes the signal[51].

A useful figure in further qualifying the NECR is the percentage deadtime. The measure aptly quantifies the limitations of the system by using the trues rate under low count rate conditions to extrapolate the expected trues rate without deadtime, and comparing it to the actual trues rate[52]. It is defined as:

$$100 * (1 - \frac{T_{actual}}{T_{expected}})$$

1.4.2 Sensitivity and Spatial Resolution

A system's sensitivity is its ability to detect radioactivity. Factors that contribute to a system's sensitivity include sampling (axial, transaxial, and radial), the dimensions of the scanner, and the sensitivity of its individual block detectors, which is dependent on the

scintillator's stopping power. If one ring is considered alone, the overall sensitivity for a single ring is:

$$100 * (\varphi \varepsilon^2 g)$$

Where φ is the packing fraction, g is the geometric efficiency for the detector pair, and ε is the efficiency of the scintillator material[41]. Finding the fractional solid angle (ratio of solid angle to complete coverage, 4π sr) for a source at the center of the ring gives the geometric efficiency:

$$\frac{4\pi - 2(\int_0^{2\pi} \int_0^{\theta} \sin(\theta) d\theta d\phi}{4\pi} = \sin(\tan^{-1}(\frac{h}{2r})) \cong \frac{h}{2r}$$

Where h, the axial height of the ring, is much smaller than r, the radius of the scanner. The average geometric efficiency includes a factor of ½ to compensate for the loss of sensitivity at the axial edges of the ring[51].

The efficiency of the scintillator material is:

$$\Phi * (1 - e^{-\mu d})$$

Where d is the thickness of the detector, μ is the attenuation coefficient of the detector, and Φ is the fraction of accepted events through the energy window[52].

The packing fraction takes into account the reflective material between the detector elements in the scintillator block, which reduces the area of the face of the detector capable of detecting photons. The fraction is calculated by the equation[52]:

$$\frac{width\ x\ height}{(widht + deadspace) + (height + deadspace)}$$

Spatial resolution is the ability to distinguish two points in an image, which in PET imaging is a measure of the device to clearly depict the variation in the distribution of radioactivity.

There are several contributing factors to the spatial resolution: the intrinsic spatial resolution, defined by its point spread function (PSF), limits the resolution of a pair of detectors to half the detector width. The positron range of the tracer places the annihilation site away from where the positron was emitted (The distance from the emission site is proportional to the energy of the positron emitted, which depends on the β+ radioisotope)[53]. The residual momentum of the electron and positron at annihilation introduces error in locating the annihilation site, an effect known as non-collinearity[54].

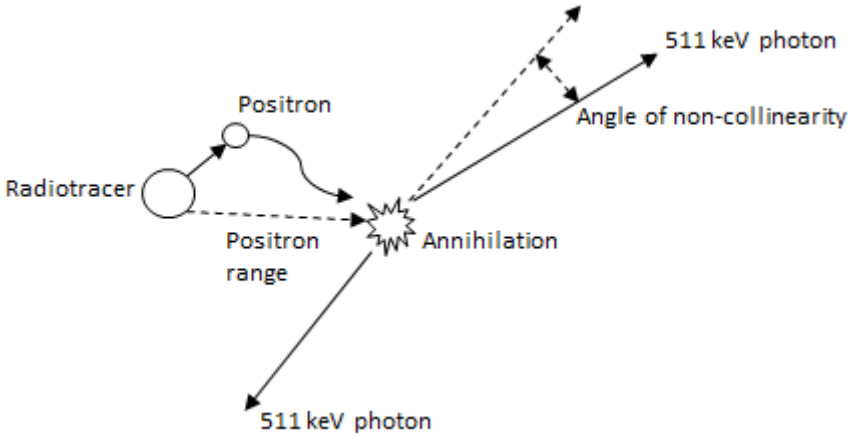

Figure 19: The effect of positron range and non-collinearity on spatial resolution

The ambiguity of where the annihilation photon interacted in the scintillation crystal when the tracer is not in the center of the FOV can result in parallax errors, especially in longer crystals. Recent developments have been made to determine the depth-of-interaction (DOI), to specify where within the scintillation crystal the photon was detected, thus correcting the location of the LOR, and reducing parallax[55].

The convolution of these factors affecting spatial resolution can be represented by the following equation

$$Resolution \cong \sqrt{R^2 + (0.0022D)^2 + \left(\frac{d}{2}\right)^2}$$

Where R is the blurring due to positron range, d/2, or half the detector width, is the intrinsic detector resolution, and 0.0022 times the scanner diameter D is the blurring due to noncollinearity[24].

A poor spatial resolution is detrimental not only to the image quality, but also to the accuracy in reproducing the activity distribution, due to the partial volume effect. This error is the result of trying to resolve structures smaller than the sensitive volume of the scanner, which is approximately equal to twice the full width at half maximum (FWHM) spatial resolution. The effect is a dilution of the activity throughout the sensitive volume, and a mischaracterization of the active structures within that volume[56].

1.4.3 Normalization

Since the sensitivity of a scanner changes throughout the FOV, it is important to account for these variations within the lines of response, and apply normalization factors that make the entire system's response to activity more uniform. The different sources of variation in sensitivity among the LORs are modelled individually in component based normalization, which uses the quantification of each contributor to non-uniformity to generate a series of normalization coefficients. The coefficients are then applied to the projection data during reconstruction to more faithfully reproduce the relative magnitude of activity within different areas of the FOV. An alternate, simpler form of normalization requires only a scan of a uniform source in which every channel is active. The normalization coefficients in this method, known as direct normalization, are the reciprocal of the counts for every LOR, and are applied during reconstruction[57].

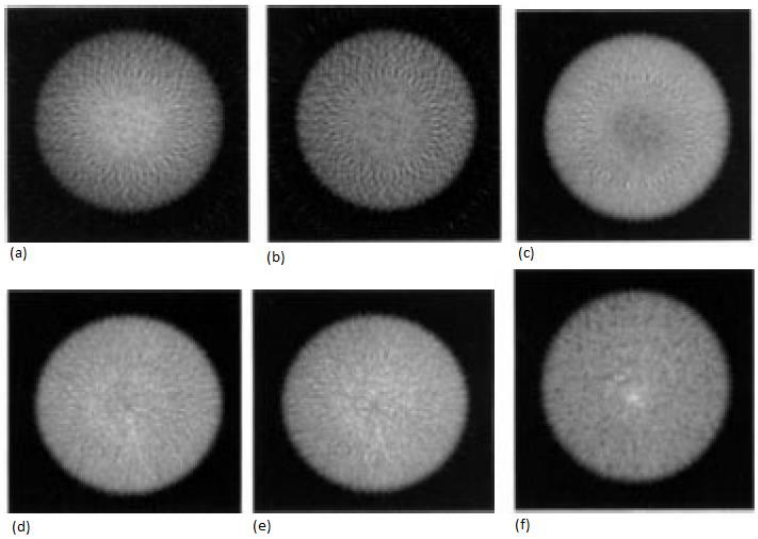

Figure 20: Image artifact and corrections: (a) No correction (b) Scatter correction (c) Detector efficiency and scatter correction (d) Detector efficiency, geometric, and scatter correction (e) Detector efficiency, geometric, crystal interference, and scatter correction (f) Scatter correction and direct normalization from inverted plane source data[58] (©1996 IEEE)

The intrinsic crystal sensitivities regard the differences in performance due to the scintillator or photon counter; The gain setting on an APD or PMT channel may comparatively increase or decrease the signal amplitude for the lines of response associated with that channel. Also, the efficiency of a scintillator element coupled to a given channel, or an entire scintillator block, may deviate from the rest of the system. Time-window misalignment involves an issue of

hardware, which in this case may attenuate the signal from certain crystal pairs because of a failure to properly synchronize the timing across the entire system, and therefore misapplying the time window to determine coincidences[59].

The remainder of the components take issue with the position of the crystal. The crystal interference factors account to sensitivity variations due to the detector element position within a scintillator block. The relative position in the block, when considered with respect to every block in system, makes up the block profile factor. The radial and axial geometric factors consider the variations within and between the planes respectively, as a result of different photon incident angles[59].

1.5 PET APPLICATIONS

The most common uses for the PET modality remain in the biomedical fields. Smaller, preclinical scanners have been commercially developed for research with animal models of human disease and disorders, primarily in oncology and neuroscience. The microPET scanner, which was first developed by Cherry et al in UCLA, has since become a popular commercial product for rodent imaging. It uses LSO scintillators with a multichannel PMT to create a 15 cm or 26 cm diameter FOV, depending on the specific model (Focus 120 or 220), with an axial length of 8 cm. The Inveon small-animal PET scanner, developed by Siemens, is the next generation of the MicroPET system, which extends the axial FOV to 13 cm, and improves overall sensitivity and processing speed[60].

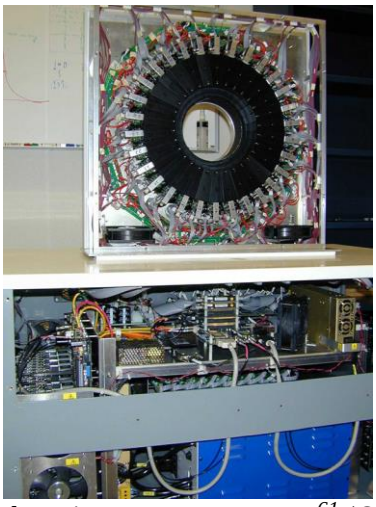

Figure 21: The microPET II scanner[61] (©2002 IEEE)

Recently, multi-modality imaging with positron emission tomography has expanded, from its typical combination with X-Ray Computed Tomography (CT), to an integrated system using magnet resonance imaging (MRI). With the detailed anatomical information provided by MRI, and the high-sensitivity functional information provided by PET, PET-MR has become a valuable tool in brain research and behavioral studies. The difficulty of this approach however, lies in applying magnet-compatible components that do not interfere with MR operation.

Pichler et al. from the University of Tübingen have developed a preclinical PET Insert used in conjunction with a 7-T ClinScan MRI. The PET scanner is APD based, using 12x12 LSO scintillator arrays, with a 1.9 cm transaxial FOV and 4 cm axial length. The scanner has been

used for colon carcinoma studies, using a combination of MR contrast agent and a ^{18}F-FLT radiotracer tracer to track tumor growth and cell necrosis. In another study, the group investigates the potential of functional imaging with both MR and PET, by measuring metabolic activity with blood oxygenation level-dependent (BOLD) fMRI with the PET insert in place. The minimum interference from PET in fMRI suggests that future brain studies using radiolabeled receptor ligands in conjunction with BOLD imaging is possible[62].

The use of smaller scanners have also extended to the plant sciences. The available short-lived positron emitters that can be included in biologically relevant molecules (^{13}N, ^{15}O, ^{11}C, and others) allows the investigator to observe the dynamic transport of photoassimilates down to the roots or transport of materials from the roots upward in the plant. One of the first PET systems designed specifically for plant research was the Positron-emitting tracer imaging system (PETIS), developed by Kume et al. PETIS consists of two opposing 5x6 panel cm^2 detectors, using BGO scintillator crystals coupled to position sensitive photomultiplier tubes (PS-PMT). It has been used for tracking the uptake of ^{13}N-labelled ammonia and ^{15}O-labelled water, and ^{11}C-labelled carbon dioxide[63].

The PlanTIS system, based on the commercial ClearPET developed for biomedical research, uses opposing detector cassettes consisting of four double layered scintillator crystals each (LSO and LuYAP) coupled to multi-channel photomultipliers. The scintillator layers allows for depth of interaction information. The system is vertically oriented to cover a larger portion of the root length, and has been used in conjunction with MRI for ^{11}C-labelled carbon dioxide experiments investigating root growth and transport[64].

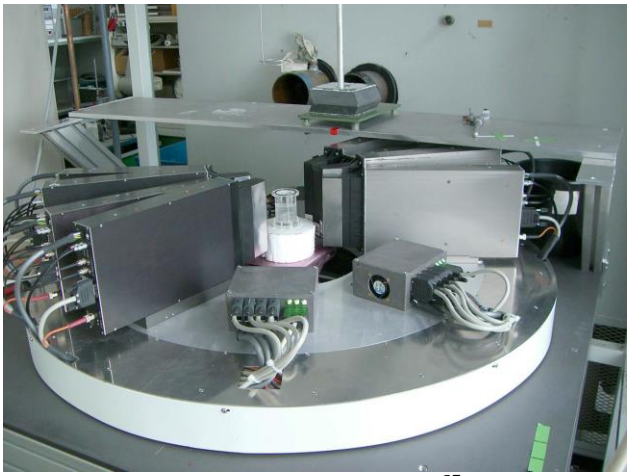

Figure 22: The PlanTIS PET system[65] (©2007 IEEE)

2. Development of Quantitative Data Acquisition and Processing Methods

2.1 NEW HARDWARE AND SOFTWARE ENGINEERING APPROACHES

The Plant Scanner, RatCAP and PET Insert have been updated to the next generation tether-less flex circuit, which no longer uses a tether to transmit signal from the front end to the TSPM ribbon cable connector. A second RatCAP for awake animal imaging, using the new circuit board, has also been developed.

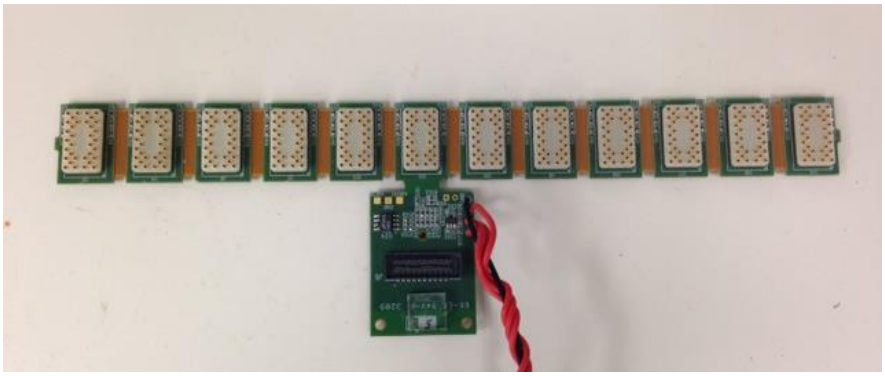

Figure 23: The tether-less RatCAP flex circuit

In addition to adding structural support, the new version also places the digital to analog converter (DAC), responsible for setting the lower level discriminator (LLD), on the flex circuit, rather than the TSPM. The BNL-UPenn System, which uses a series of tower boards that connect to four detector blocks each, uses a DAC for every ASIC, allowing for the application of different energy thresholds for specific detector modules. The Wrist Scanner continues to use the older, tethered version, of the flex circuit, and requires an external analog signal for setting the LLD. To simplify this exception, the external source can be set using scripted commands for a GPIB controller in lieu of scripted TSPM client commands. All systems have been outfitted with additional filtering capacitors for cleaner signals.

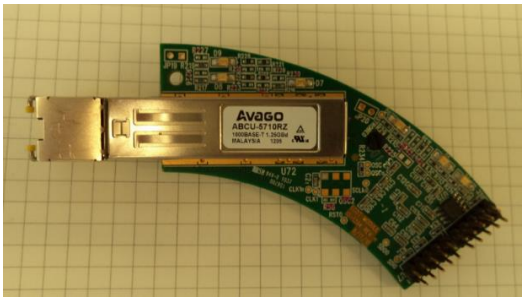

Figure 24: The updated Time Stamp and Signal Processing Module (TSPM), with SFP module attached)

The TSPM has also been updated. The new version, printed on a crescent-shaped circuit board and designed for superior heat dissipation, was specifically developed for the BNL-UPenn System, but can be used with all other scanners when attached to a custom adapter board. One TSPM can handle signals from up to 24 ASICs, therefore necessitating the use of four TSPMs for the full BNL-UPenn System.

The communication between the TSPM and data acquisition (DAQ) computer has changed: the G-Link custom PCI-based (Peripheral Component Interconnect) data acquisition board has been replaced with a commercial gigabit Ethernet card (Rosewill PCI Express Gigabit Ethernet Card RC-401-EX). One DAQ computer can now access any number of TSPMs at once, requiring only that additional Ethernet cards are installed. The TSPM transmits and receives data through a small form-factor pluggable (SFP) transceiver, which can use either fiber-optical cable or copper Ethernet. Fiber optic Ethernet becomes a necessity when using the system in conjunction with MRI, since copper RJ45 cables are susceptible to electromagnetic interference from the radiofrequency coil.

The older software, which was written in LabVIEW and Matlab, and ran on the Windows operating system, has been replaced and updated with Linux-based C++ / ROOT programs and BASH scripting routines (ROOT is a data analysis framework developed at European Organization for Nuclear Research, CERN[66]. BASH is the Bourne-Again Shell). The newer software has been designed to work on any scanner, and can easily be updated to support additional new scanners.

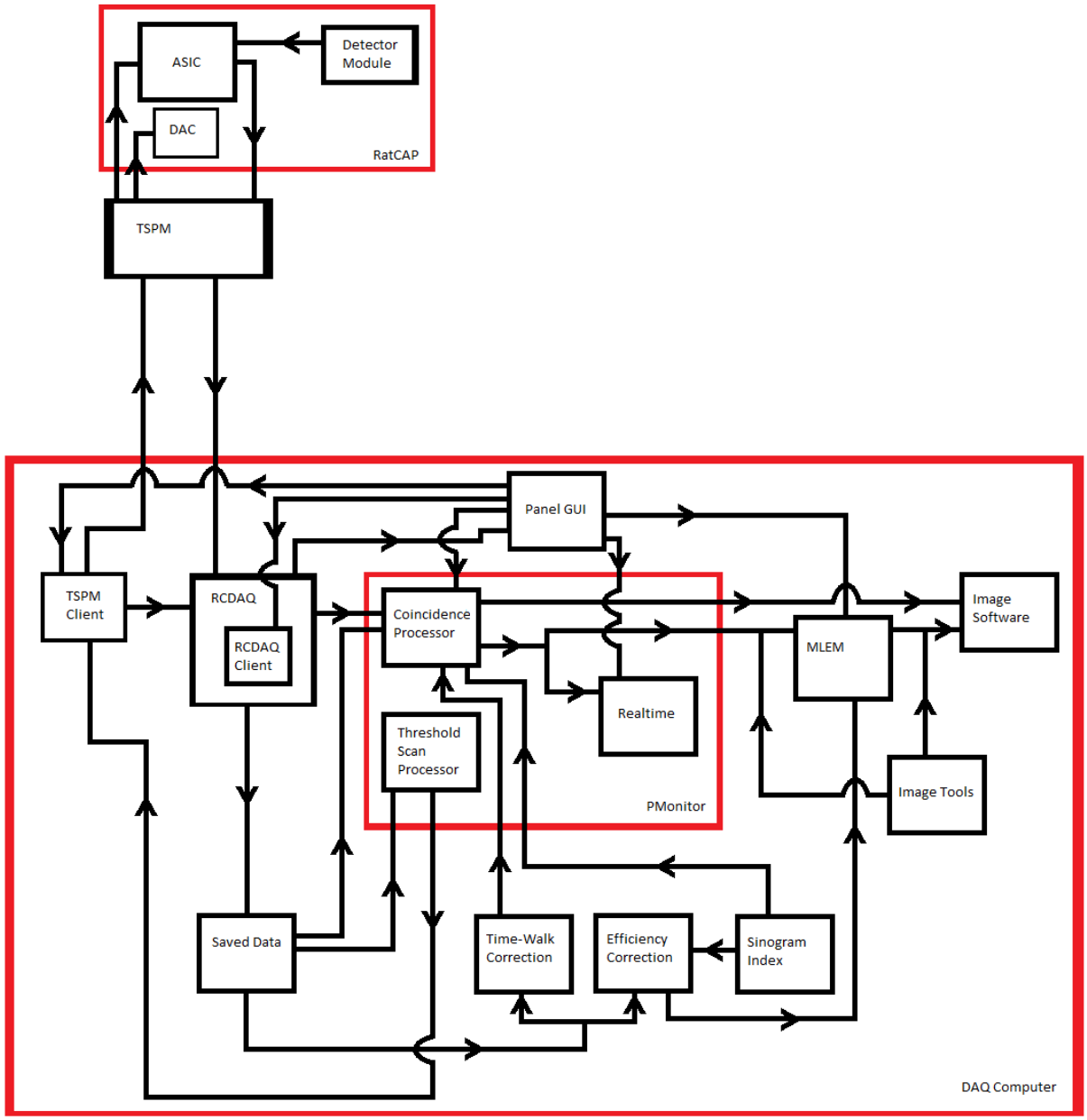

Figure 25: Flowchart of data acquisition and processing

The collection of new software, named the MI_RCDAQ suite, is used in conjunction with the PHENIX RCDAQ and PMonitor frameworks (developed by Martin Purschke[67,68]), and the TSPM client. The suite is packaged for easy installation on new computers and comes complete with the necessary tools for calibration, data acquisition and processing. Its programs, diagramed in figure 25, are organized using standard project structure, and are version controlled with native Linux tracking software. The data processing components of the suite have been

developed for use on multiple servers, so that the workload of image reconstruction can be distributed for parallel processing. It has been installed on several distributions of Linux (Gentoo, Redhat, Ubuntu, Scientific Linux), and requires no outside software for its operation. Specific files, such as APD gain calibration factors, system matrices, custom setup scripts, and lookup tables, are organized in the package directories by scanner type, and are updated consistently for quality control.

2.2 MORE ROBUST DATA THROUGHPUT

2.2.1 Data Transmission

Rather than dividing the singles' timestamps into coarse and fine components, the new TSPM uses a phase lock loop (PLL) to generate a 500 MHz clock, improving the timestamp resolution from 10 ns to 2 ns. When using the PET Insert in conjunction with MR, the TSPM data clock deviates slightly from 2 ns to avoid harmonic interference with the RF coil. To ensure the proper function of scanner calibration and communication, the PLL generates other clock frequencies corresponding to different aspects of the system: The Gigabit Ethernet block of the FPGA uses a 125 MHz clock for data transmission, while the TSPM IO functions, including data arbitration, register access, and signal processing, runs on a 100 MHz clock. The SPI for the front end, responsible for gain calibration during system power-up, is limited by the ASICs capabilities, and runs on a 100 KHz clock.

Communication between the TSPM and DAQ computer now uses the Internet protocol (IP) suite. Once the DAQ computer's address resolution protocol (ARP) table maps the TSPM (or TSPMs in the case of the BNL-UPenn Scanner) hardware address to the network layer IP address, communication between the scanner and computer is established, and ready for system calibration or data transmission.

The singles data transmitted from the TSPM is divided into UDP (User Datagram Protocol) packets. Each packet contains a maximum of 126 singles events in list-mode. Each single event is saved as a 64 bit word, with 2 bits set for gating, 5 bits for block address, 5 bits for channel address, 10 sequence bits set for checking for any lapses in data transmission, and 46 bits set for the timestamp (an improvement from 36 bits). The two bits set for gating are set high or low dependent on an external gating line, connected to the MR control software.

Packets also reserve space for a header, which contains a 32 bit serial number, a 28 bit singles rate, and 64 bits for user-defined information. The header singles rate is provided directly by the ASIC readout, and can be measured against the timestamp based count rate when analyzing the data. With the user defined header space, records of anomalies or unexpected occurrences can be directly integrated into the data during the scan. Altogether, the UDP packet size is approximately 1 kB.

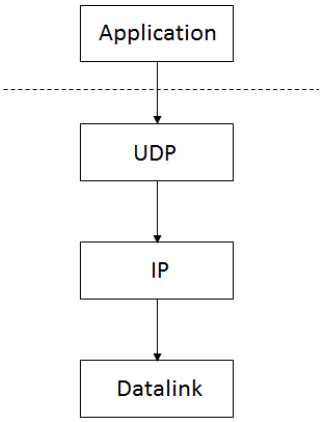

Figure 26: (Bottom to top) Model showing the data-link layer (TSPM), network layer, transport layer, and process layer (TSPM client) for UDP communication. Data acquisition using the RCDAQ follows same chain in reverse

The UDP service is connectionless, in that each packet is independent of one another, and no confirmation is made that the packet was received. In contrast, the more secure Transmission Control Protocol (TCP), transmits data as a byte stream, rather than datagrams, and assures the complete success of the transmission. However, the TCP safeguards come at the sacrifice of speed and versatility; UDP does not require handshakes and additional packets to establish a connection, and will never delay incoming data to verify whether the data is complete and in order. The UDP transport layer is thus more compatible with the nature of PET imaging, where the pace of recording data is more essential.

The data loss associated with the UDP service can occur between transmitted packets: when one packet is transmitted, there is a small lag before the next packet can be filled with singles events. This time lapse is the transmission based deadtime, and it is reported as a percentage of time lost compared to the whole. It is calculated by finding the difference between the time within every packet and the overall scan time. When the data rates are high, the probability that a packet will not be transmitted, or "lost" (a disadvantage of UDP), increases, thus adding to the deadtime. The packet header serial number keeps track of the packets sent from the TSPM to the DAQ computer, in order to assess whether any packets were dropped. To ensure that no data is lost within a packet, the sequence bits of each 64 bit word are used to trace each singles event.

2.2.2 Signal Processing

The user controls the TSPM using the TSPM client, a scriptable command line interface which sends UDP packets containing values for writing to specific registers in the TSPM Altera Stratix II FPGA. The instructions written to the registers specify to the FPGA firmware the configuration parameters of the PET system, including scanner-specific modes of operation and thresholds settings for photon energy discrimination (Writing to the threshold setting register prompts the FPGA to program the DAC that sets the LLD.) In addition, new TSPM commands have been introduced for more control during data acquisition: One register provides a timeout which prevents unexpected errors in UDP transmission or signal delays from blocking the datastream. This is done by setting the length of time the TSPM should wait for another single event before it transmits an unfilled data packet. Another register potentially removes motion artifact or interference by controlling a switch that determines whether data collected during the gating period, marked by the 2 first bits of each word, is flagged or deleted (known as the "veto" bit). Block detector modules that appear to be malfunctioning can be disabled altogether through the ASIC disable register.

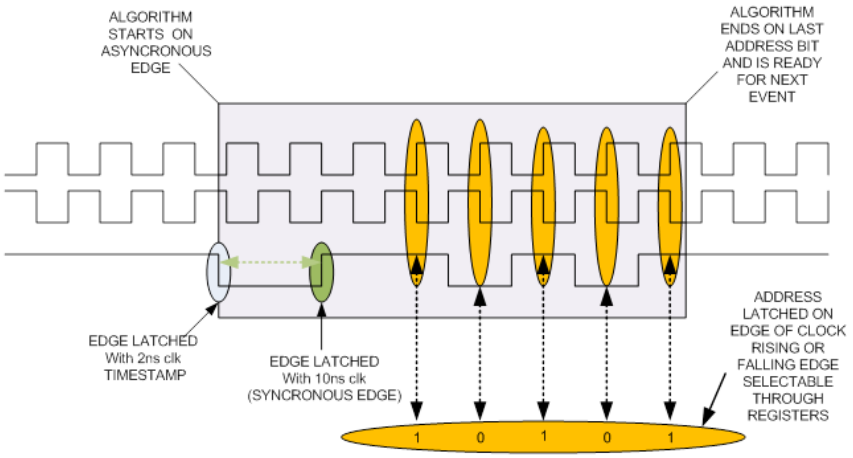

Figure 27: ASIC readout

The phase correction scheme has been improved with the new TSPM: When the detector module receives a signal, a stop bit, followed by the 5 bit address of the receiving channel, is encoded by the ASIC using a 100 MHz clock, and transmitted to the FPGA one full clock cycle after the asynchronous timing edge. The FPGA uses the asynchronous timing edge to determine

the time at which the singles event occurred, and decodes the subsequent channel address, beginning after the next synchronous edge, to determine the position where it occurred. At times however, the FPGA, after the algorithm latches to the asynchronous timing edge and detects the synchronous edge, may begin to read the following address on the wrong 10 ns clock edge. This is known as a "phase" error, and can result in the incorrect positioning of singles data. Using a TSPM client command, the user can switch between the rising or falling edge of the clock when reading the address to ensure that it is read correctly. In the rare occasion that the read sequence begins on the wrong clock cycle, another TSPM register can be accessed through the client to read the channel sequence one cycle later.

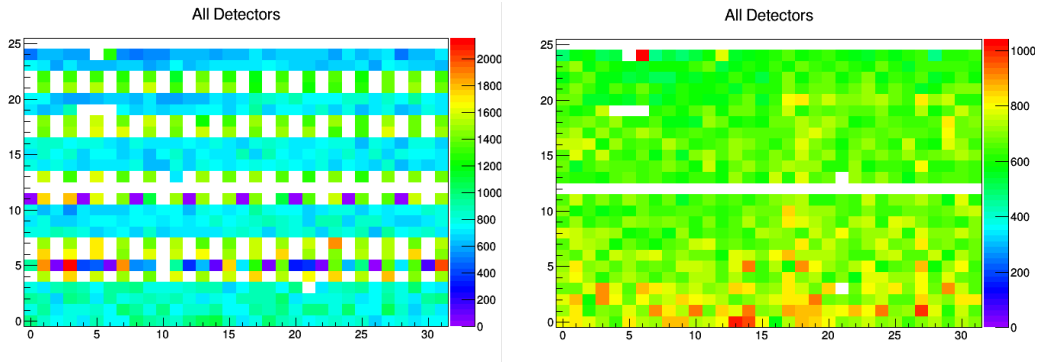

Figure 28: Channel hitmaps of channels 0-31 for blocks 0-25. (Left) Phase is programmed incorrectly, therefore losing the lowest significant bit of channel address. (Right) Phase is programmed correctly

Potential "phase" errors are diagnosed by inspecting the realtime channel hitmap: If the phase is incorrect, it could either affect least significant bit, causing alternating channels to seem nonresponsive, or the most significant bit, causing the upper half or lower half of the channels to be misread. To prevent this crosstalk, phase corrections are found for each ASIC for every new version of firmware, and applied at startup. The user now selects from four phase settings, as opposed to 33 settings which were less reliable in avoiding crosstalk.

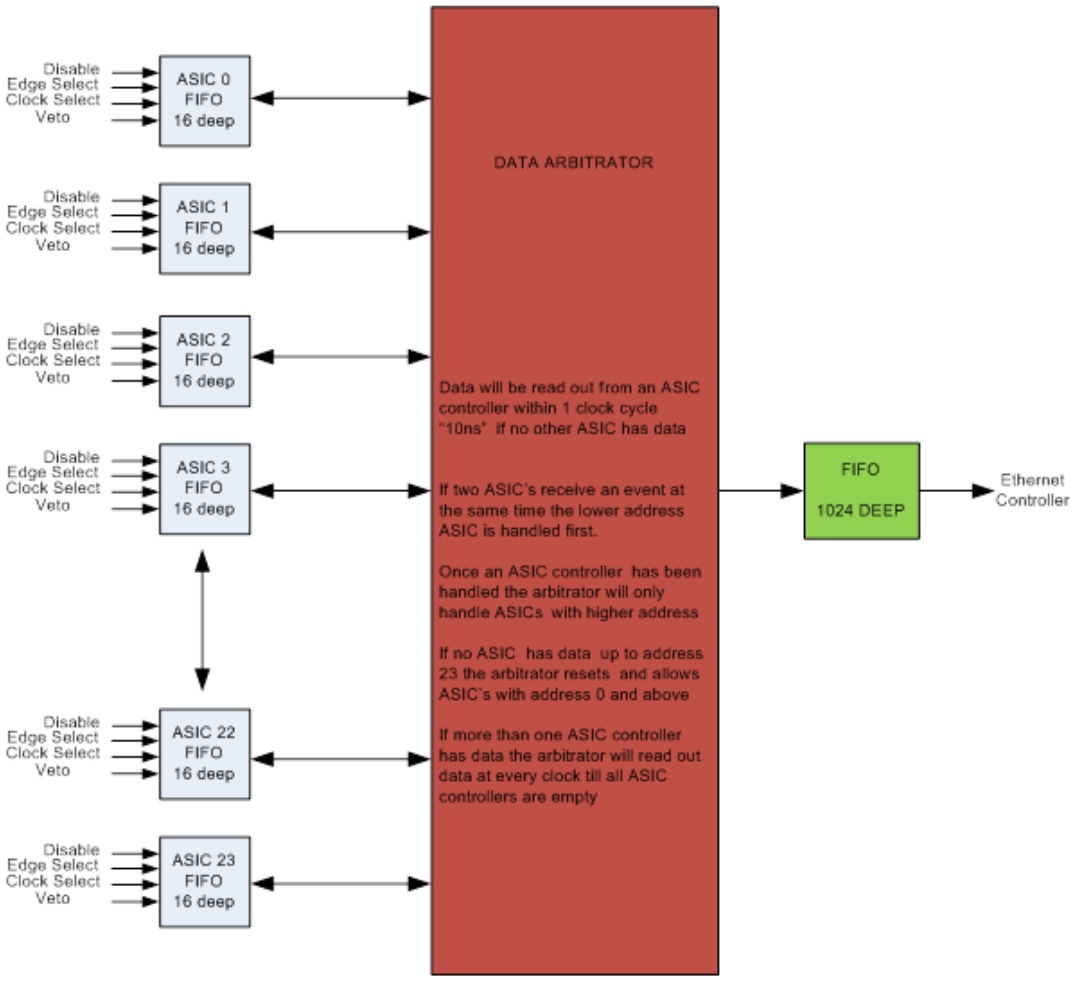

Figure 29: Data arbitration scheme for the TSPM

Figure 29 shows a diagram of the data arbitration scheme within the FPGA. Each ASIC controller within the FPGA firmware, controls the disable, edge select, clock select, and veto switches described earlier for its assigned ASIC, and contains a 16 byte (64 bit) first-in-first-out (FIFO) buffer which receives the single event from the detector module. The arbitrator will read in and empty the contents of each buffer 0-23, one ASIC controller per clock cycle (10 ns), starting with the receiving controller with the smallest address. The data from each buffer fills the 1024 byte FIFO buffer, which is sent out through the Ethernet controller as a UDP packet, read by the DAQ computer.

2.3 COMPREHENSIVE ONLINE MONITORING

2.3.1 Data Acquisition

The RatCAP and its associated scanners now use the flexible Remote Call Data Acquisition (RCDAQ) software for recording data[67]. Running the RCDAQ software creates a server, in which plugins can be loaded to interact with a variety of different data generating devices. Its versatility is owed to its origins in the Pioneering High Energy Nuclear Interaction Experiment (PHENIX)[68], where a compact data acquisition system was necessary for testing its many types of data and detectors. Commands to the server are issued through the RCDAQ client using the Remote Procedure Call (RPC) network protocol, allowing the user to control the acquisition system from anywhere through a virtual connection. Most recently, a website has been created that can control the RCDAQ.

When using the RatCAP and related technologies, the plugin containing the library needed for communication with the TSPM is loaded. This allows the RCDAQ server to receive data from two different aspects related to the TSPM's operation: the data it collects and transmits from the front-end, and a read-back of the calibration parameters applied during the system's configuration. These aspects are reflected in the "create device" RCDAQ client command: One device is created for receiving packets of singles data from the PET scanner, and another collects data concerning the gain, LLD, scanner type, and other configuration settings that are essential to understanding each dataset.

The way these different kinds of information are saved is defined by the PHENIX raw data format (PRDF) [69]. Using PRDF, RCDAQ distinguishes different kinds of information, such as UDP packets or text files containing calibration parameters, by enveloping them in an "event" structure. An event is then assigned a type based on the information it holds, which is written in its header. In addition, each event within a data set is numbered (which can be compared with a UDP packet's serial number) and contains the date and time in which it was created.

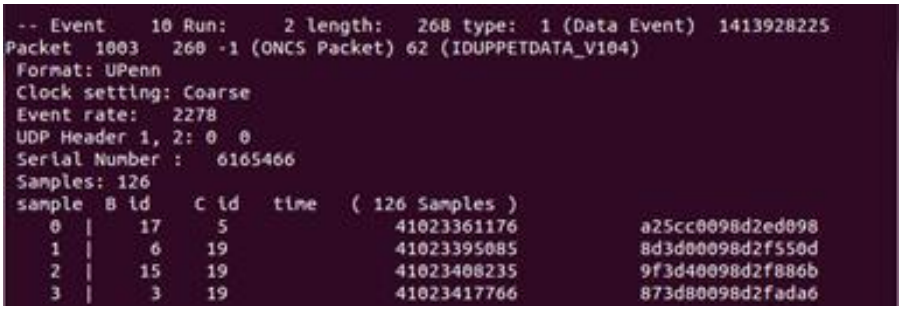

Figure 30: Output of pdump utility on command line

Data that is packaged in the PRDF event structure during acquisition is accessible to any processing software which includes the Event Handling Library. This can include realtime monitoring software for instant feedback from event data. Figure 30 shows the output of one of the basic tools in the event handling suite: the packet dump (pdump) utility[67]. Accessed from the command line, it can simply display the contents of an event, including its event header, its packet header, and, in the case of RatCAP type scanners, the singles data. In this figure, 4 of the 126 singles are shown, each displaying the raw 64 bit word, along with the decoded block and channel addresses and timestamps.

To begin data acquisition, the RCDAQ server binds the address of the TSPM connected Ethernet port to a file descriptor, from which a memory buffer, known as the fill buffer, receives the data. Though the packets are pooled together within the buffer, the acquisition readlist, which lists the parameters corresponding to each loaded device (in this case, the TSPM device), specifies the packet length, allowing the filled buffer to be divided into separate event structures. Packets, in this sense, can be regarded as sub-events, containing the raw data that are encapsulated in the data event structure. Once the buffer is full, the data is moved to a transfer buffer, while the original fill buffer continues to receive data. The data in the transfer buffer can then be sent to a monitoring socket, where it can be accessed by other compatible programs. If indicated by the user, the transfer buffer data can also be written to disk as a PRDF file. A series of mutually exclusive (mutex) locks make sure that the process of switching buffers and the recurrent processes of writing to a file or monitoring socket never interfere with one another. In the case that the buffer fills very slowly and holds up the monitor, an adaptive buffering function provides a time-out function, which automatically triggers the filling buffer to move its content into the transfer buffer after a given time has passed.

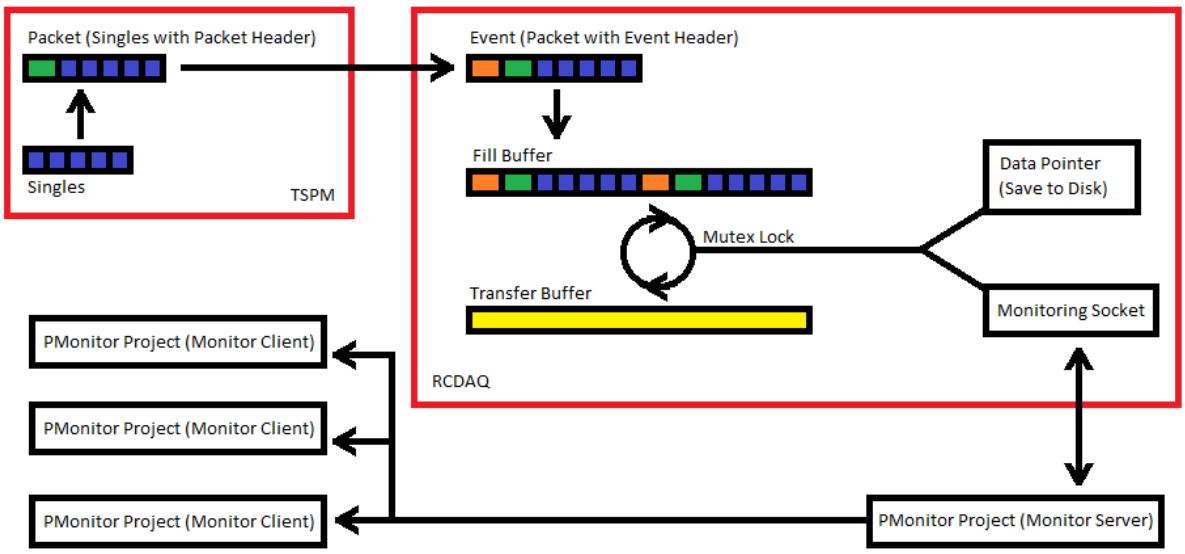

Figure 31: Diagram of TSPM (hardware) to RCDAQ (acquisition software) to PMonitor (data processing and monitoring software) communication

Once creating the appropriate devices, RCDAQ server is setup so that the first event of a dataset is a unique type of event, which contains textual information about the system's calibration. A copy of the shell scripts that contain the RCDAQ client and TSPM client startup commands can also be saved in this begin run event, through the creation of another DAQ device. In past scans, we have saved data from different sources, such as photographs of the PET scanner subject from a still camera, within the datastream by matching those sources with appropriate DAQ devices, and designating them with specific event types[70].

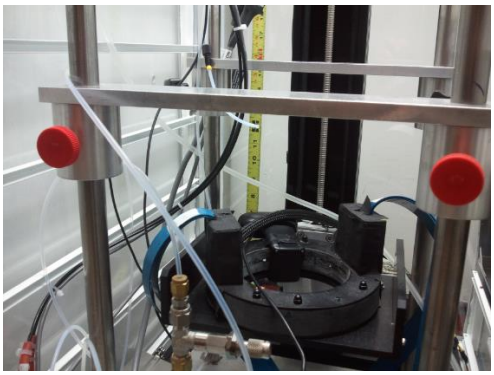

Figure 32: Plant Scanner using attached camera to photograph tape measure in plant growth chamber. Photographs are enveloped within event structure and inserted into the datastream

With the setup complete, the scanner is ready to acquire data. To supply the user with appropriate feedback of the scan, both offline and online, several tools, known as projects, have been developed using the PHENIX Monitor (Pmonitor) framework[68], which will be discussed in the following section.

2.3.2 User Interface

Software that incorporate the PMonitor library use the PRDF event structure to open and analyze data. Being multi-threaded, it can open a data stream that allows for user input and monitoring concurrent with data processing. The data stream can come from a data file already taken, or from data that is currently being acquired. This is possible because of the event structure that defines PRDF: The PMonitor projects use event iterators that latch onto the datastream and parses the data one packet at a time, regardless of whether the series of events is saved to the disk, or accessed buffer by buffer from the RCDAQ monitoring socket. PRDF also provides easy access to packet information, giving access not only to singles information, but also packet and event headers, such as event rates and packet serial numbers. This information can be accessed by multiple Pmonitor projects at the same time, as long as one project, running as a monitor server, opens the data stream first. Afterwards, any following project can connect to the monitor server by running as monitor client; a feature that becomes essential when simultaneous data processing and monitoring is needed.

To display coincidence data in realtime, the coincidence processor, run as a monitor server, opens the live datastream and processes its content, which is accessed by the realtime monitoring program, run as a monitor client. The main page of the monitor program displays the hitmap of the detector's channels, along with prompt, delayed, and true coincidences, as an updating counter and on a timeline. For basic positioning and source distribution feedback, an updated rotating view of the PET detector's projections is shown. A separate panel graphical user interface (GUI) handles the monitor server / client operations, and also allows for easy control of the scanner setup, and online and offline processing, without the user issuing console commands and scripts.

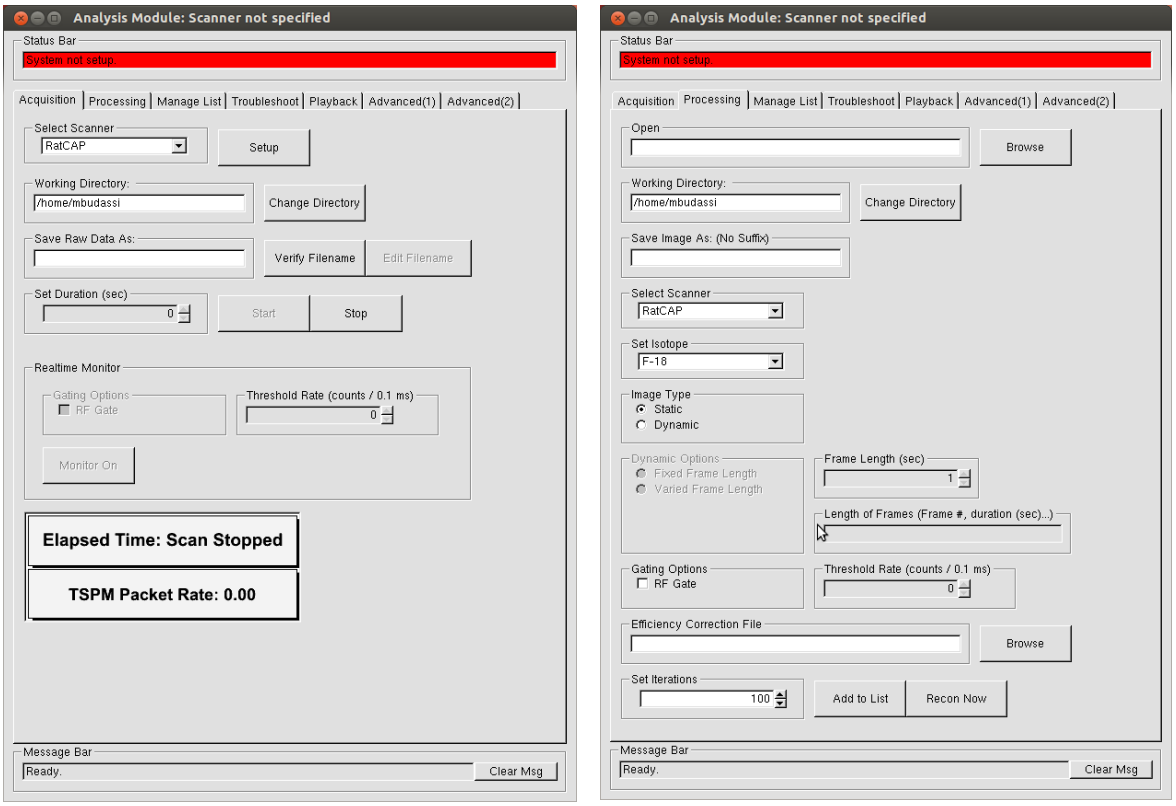

Figure 33: Acquisition (left) and processing (right) tabs of panel GUI

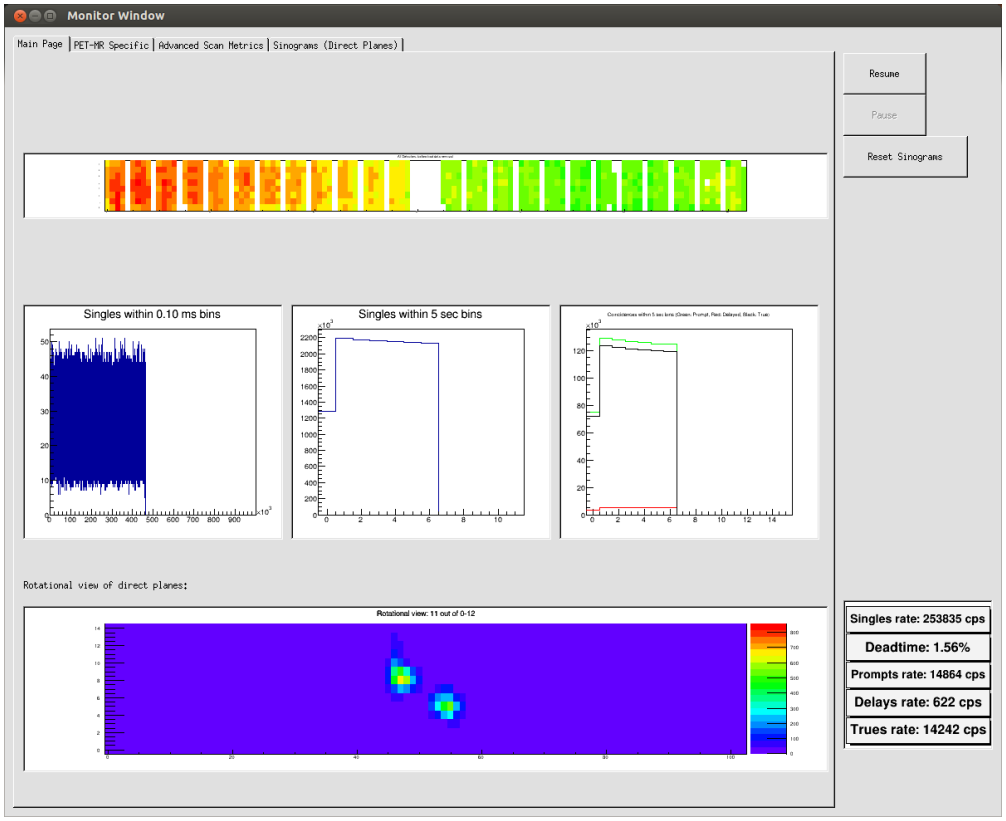

Figure 34: Front page of monitoring program

Realtime projection view and realtime updates of the prompt, delayed, and true sinograms of the direct detector planes use a sinogram bin lookup table to match each coincidental channel pair with a 3D sinogram bin. Because the number of channels in our scanners is relatively small, coincidences between detectors can instantly be assigned a LOR, and displayed on the monitoring program as soon as they are detected. The software that creates the sinogram lookup table only requires the number of rings, the number of detectors per ring, and the numbering scheme of the scanner's detectors (Because we are not concerned with saving disk space, the sinogram mashing factor and span have been set to one). In the case that the user is interested in imaging a specific axial section within the subject, new lookup tables that correspond to a defined portion of the scanner can be written by creating a new scanner class. A switch in the coincidence processor is then enabled to create sinograms, online or offline, according to the custom table. Figure 35 shows a reconstructed dataset of a resolution phantom using the central four rings of the BNL-UPenn System, which normally uses all 16 rings.

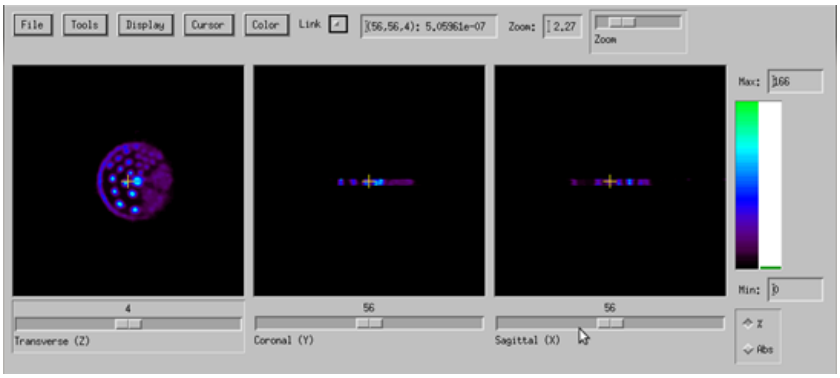

Figure 35: Transaxial, coronal, and sagittal sections of a resolution phantom. Data was acquired only from the axial center of the BNL-UPenn System

2.4 QUANTITIATIVE DATA PROCESSING

2.4.1 Coincidence Processing

The coincidence processor, when used in offline mode, will write out prompt and delayed sinograms into a binary file, which is read by our maximum likelihood expectation maximization (MLEM) reconstruction software. Using the event headers of the PRDF file, it can create sinograms for time intervals within the dataset, which can later be reconstructed into dynamic images. The sinograms have corresponding log files that contain information about the scan, including scanner type, data integrity, single and coincidence totals and rates, gating deadtime, transmission based deadtime, scan date and time, and the number and length of time frames. For the sinograms and the images that the sinograms will be reconstructed into, header files, compatible with ASIPro[71] and PMOD[72], are written, which describe the geometry of the scanner. The user can indicate the radioisotope used in the scan to include decay correction factors for each frame in the dynamic image header. To ensure that the data rates in each frame are comparable with regards to the duration of each frame, a correction factor for the deadtime is included in the header as well.

The coincidence processor works by reading in the Event structured data, and collecting the singles data in data pool, known as the set. The Event iterator passes through each event, extracting each single, and reassigning the block and channel ID, which originates from the APD pin number, to correspond to the scanner channel layout, as described in the sinogram lookup table.

The coincidence processor, along with the other software, uses class-based definitions to provide processing instructions for each scanner's unique specifications. For example, the BNL-UPenn System specific functions identify different types of data packets to issue the singles list-mode data with channel IDs that correspond to the entire system; the Plant Scanner specific functions consider the virtual blocks between the flex circuits when writing sinograms. Class-based definitions include the specific sinogram lookup table, the time correction lookup table (will be discussed in section 3.1.2), channel number assignment, and geometry for each scanner.

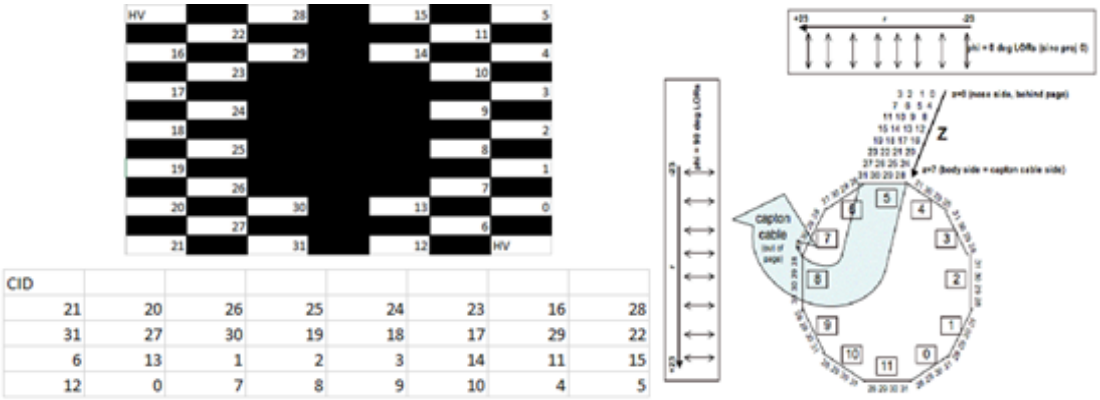

Figure 36: (Top left) Diagram of numeration scheme as written by TSPM. (Bottom Left) RatCAP map of APD pin to discrete crystals and (Right) numeration scheme as represented by the sinogram lookup table

Addresses and timestamps that have been reported incorrectly are removed by checking for nonexistent channels and aberrations in the detection time (if the difference in subsequent singles exceeds a given threshold, the single is removed). If the file containing timing correction factors is read into the program, the time stamp is corrected before being inserted into the set, where it is sorted based on its timestamp. Since all information pertaining to the event or packet from which the single originates is lost once the single enters the set, the length of time contained with a packet is recorded. This time span is regarded as the live time, which is compared against the total elapsed time to determine the time lost due to transmission. During normal operation, this transmission based deadtime amounts to ~1.5% of the scan time, but it can increase with the loss of UDP packets at high data rates.

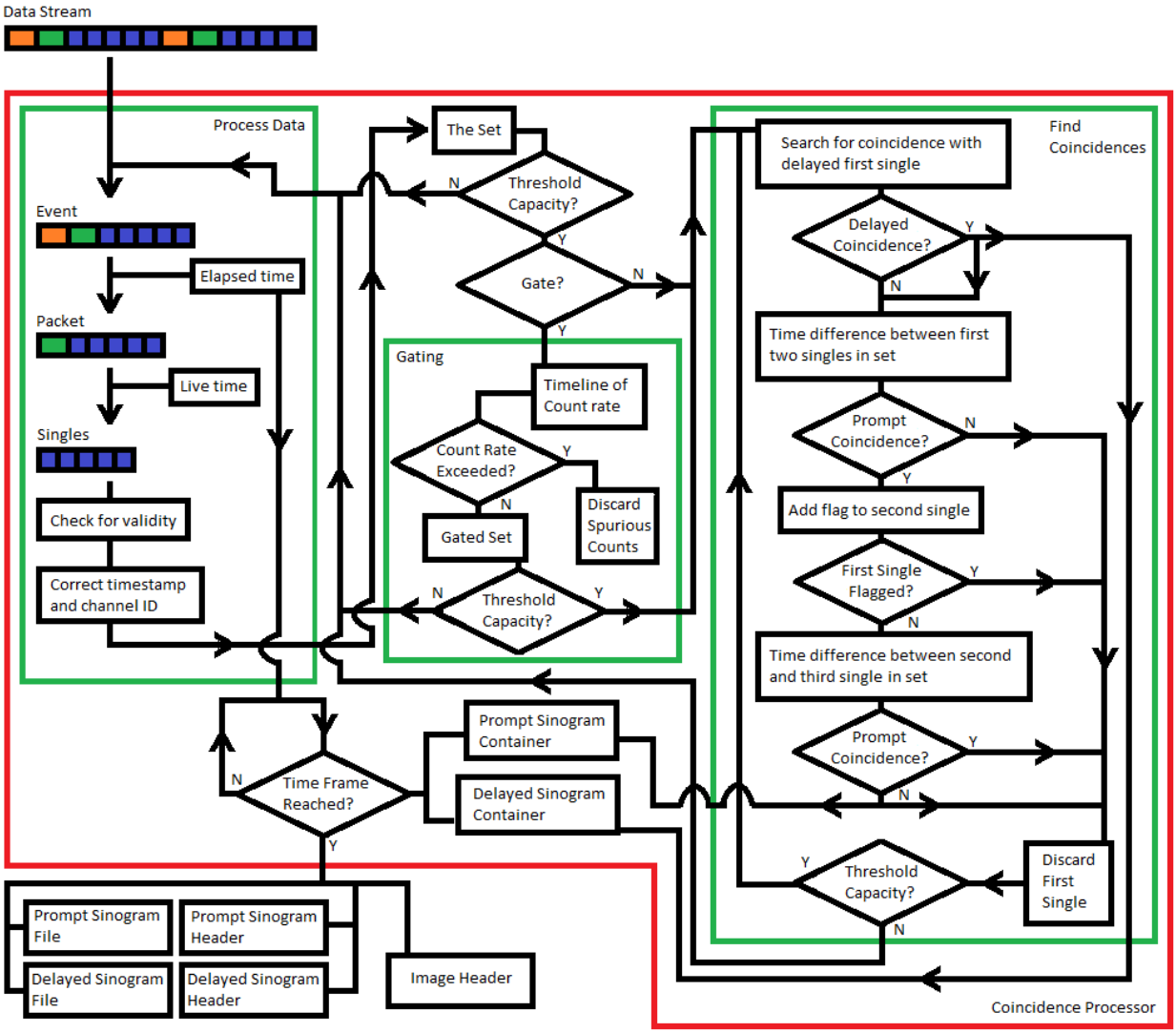

Figure 37: Flowchart of coincidence processor

When an external transistor-transistor logic (TTL) signal is not used for gating, the removal of false counts due to RF interference can be removed in realtime or offline by singles-based gating. In simultaneous PET-MR imaging, interference from the MRI can often trigger spikes of spurious data for the duration of the RF duty cycle, resulting in false coincidences. When the user activates singles-based gating before running the coincidence processor, the set is run through the gating function before searching for coincidences. The singles are plotted into time bins lasting a fraction of the RF duty cycle. If the number of counts in a single time bin exceeds a user-defined threshold, then the counts from that bin, along with the counts from the bins immediately preceding and following it are removed from the set. The time lost due to

interference throughout the scan is also calculated and reported as a separate source of deadtime. In the monitoring program, a timeline displaying the counts per time bin is plotted before and after the interference removal, along with a channel hitmap indicating which channels are affected by the MR. The channels most susceptible to interference are often at the periphery of the block detector. Depending on the effectiveness of the shielding and the intensity of the RF, the deadtime due to gating for a typical simultaneous PET-MR scan with the PET Insert, using FLASH MRI sequences throughout the scan, ranges between 4.1% and 5.6%.

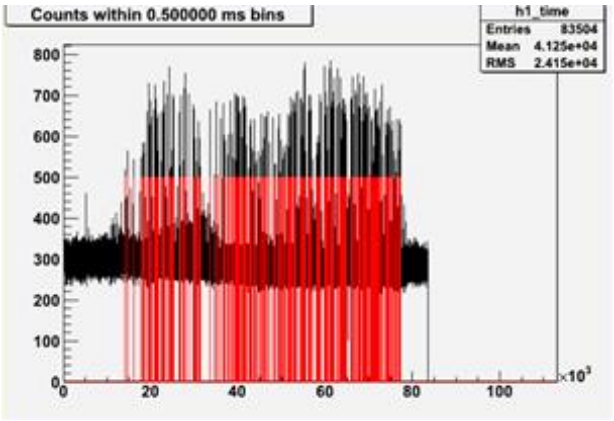

Figure 38: Timeline of counts during a simultaneous PET/MR scan. Spurious counts (highlighted in red) are ultimately removed by the processing software

Once the set reaches a given size, it is passed into the coincidence detection function. The check for the set size assures that singles that comprise true coincidences can find their matching single within the set. The correct approximation of accidental coincidences being essential to the performance of our PET scanners, our coincidence processing chain begins with the detection of random coincidences. For our scanners, we employ the delayed coincidence method: In lieu of an electronic delay circuit, our coincidence processor checks for random coincidences within the set, one single at a time[11]. The function reads in the first single within the set, and adds a delay time (~100 ns) to its timestamp, and looks for another single event in coincidence with it. If the single with the added delay and another single further along in time in the set fall within the time window, the coincidence is added to the randoms sinogram. Figure 39 shows the time difference between prompt coincidences (left) and delayed coincidences (right). Highlighted in red in the prompt coincidences is the plateau comprised of delay coincidences; the number of counts within the plateau is approximately the number of detected delayed coincidences.

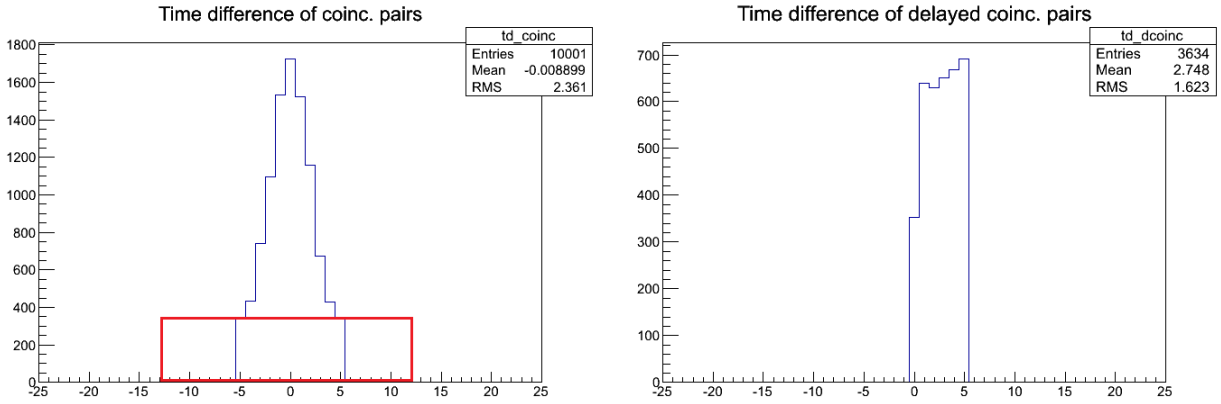

Figure 39: Histogram of time differences in clock cycles, one tick equal to 2 ns. (Left) Prompt coincidences and (Right) delayed coincidences

After checking if the same single event, without the added delay, comprises a prompt or multiple coincidence, it is removed from the set, and the next single is processed, until the coincidence processing loop has gone through every single in the set. At the end of the processing chain, when the prompts and randoms sinograms are written, the randoms sinogram is added to the sum of the system matrix voxels per LOR in the forward projection phase of the MLEM algorithm. For purely demonstrative purposes, when Poisson statistics in the sinogram do not need to be preserved, the difference of the prompts and delays sinogram can be taken to approximate a sinogram of the trues coincidences, as seen in figure 40.

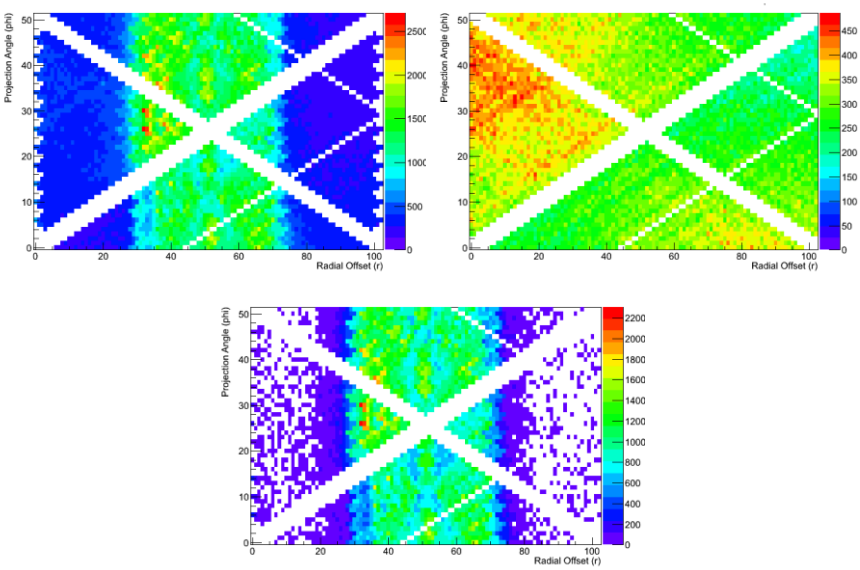

Figure 40: (Top Left) Prompt coincidence sinogram, (Top Right) delayed coincidence sinogram, and (bottom) the difference between them, yielding the true coincidence sinogram. White streaks in center are the result of the lack of data from the virtual blocks. Other white streaks are from nonresponsive channels

Prompt coincidences are determined by finding the time difference between a single event, and the following single event in the set. If the time difference is bigger than the time window, the single is discarded, and the next single passes through the coincidence function, beginning with delayed coincidence detection. If the time difference is smaller or equal to the time window, the difference between the second single in question and the third subsequent single is compared to the time window. If these two are in coincidence, then the first single is discarded, and the second and third singles are flagged. Flagged singles also pass through the coincidence loop in order to determine whether other singles in the set fall within the same multiple coincidence, and are ultimately discarded.

If the first and second single are in coincidence, but the second and third are not, the coincidence is added to the prompts sinogram. Prompts and randoms sinograms are written by using a combination of the channel addresses of the two singles, called a global channel pair index. The sinogram lookup table maps the pair address to a sinogram bin, which is included to the sinogram at the end of the processing chain. If prompted by the user, if the scan time, indicated by the event header, shows that a given amount of time has elapsed, the path from filling the set with new singles to finding coincidences within the set can be interrupted to write sinograms for that time interval. These individual sinograms of specified time intervals are reconstructed and concatenated to form dynamic images. Time intervals can be of a fixed length (e.g. five minute intervals of an entire scan), or can vary (e.g. first interval is five minutes, next three are ten…) depending on the user input. When the radioisotope is indicated, the image headers for the reconstructed sinograms will contain scale factors (compatible with ASIPro) that account for radioactive decay within and across the time frames.

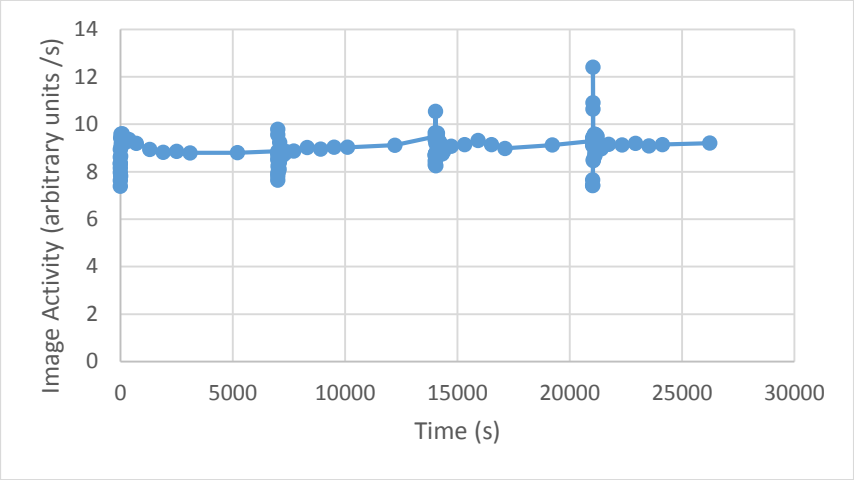

Figure 41: Time activity curve of uniform phantom, using different time frame lengths

Figure 41 is a time activity curve from uniform phantom data taken with the RatCAP, using different frame sizes. Following a pattern of ten one-second frames, ten ten-second frames, five one-minute frames, five ten-minute frames, and one one-hour frame, the curve is corrected for decay and expressed as a rate, using live time. The greatest source of variation of the data is seen in the shorter frames, which when included, brings the mean down to 8.95 s^{-1}, and standard deviation of 0.67. When the one-second and ten-second frames are removed, the standard deviation drops to 0.22, with a more realistic mean of 9.08 s^{-1}.

Initially, the software discussed using the PMonitor framework were loaded as library files, and controlled with ROOT scripts. Because it often desirable to queue jobs that use this software in batches, an additional tab in the panel GUI for managing jobs has been created. In addition to allowing the user to set parameters for reconstruction quickly and easily, it also automates the implementation of the workload management system Condor for parallel data processing across a collection of cluster nodes, resulting in quicker image reconstruction throughput.

2.4.2 Image Processing

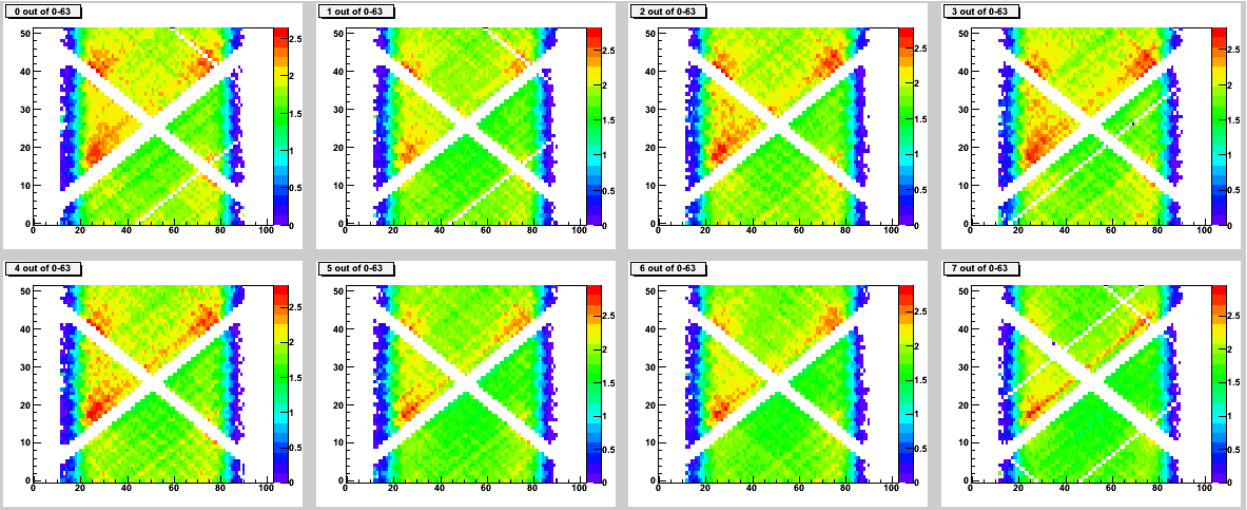

Figure 42: Efficiency correction sinograms for the direct planes of the Plant Scanner

The software that creates sinogram lookup tables can also be used to create custom efficiency correction sinograms, which can set the efficiency of any sinogram bin to zero, if a channel is unresponsive or malfunctioning in a given scan. The custom efficiency correction can either set the efficiency of the sinogram bins corresponding to properly functioning channels to one, or use the efficiency values previously calculated using normalization data. Figure 43 on the left shows an example of a reconstructed uniform phantom that does not account for a dead channel, and the ray-like artifact that can result. The figure on the right corrects the efficiency correction sinogram by incorporating the malfunctioning channel.

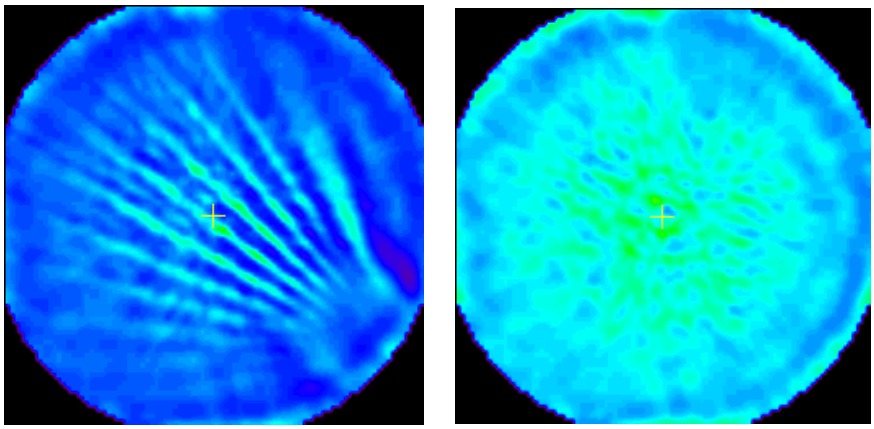

Figure 43: Images from uniform phantom. (Left) Using normalization data that does not account for a malfunctioning channel (Right) Corrected normalization data

When normalization data is available, the efficiency correction software can use it to correct for detector inefficiencies unaccounted for in the system matrix simulation. This program takes a dataset in which the FOV is filled evenly with activity, and finds the ratio of the true counts in each sinogram to the number of counts in a simulated phantom. The sum of the given scanner system matrix voxels per LOR (abbreviated as sum sinograms) supplies the comparative estimation. Figure 44 shows the sum sinograms for the direct planes of a simulated uniform phantom.

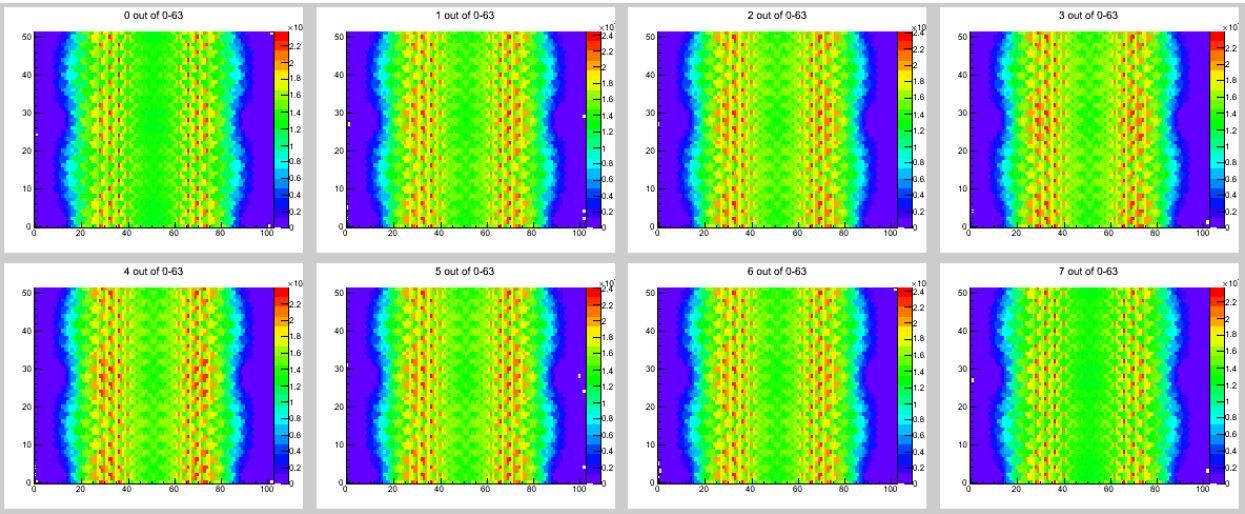

Figure 44: Sinograms from simulated uniform phantom data for the direct planes of the Plant Scanner

Using system matrix storage methods that span the lifetime of the RatCAP project, the efficiency correction software is able to read four different kinds of system matrix. The oldest format is a full system matrix, with dimensions equal to the total number of voxels to the total number of LORs. This method of data storage is inefficient, since each LOR intersects a relatively small number of voxels in its path between detectors. As a result, most elements in the matrix are zero. An improvement on the last, the sparse matrix is a series of data structures, which assign a value to a LOR-voxel pair known to have counts. Though it is more efficient, in terms of redundancy it does not take advantage of the different LORs that intersect the same voxel or voxels. This is addressed in the "standard" matrix, which stores rows of non-zero LOR elements for each voxel[70] as seen in figure 45. The current version of system matrix uses the open source Lempel–Ziv–Oberhumer (LZO) algorithm to compress the standard matrix further.

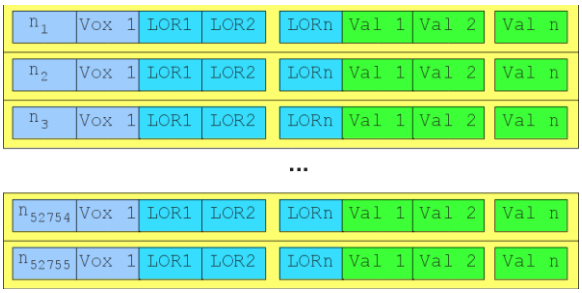

Figure 45: Organization of the "standard" and LZO-compressed system matrix. First element denotes the number of lines of response per voxel, second denotes the voxel position. Following elements indicate each LOR corresponding to voxel and their respective values[69] (©2012 IEEE)

In an effort to create a standard for all our scanners in image reconstruction, the efficiency correction sinogram writer will also read in older versions of system matrix, and convert them into our current method, For the RatCAP system matrix, the removal of all zero and redundant elements from the matrix reduces the full matrix size by a factor of ~5.7, and the LZO compression sparse reduces it further by a factor of ~1.6.

Our system matrices are generated using the Simulation System for Emission Tomography (SimSET), developed by the Division of Nuclear Medicine in University of Washington[73]. SimSET uses Monte Carlo to simulate a uniform phantom of a given activity, filling the FOV of the scanner, and records the number of counts in each voxel per LOR. The user defines the geometry of the scanner and detector modules, the scintillator type, and the material within the FOV. The simulation uses these inputs to incorporate the physical processes that affect PET scans, such as attenuation, scatter, positron range, and non-collinearity. The system matrix associated with the Plant Scanner contains 91x91x17 voxels, and uses 52 projection angles with 103 sinogram bins per projection angle, and 64 sinogram axial planes. The simulated voxel size is ~1.15 mm

The panel GUI also has stand-alone tools for image editing, specifically with datasets involving a rotation of several scanner positions. One tab on the panel is for stitching together images that have been taken at varying heights on a movable z-stage (Velmex Single Axis M02 BiSlide)[74]. The user inputs the starting position, the number of rotating positions, the length of time the scanner stood in each position, the length of time between scans while the scanner was in motion, and the number of overlapping planes in each image. The program will create a series of decay-corrected stitched images and headers from the images of the individual positions, thus extending the PET scanner's axial FOV. Another tab uses the same inputs, and creates a decay-

corrected dynamic image of scans taken in only one position in the rotation (e.g. a dynamic image of the top position, a dynamic image of the center position).

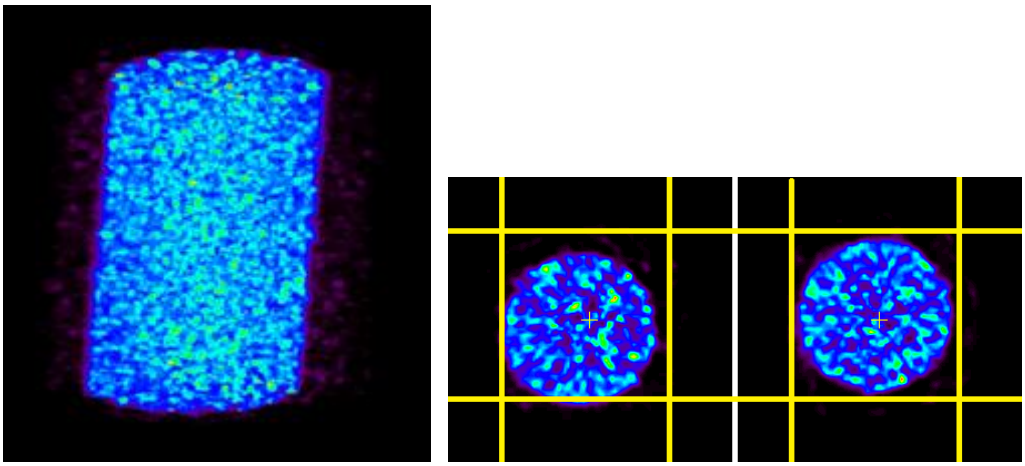

Figure 46: (Left) ^{18}F filled uniform phantom, imaged using Plant Scanner on single axis moveable stage. (Center and Right) Transaxial images of bottom and top position. Yellow lines highlight the phantom's tilt

Figure 46 is a three-dimensional view of the first time frame of a stitched uniform phantom, filled with ~1 mCi of ^{18}F. The phantom was imaged at a slight tilt (center and right figures are transaxial images of the top and bottom positions), and was imaged at six positions. The positions had two overlapping axial slices, equal to 0.24 cm, in which the pixel values were averaged. Each position was imaged for 330 seconds, with 8 seconds in between to allow the stage to reach a complete stop before scanning the next position. Once the stage reached the sixth position, the shell-scripted automated USB controller returned to the first position to resume the cycle. Since header scale factors are applied to an entire image, the stitching program edited the images to include decay correction in each position image before combining them. The total axial FOV in this demonstration reached 8.09 cm.

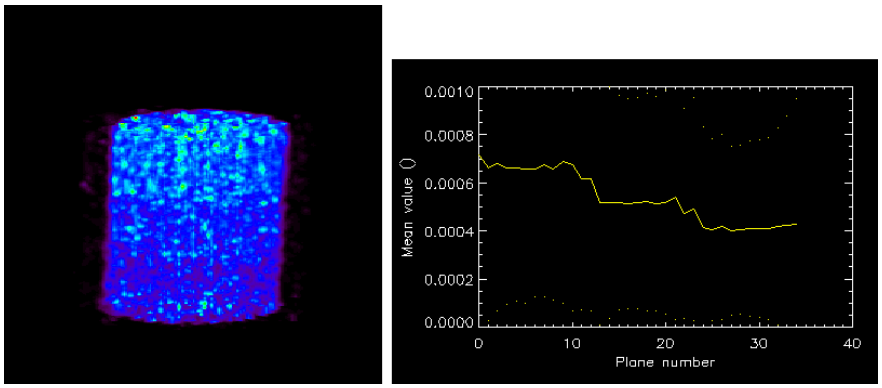

Figure 47: (Left) Top three positions of uniform phantom in figure 46, without decay correction. (Right) Axial profile of image, arbitrary units

Figures 47 and 48 are stitched images of the top three positions of the uniform phantom seen in figure 46, containing 35 0.115 cm axial planes. Each position was imaged during a different cycle of the moveable stage, setting the image of each position 39 minutes apart. Figure 47 does not apply decay correction, thus showing in its axial profile a decrease in activity by plane 13 by 1.28, and again in plane 24. Figure 48 is decay corrected, and shows an even level of activity.

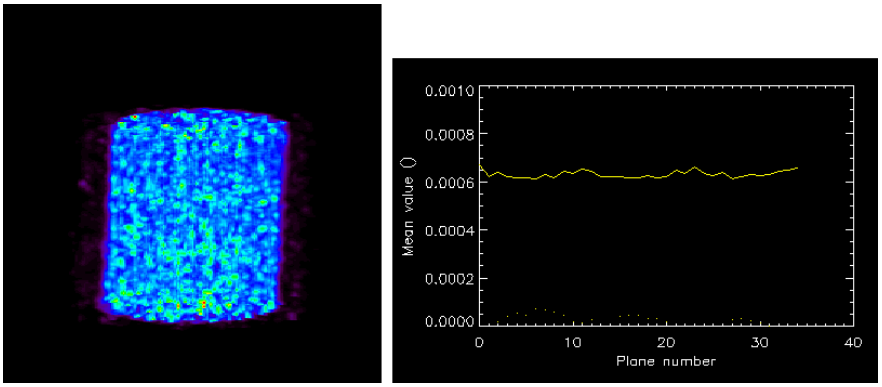

Figure 48: (Left) Top three positions of uniform phantom in figure 46, after decay correction is applied. (Right) Axial profile of image, arbitrary units

For other basic image editing, a ROOT based viewer has also been developed. The viewer can be used to see both images and sinograms, and is capable of showing up to 16 planes at once. It is useful for arithmetic operations between images or sinograms, and truncating the radius or end planes of an image. The planes within a sinogram or image can be summed to create a sinogram profile or a two dimensional projection of a three dimensional scan. Threshold and cap values can be applied to pixel values to adjust image contrast and highlight structures.

2.5 ADDITIONAL CALIBRATION SOFTWARE

The ASIC level changes are made through its 1088 bit serial programming interface (SPI). These changes include programming the gain of each channel (up to a factor of 2.7), toggling between threshold and window energy discrimination, and activating the analog multiplexer for monitoring the shaper signal. The programming instructions for the SPI is written as a text file for every flex or every tower board, depending on the scanner. The file is read and processed by the TSPM client, where it is transmitted to the TSPM, and loaded across the daisy chained ASICs. Figure 49 are snapshots of an oscilloscope, connected to the output of analog multiplexer, which has been activated for a given channel on the PET Insert. The figure on the left is the bipolar signal of a normally behaving channel, whereas the figure on the right is picking up interference from the MR RF coil.

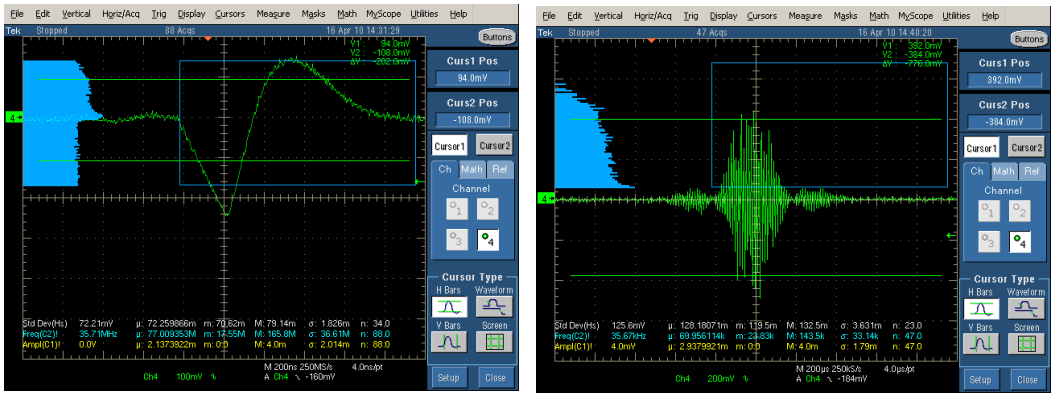

Figure 49: Output from analog multiplexer for (Left) normal emission data and (Right) RF interference

The overall gain for the system is a product of the system operating high voltage, which is determined using the specifications of each system's set of APDs. The high voltage setting is set correctly if the photopeak of every channel falls within the dynamic range. Specific gain settings can then further align the photopeaks of their respective channels more accurately. The gain for each channel is calculated using a series of data files acquired over multiple short scans, known collectively as a threshold scan. In a threshold scan, the scanner is set at a low LLD, and a short scan of a low activity sealed source is taken. The threshold is then lowered and another dataset is recorded. This sequence continues until the threshold setting reaches the baseline of the

bipolar signal. The number of singles recorded for each file is extracted for every channel, and plotted against the threshold setting of the scanner at each dataset.

During the analysis, the user must indicate which scanner is being used in order to display the appropriate number of channels, and to correctly convert the particular scanner's DAC setting to mV. This plot is then differentiated to reveal the photopeak, and to compare the threshold setting that corresponds to 511 keV in every channel. A ROOT based GUI was developed to display the integrated and differential plots, and automatically fit every photopeak with a Gaussian curve, while avoiding noisy aberrations in the Compton scatter region of the energy spectrum. The fitting algorithm saves the mean and standard deviation of each curve in a text file, so that another calibration program can calculate the gain needed to align every channel to the lowest energy photopeak. With the new gain factors programmed, an additional threshold scan is run to calculate the operating LLD, which is set to approximately 350 keV.

After running the threshold scan for the Plant Scanner, it was determined that the 511 keV photopeak on average corresponds to a 388.7 mv signal (not including hysteresis). The calculated operating threshold was set to 363.5 keV at 272.2 mv.

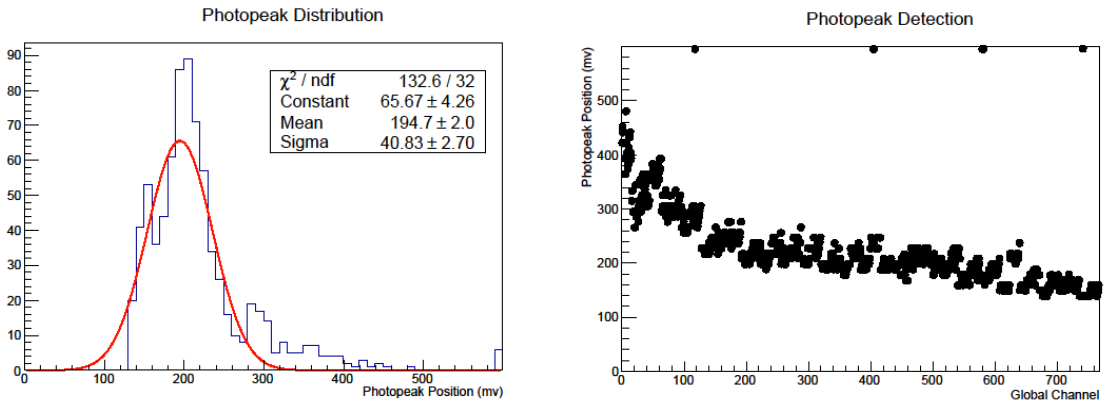

Figure 50: (Left) Distribution and (Right) plot of threshold energy (mv) position of 511 keV photopeaks for Plant Scanner, without calibration

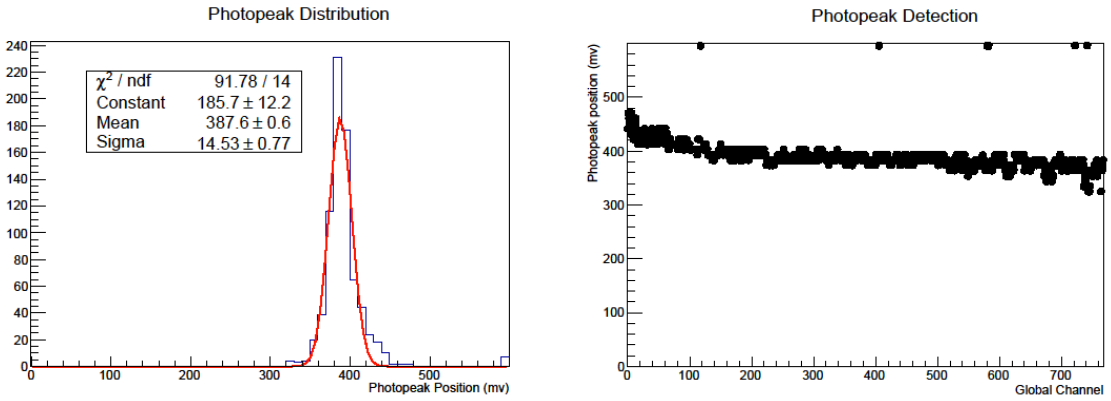

Figure 51: (Left) Distribution and (Right) plot of threshold energy (mv) position of 511 keV photopeaks for Plant Scanner, with calibration

3. Characterization

3.1 FIGURES OF MERIT

The methods used in characterizing the Plant Scanner were guided by the NEMA standard for preclinical scanners[75], whenever it was applicable to do so.

3.1.1 Spatial Resolution

The spatial resolution for the Plant Scanner was obtained as follows: A 0.3 mm^3 ~5 µCi ^{22}Na point source, encased in a metal rod, was positioned in the center of the axial FOV, and imaged at distances of 5, 10, 15, 25, and 50 mm from the center. The point source was imaged for two minutes at each position, resulting in a minimum of 10^5 prompts for each image. As the source is moved across the FOV, the PSF is expected to widen because of the angles of the detectors with respect to the active source; since the area of the detectors facing the parallel projections narrows, there are more detector elements per area in view of the activity. To compensate for this effect, both the tangential and radial values at each position are reported[76]. Raw singles data were used to create prompt and delayed sinograms, which were input for our reconstruction software, along with an efficiency correction sinogram. Our MLEM algorithm was used for image reconstruction.

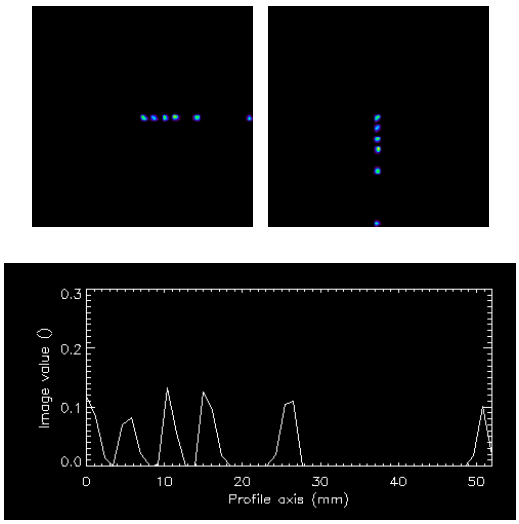

Figure 52: Sum of point source images across the (Top left) radial and (Top right) tangential FOV. (Bottom) One dimensional profile of image values for radial positions

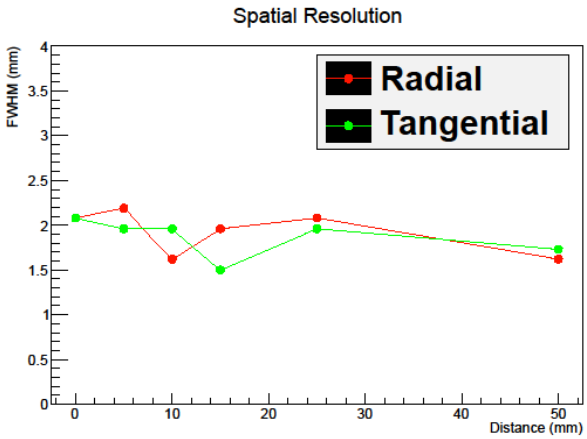

Figure 53: Spatial resolution across the scanner FOV

A one dimensional profile parallel with the radial and tangential directions were plotted individually for each imaged position of the point source. The pixel values of the image profiles were fit with a Gaussian curve, and the FWHM was reported. As a demonstration of the point source positions, figure 52 shows a sum of the different images moved across the tangential and radial directions respectively, and a profile of the summed image in the radial direction.

Figure 53 shows the image spatial resolution across the transaxial FOV. The resolution for each of the orthogonal directions is relatively uniform, and remains below 2.2 mm with an isotropic mean of 1.8 mm.

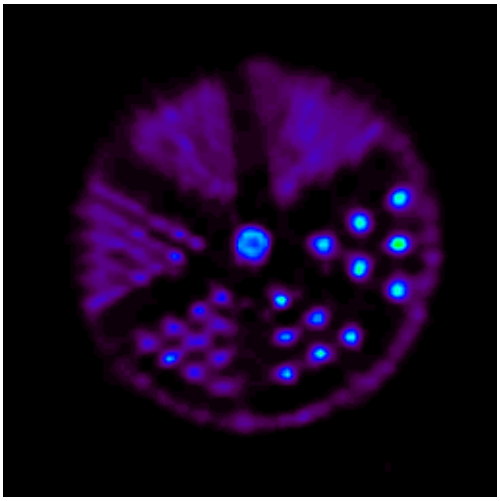

Figure 54: Image of mini-deluxe phantom, using Plant Scanner

Figure 54 shows the transaxial view of a mini-deluxe (Data Spectrum Corp., NC, USA), or resolution phantom, filled with ~1 mCi of ^{18}F-FDG, and imaged with our Plant Scanner. The

resolution phantom consists of 6 sections of rods with diameters 4.8 mm, 4.0 mm, 3.2 mm, 2.4 mm, 1.6 mm and 0.8 mm.

3.1.2 Timing Resolution

Timing resolution can be improved with a faster system clock, but is ultimately limited by the scintillator decay constant. Beyond the limitations of the scintillator, the ASICs can also introduce error into the timing.

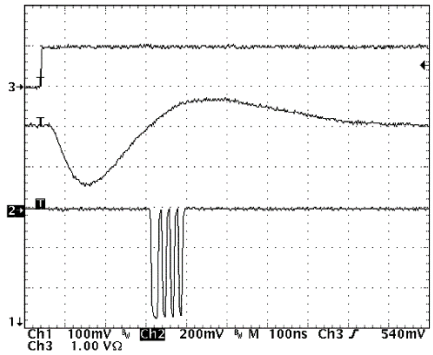

Figure 55: Oscilloscope display of (top) signal generator pulse, (center) bipolar signal, and (bottom) channel digital address[3] (©2008 IEEE)

When the analog pulse that contains the signal amplitude information, as seen in the center signal in figure 55, returns to baseline, a trigger is generated on the zero-crossing mark, creating an asynchronous edge for the digital output, followed by the channel address, as seen in the bottom signal in the figure. The edge provides the timing information for the TSPM, but is susceptible to the energy dependent variability in the zero-crossing. This is exacerbated by the uneven efficiencies in the scanner's crystals, generating different energy responses to detected photons. The BNL-UPenn System adds the difficulty of synchronizing different TSPM clocks, which includes a margin of error in the timing among the different quadrants.

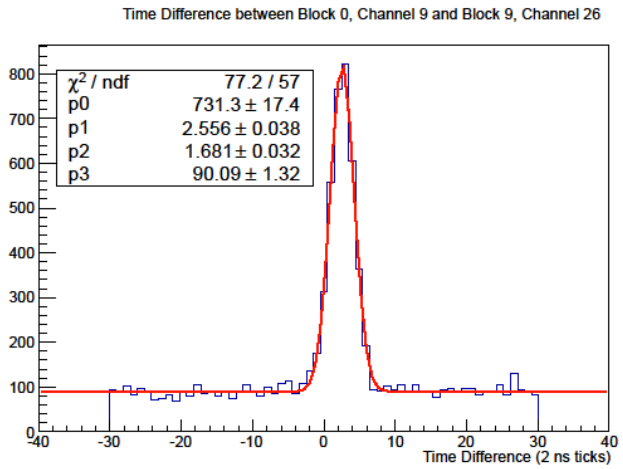

Figure 56: The time difference in incoming signals between two channels

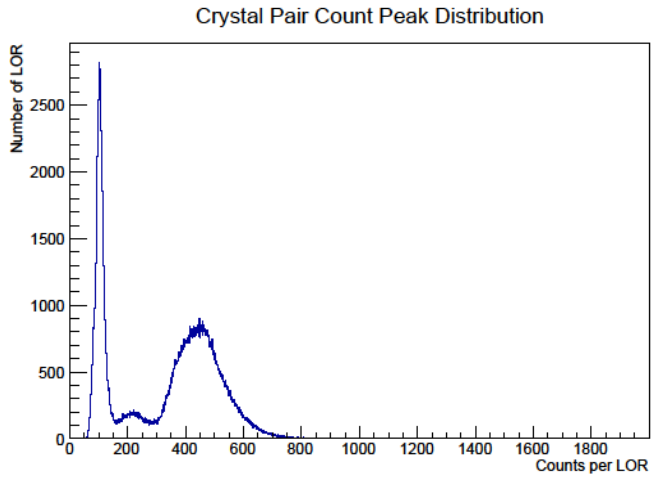

Figure 57: The distribution of the peak values for each of the time difference histograms

Figure 56 shows an example of the time difference histogram between two channels: channel 9 in block 6 and channel 26 in block 9. The mean of the time difference between the two channels is offset by approximately 5 ns (2.556 ticks * 2 ns per tick). Though the time resolution for this pair is ~8 ns, the offset in the mean, compounded by the offsets for the rest of the channel pairs, result in a much wider system time resolution. Figure 57 shows the distribution of these offsets, which can be as large as 30 ns in some channel pairs. Time correction lookup tables consider the discrepancy of signal arriving time within a scanner's detectors by matching each channel with a delay factor. This factor is then incorporated into each time stamp when read by the coincidence processor.

The corrections factors are determined using a least squares approach. A dataset in which all channels are approximately equally responsive is used to plot the time difference between

each channel pair with a significant peak (Many lines of response yield only accidental coincidences, as seen in figure 57: The spike in LORs with low counts are discounted). These differences are automatically fitted with a Gaussian curve, and the mean of each curve is read by another program which performs singular value decomposition (SVD). The resulting time zero offsets drastically improve the time resolution of the scanners.

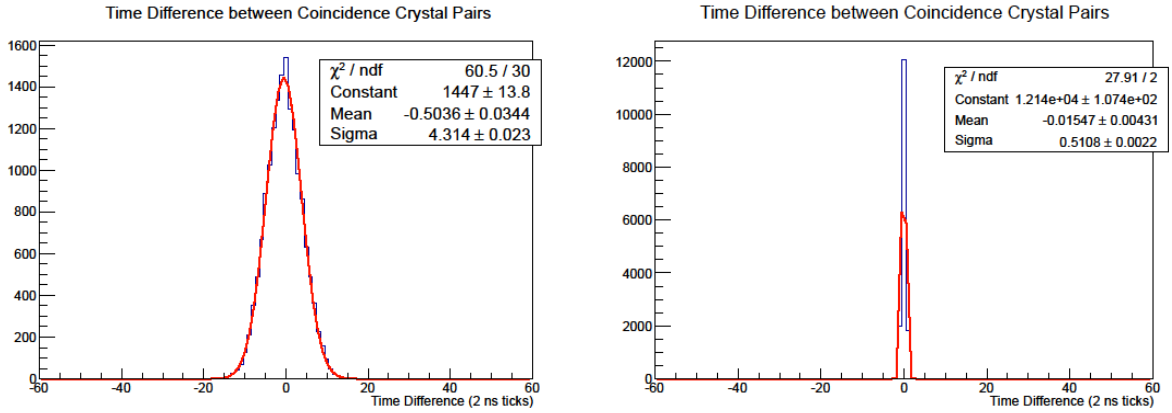

Figure 58: The distribution of the centroid values for each of the time difference histograms, before (left) and after (right) timing correction

Figure 58 shows the distribution of offsets, once the delay correction factors were applied. With the reduced offset distribution, the system time resolution, determined to be 9.9 ns FWHM, resembles more the FWHM between one crystal pair as seen in figure 56.

3.1.3 Energy Resolution

The energy resolution is determined by finding the ratio the peak FWHM to the energy corresponding to the center of the photopeak, expressed as a percentage. The energy spectrum of each channel in the Plant Scanner was generated by determining the energy of singles data from a ~15 µCi ^{68}Ge rod source, placed in the center of the transaxial FOV. Because our scanners are not currently capable of recording photon energy data, the energy from the annihilation photons are calculated by taking data at a range of LLD settings, and matching the signal amplitude of the photopeak mean, based on the threshold setting, to 511 keV.

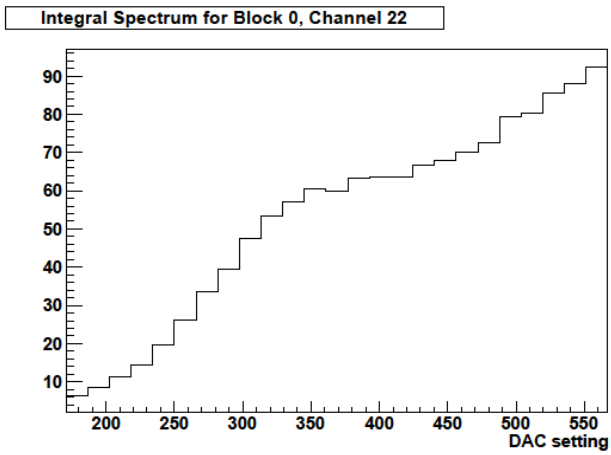

Figure 59: Integral energy spectrum for one channel

The threshold level is increased from 0 mv to 600 mv in increments of 10 mv. The voltage settings correspond to the magnitude of detector's bipolar signal: 0 mv, the most restrictive setting, corresponding to an amplitude of 600 mv below baseline, and 600 mv, the most permissive, being the baseline at which all signals are counted. Every scanner except for the Wrist Scanner achieves this through TSPM commands that control a DAC on the flex circuit or tower board. (The Wrist Scanner uses a looped shell script that issues GPIB commands to an external low-voltage source which connects to a custom TSPM adapter board.) The gain for each channel in the system must be set beforehand, so that the photopeaks for each of the scanner's discrete crystals are aligned. The derivative of the measured output signal rate as a function of energy threshold reveals the photopeak, which can be fitted with a Gaussian curve. The energy resolution is then determined by finding the ratio of the peak FWHM to the threshold setting corresponding to the center of the photopeak.

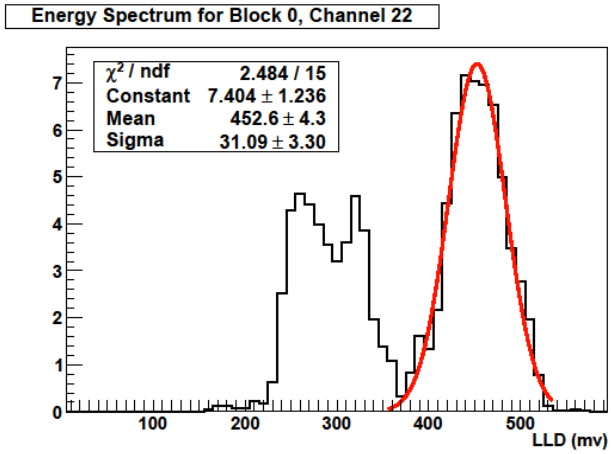

Figure 60: Energy spectrum for one channel

Figure 59 shows the integral spectrum for channel 22 in block 0, in units specific to the DAC. (For the BNL-UPenn System, the 12 bit setting applies a voltage from 0 to 1.25 V in 4096 steps. For the rest of the systems, the range goes from 0 to 2.5 V). The energy spectrum in figure 60 converts the setting into mV, and measures the magnitude of the pulse, rather than the LLD applied to the bipolar signal. The energy resolution of the channel shown is 16.2%. The energy resolution for each channel in the system can be seen in figure 61; the mean energy resolution for the system is 15.8%, and appears to be uniform throughout the system.

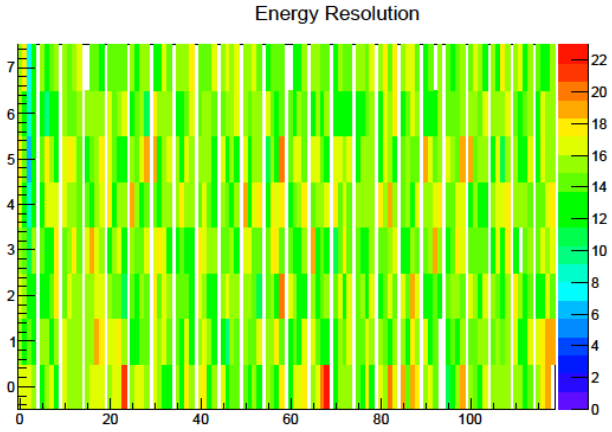

Figure 61: The energy resolution across the system block detectors

3.1.4 Sensitivity

A system's sensitivity is expressed as a rate of true coincidence detection for a given amount of activity. Sensitivity is calculated by placing a radioactive source in the scanner FOV, and taking the ratio of the detected true coincidences, excluding true coincidences attributable to background activity, to the activity of the source. Since the activity of some sources are not purely β+ decay, the absolute sensitivity takes the ratio of the calculated sensitivity to the source branching fraction, expressed as a percentage:

$$\frac{R_i - R_{B,i}}{A * B_A} \; x \; 100$$

Where R_i is the trues rate, $R_{B,i}$ is the background trues rate, A is the activity in Bq, and B_A is the branching fraction (0.9060 for ^{22}Na). The activity must be low enough as to not incur more than 1% counting losses, and the randoms rate must be less than 5% of the trues rate[16].

A 5.6 µCi ^{22}Na point source was transaxially centered in each scanner, and moved across the axial FOV in steps of 2 mm. A scan lasting 30 seconds was taken in each position[15], and the sensitivity was calculated at each point (The LLD was set to 363.5 keV).

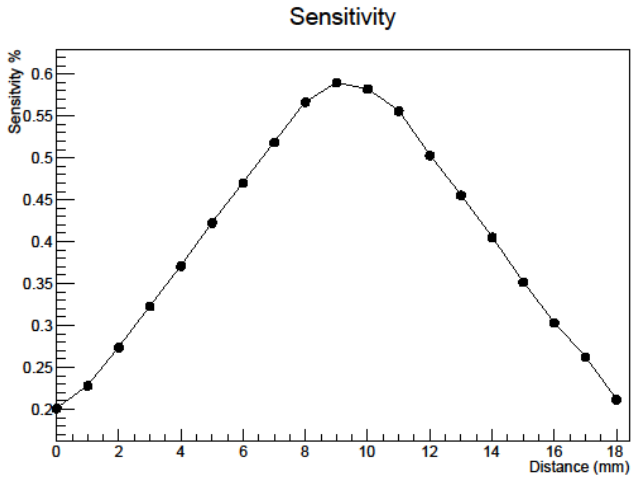

Figure 62: Sensitivity profile as a function of axial position

The axial sensitivity profile shows the maximum sensitivity at the center of the axial FOV, at approximately 0.6%, which gradually decreases towards the scanner axial edges to 0.2%. The effect of the energy threshold on sensitivity was also explored, by calculating the absolute sensitivity in the center of the axial FOV at a range of LLD settings (98 to 293 mv) corresponding to energy levels between 150 to 375 keV:

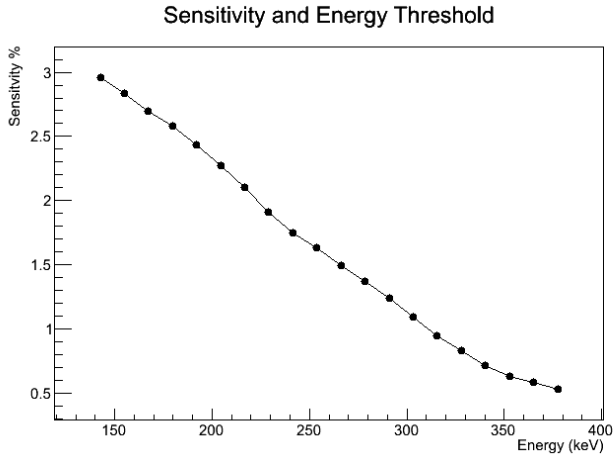

Figure 63: Sensitivity as a function of LLD

As seen in figure 63, the sensitivity can increase up to 2.9% when photon energies as low as 150 keV are accepted. However, as seen in the energy spectra of the system's channels, the

increase in sensitivity may be attributable to the acceptance of more scattered events, which can impoverish the reconstructed image SNR.

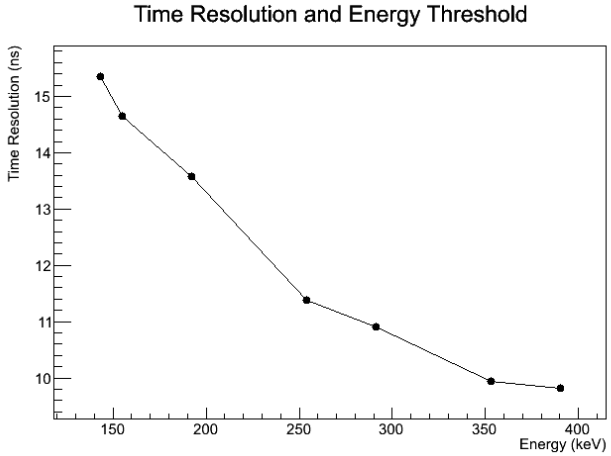

Figure 64: Time resolution as a function of LLD

In figure 64, the FWHM of the time difference between prompt coincidences is plotted for data taken at 7 LLD settings spanning 150 to 350 keV. Each data set contains 10^5 prompts of the same ^{22}Na used for the sensitivity calculation. Using a 150 keV energy threshold results in a 15.4 ns time resolution FWHM, in contrast to the system's ~10 ns resolution during normal operation. The increase in sensitivity when using a more permissive threshold may exacerbate the variability of the signal baseline zero-crossing within the system's channels.

3.1.5 Noise Equivalent Count Rate and Deadtime

The noise equivalent count rate is a system estimate of the SNR, independent of method of image reconstruction used. It is used to estimate the trues rate once the scattered and random coincidence contribution is removed. To calculate it, a uniform phantom filled with ^{18}F-FDG was left to decay inside the PET camera. We approximated, based on experience with past scanners, that the scatter rate is approximately 20% of the trues rate. Figure 65 shows the peak NECR to be 25 kcps at 1.2 mCi.

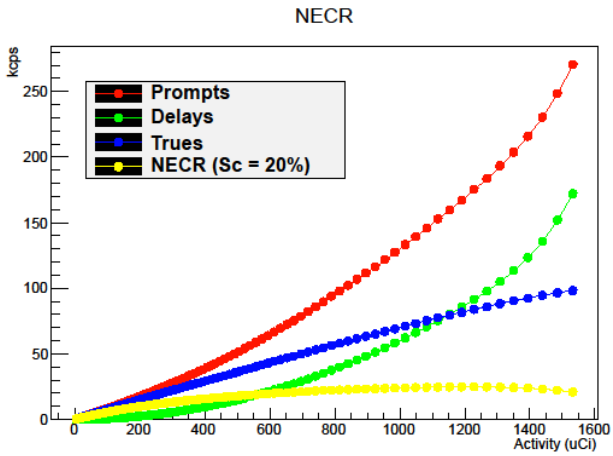

Figure 65: Count rate capability as a function of source activity

Overall deadtime, which includes the transmission deadtime, can also be derived from the uniform phantom dataset, by using the trues rate under low count rate conditions to extrapolate the expected trues rate without deadtime, and comparing it to the actual trues rate[52]. The function defining the expected trues rate was calculated for activity under 0.4 mCi, where the counts increased linearly with more activity. Under this definition, the percent deadtime at 1 mCi is 6%.

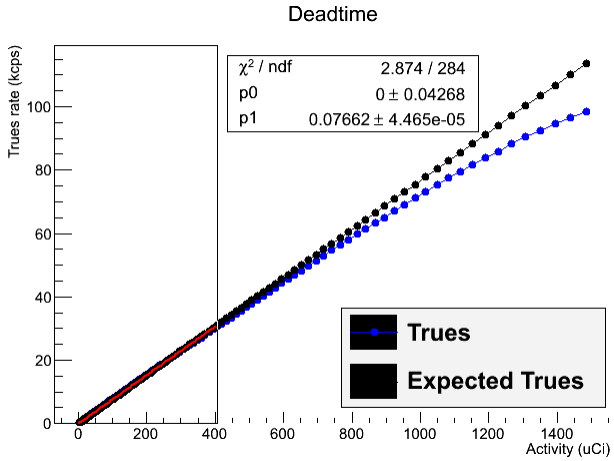

Figure 66: Expected and acquired trues rate as a function of source activity

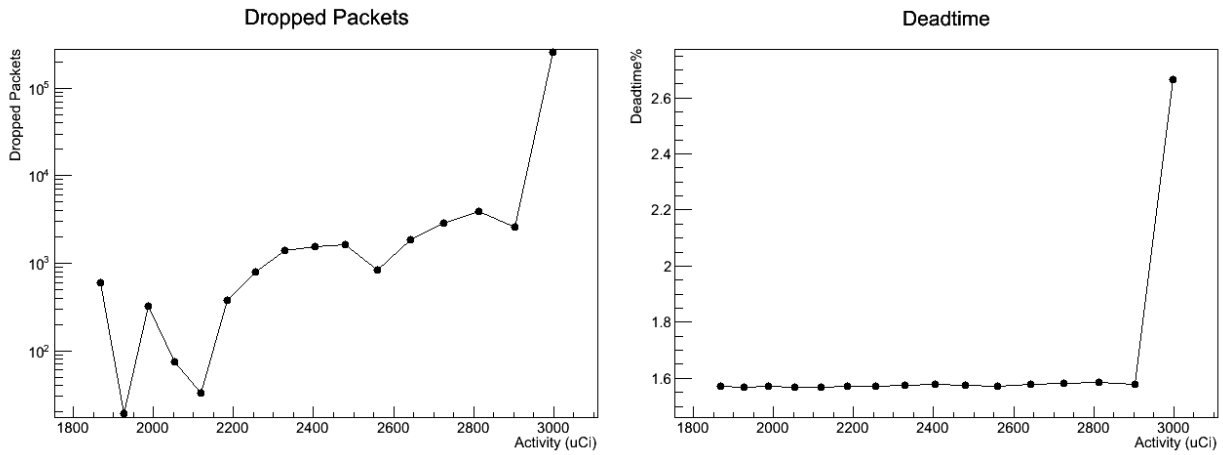

Figure 67: (Left) Logarithmic plot of dropped Ethernet packets, each packet 1 kB, as a function of source activity. (Right) Transmission deadtime as a function of source activity

The loss of UDP packets is more prevalent at higher data rates. For a 3 mCi source, which is far above the usual activity used in experiments (>1 mCi), where the count rate reaches 9.4 million counts per second, up to 2.6% of the scan time is lost. This rate of data acquisition, averaging at 74.6 MB per second, resulted in the loss of 254 MB in 5 minutes, equivalent to 8 seconds of lost data. For sources below 3 mCi, the transmission based deadtime is typically below 1.6%. At count rates below 3.46 million counts per second at 1.27 mCi, or 27.4 MB per second, where no packets are lost, the transmission deadtime plateaus to 1.56%, which is attributable to the time spent sending the filled TSPM buffer through the Ethernet controller.

3.1.6 Absolute Quantification

For absolute quantification, a uniform phantom filled with fluorine-18 radiolabeled fludeoxyglucose (^{18}F-FDG) was scanned until the activity fully decayed. After the scan, several samples of the ^{18}F-FDG solution was taken and counted in a dose calibrator and weighted, so that the activity concentration for the phantom could be determined. A portion of the data taken from the phantom with minimal deadtime and random coincidences was reconstructed using efficiency correction. Large regions of interest (ROI) were drawn across the planes of the image, taking the sum of the unitless voxel values and using the image dimensions to calculate the concentration per cubic centimeter. The ratio of the sample concentration to the voxel value concentration provided the calibration factor for future images.

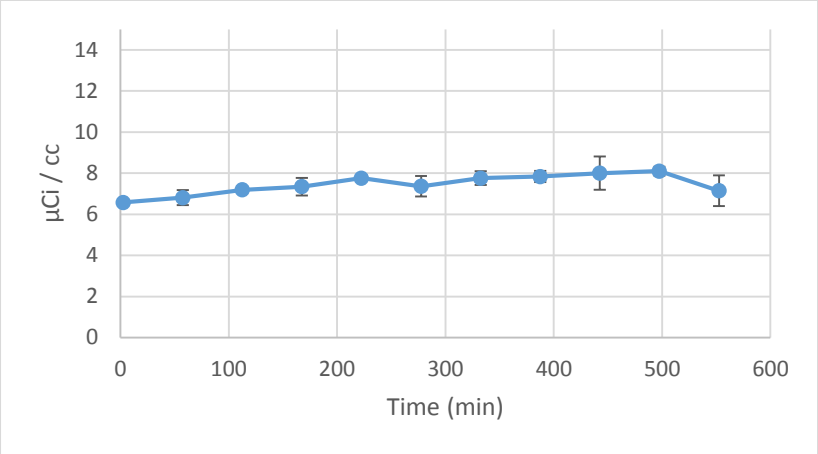

Figure 68: Decay corrected time activity curve of ^{18}F uniform phantom, with activity concentration calibration factor

The mean value of the aliquot samples, decay corrected to the first time frame of the reconstructed image was 6.9 µCi, with a standard deviation of 0.2. The calibration factor was included in the header for a dynamic image of the ^{18}F uniform phantom, and a ROI with an area typically used for sorghum plant experiments was drawn in the transaxial center, in three axial locations. The time activity curve of the decay corrected image was plotted for five half-lives. The error bars indicate the standard deviation of the activity concentration at the three positions. The maximum variation seen due to axial position was 9% of the mean.

3.2 IMAGE STUDIES

3.2.1 Plant Scanner

We have shown the efficacy of the Plant Scanner in a series of imaging studies, using corn, pea, and poplar plants, in collaboration with the Department of Biological, Environmental, and Climate Sciences in BNL. In one experiment using corn, a leaf that was gassed with ^{11}C-carbon dioxide was cut and imaged after an uptake period, to show the distribution of the isotope within the leaf. This was compared to a radiographic image of the same leaf. The area of the leaf in which the cuvette administered the radioisotope is indicated by the markings on the leaf in the photograph in figure 69.

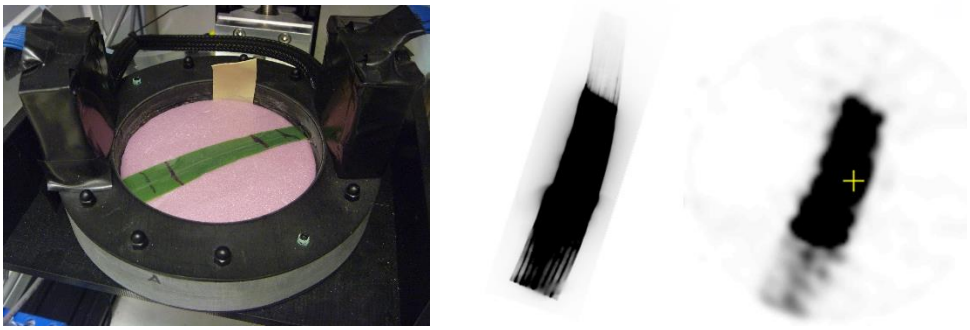

Figure 69: (Left) A corn leaf within the PET scanner that was cut one hour after ^{11}C-carbon dioxide uptake. (Center) A radiographic image of the same cut leaf. (Right) a PET image taken with our scanner, confirming the radiograph results of the distribution of the radiotracer[8]
(©2013 IEEE)

Two studies were conducted using poplar leaves. In the first, a poplar leaf was cut off, and its petiole was placed in 100 mL of water containing 0.13 mCi of ^{18}F-fluoride. The uptake period lasted 45 minutes, and was followed by a flushing period, where the petiole was submerged in water with no activity. The petiole was then cut, and the leaf was imaged for one hour (figure 70).

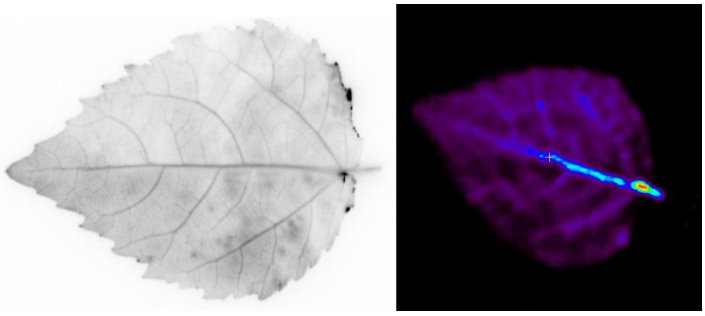

Figure 70: The radiographic image (left) and the PET image (right) of a poplar leaf[8]
(©2013 IEEE)

In the second, a poplar leaf was cut off from a different plant, and its petiole was placed in 0.25 mL of water containing 0.9 mCi of ^{18}F-FDG. The uptake period lasted one hour, and the petiole was left intact. The scan lasted one hour (figure 71).

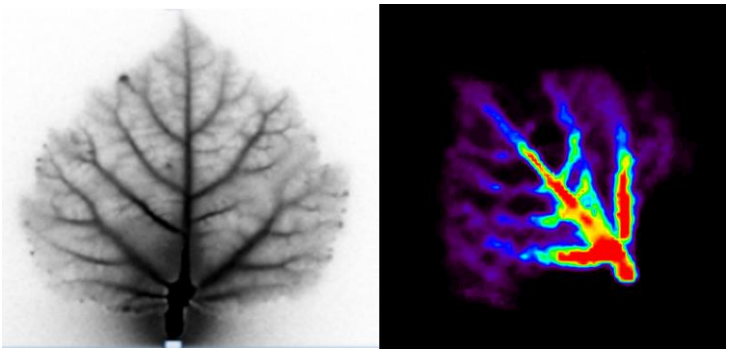

Figure 71: The radiographic image (left) and the PET image (right) of a poplar leaf[8]
(©2013 IEEE)

In a static study of the corn plant, the corn stem was imaged one hour after a dose of ^{11}C-carbon dioxide to a higher leaf using the leaf cuvette. The scanner was placed at a height where the stem bifurcated into several leaves (figure 72)

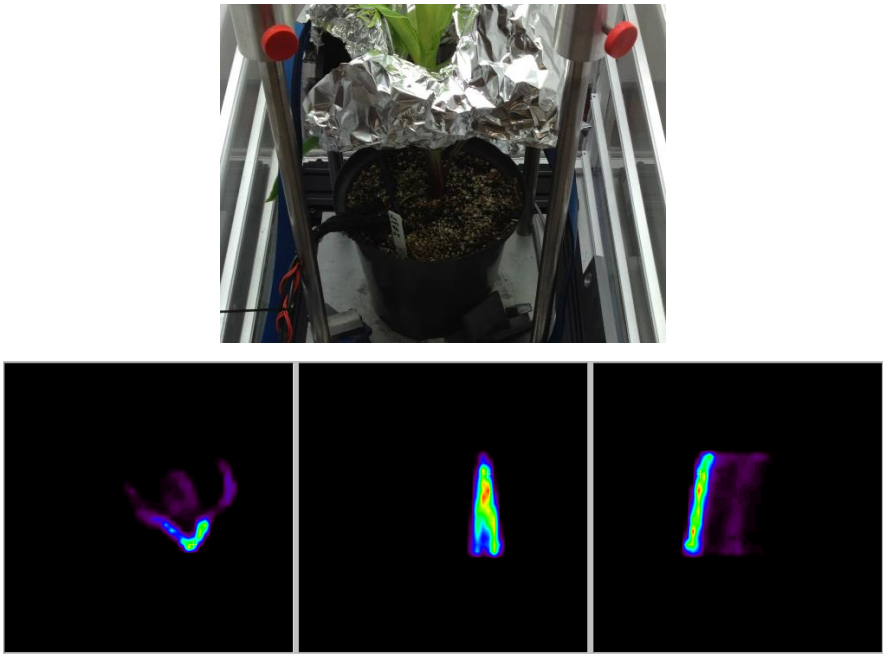

Figure 72: (Above) A corn plant positioned within our PET scanner. (Below) Three orthogonal views of the above corn plant experiment. The left image is the cross section of the plant (transaxial). The center and right images are the longitudinal images, coronal and sagittal respectively[8] (©2013 IEEE)

Several experiments were conducted to demonstrate the scanner's capability for dynamic studies, which can highlight different aspects of plant biology. In order to explore the transport within the corn plant, a corn stem was imaged immediately after a dose of ^{11}C-carbon dioxide to a higher leaf. The corn leaves were left intact while the photoassimlates were transported throughout the plant. The scan was divided into ten minute frames, and a time activity curve was generated for two regions of interest, drawn at two different heights on the stem. Results show a gradual increase of activity throughout the plant, with more activity seen moving towards the roots (figure 73).

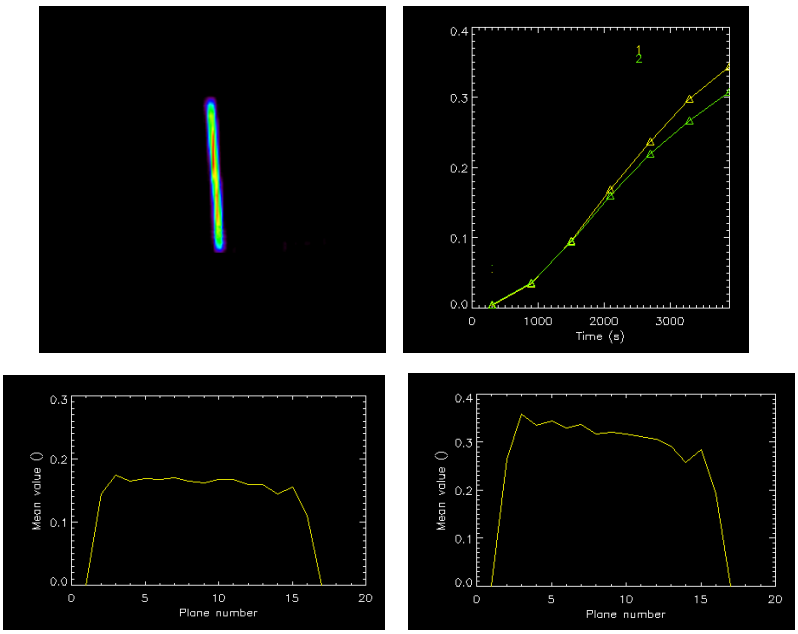

Figure 73: (Top, left) A projection view of a PET image of the corn stem. (Top, right) A time activity curve, drawn 5.6 mm (yellow) and 13.9 mm (green) from the bottom of the scanner. A plot of activity throughout the cross sectional planes of the scanner, taken 30 minutes (bottom, left) and 1 hour (bottom, right) into the scan, are shown[8] (©2013 IEEE)

In a similar experiment, a pea stem was imaged immediately after a dose of ^{11}C-carbon dioxide to a higher leaf. In contrast to the corn experiment, the stem apex, above the scanned region, which did not directly receive the dose, was cut off before the scan. The time activity curves generated for different regions of interest show an accumulation of activity in an emerging bud on the stem, which can be interpreted as the pea plant's response to the stem apex removal (figure 74).

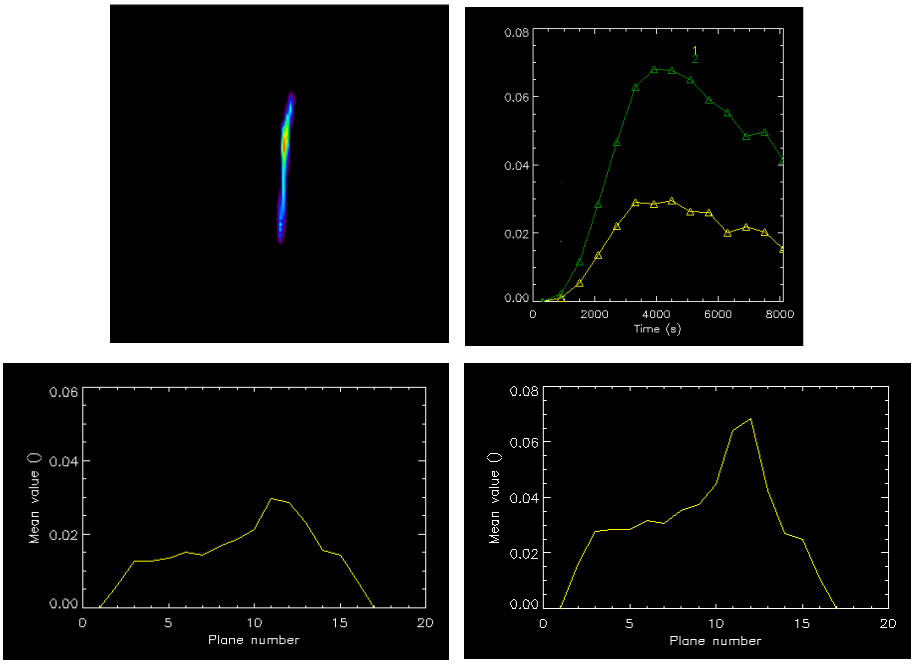

Figure 74: (Top, left) A projection view of a PET image of the pea stem. (Top, right) A time activity curve, drawn 5.6 mm (yellow) and 13.9 mm (green, at the height of an emerging bud) from the bottom of the scanner. A plot of activity throughout the cross sectional planes of the scanner, taken 30 minutes (bottom, left) and 1 hour (bottom, right) into the scan, are shown[8] (©2013 IEEE)

3.2.2 PET Insert

The PET scanner and RF coil, cased within a plexiglass tube, is placed inside the bore of the MR through one side, while the subject animal is held in a 3D printed holder and fed into the other side. The holder is made to fit directly inside the RF coil in the center of the Bruker Biospin 210-mm diameter clear-bore, 9.4 T small animal MRI scanner (94/20, 400.32 MHz proton frequency, Magnex Scientific). Our RF coil, (Helmholtz cross-coil pairs operating in transceiver quadrature mode[6]) fits within the PET system, creating a FOV of 32 mm in diameter. The MR axial FOV is 27.4 mm.

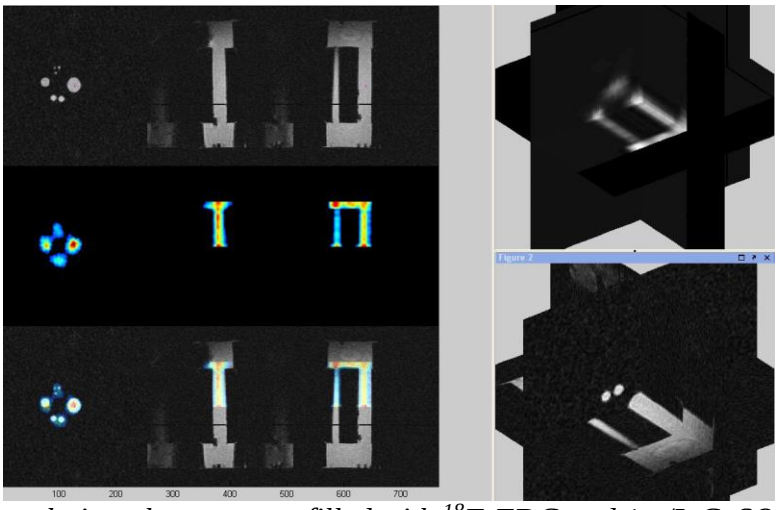

Figure 75: A resolution phantom was filled with ^{18}F-FDG and 1 g/L $CuSO_4$ solution, and scanned with simultaneous PET/MR

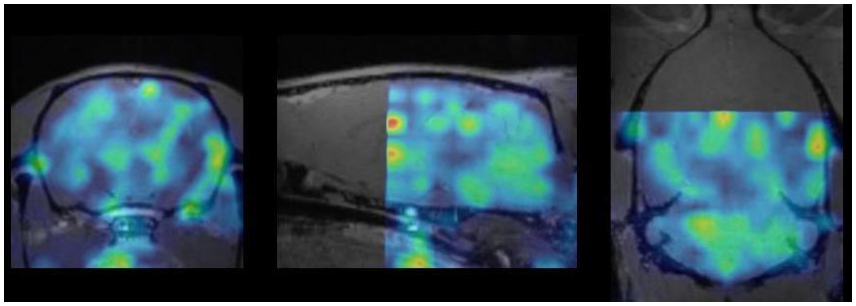

Figure 76: Co-registered, simultaneous PET-MR image of rat brain, i.v. injected with ^{18}F-FDG, using PET Insert, run alongside a 3D T1-weighted FLASH MR sequence

In one experiment, in collaboration with the Department of Anesthesiology in Stony Brook University, a solution of Gd-DTPA MR contrast agent and 0.50 mCi of ^{18}F-FDG was injected into an anaesthetized rat through an intrathecal catheter to investigate the role of the glymphatic pathway in the removal of waste products in the brain. A PET scan was then run for 90 minutes alongside a series of 5 minute 3D T1-weighted FLASH MR sequences in order to dynamically trace the paired movement of the solution (figures 77 and 78).

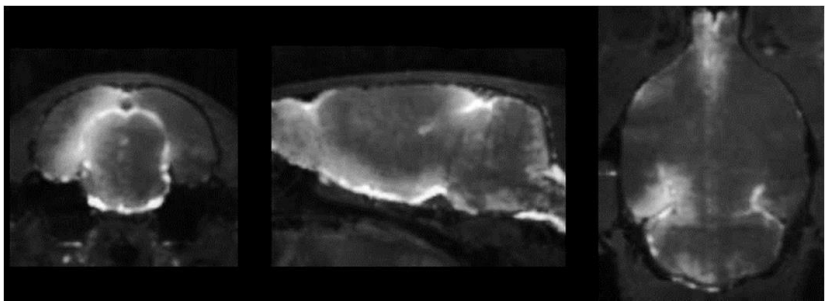

Figure 77: MR image of a rat brain, i.t. injected with Gd-DTPA contrast agent, after one hour of uptake. Contrast agent was administered into lumbar intrathecal lumbar space

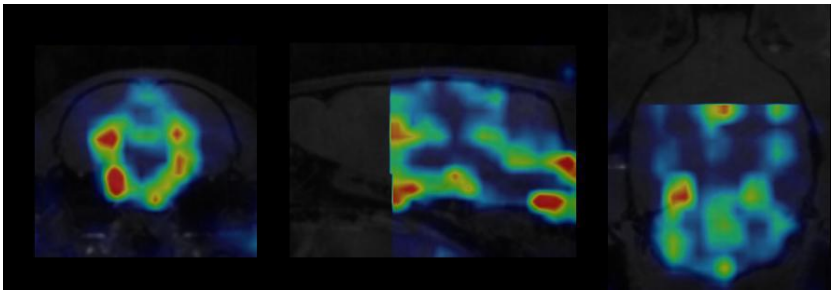

Figure 78: The co-registered PET Insert image resulting from the scan shown in figure 77. Results coincide with the distribution of the contrast agent, with activity remaining within the locations of glymphatic transport

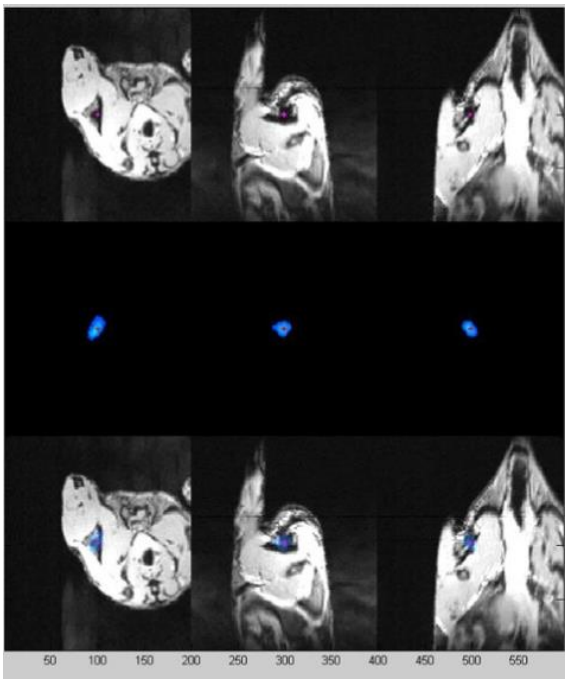

Figure 79: MR image (top), PET image (center), and co-registered PET-MR image of a mouse, s.c. injected with ^{64}Cu-SPIO.

In another experiment, in collaboration with the Department of Medical Radiation Physics in Lund University, superparamagnetic iron oxide (SPIO) was used as a MR contrast agent to target the sentinel lymph nodes of a mouse. The use of this contrast agent has the potential to detect metastases in the lymphatic system. When SPIO is coupled with ^{64}Cu, it is possible to image these metastatic nodes both with PET and MR, thus improving its diagnostic utility. The solution of radiotracer and contrast agent was injected in the hind paw of the anaesthetized mouse, and the mouse was imaged in our PET-MR system, 6 and 24 hours after injection (figures 80 and 81).

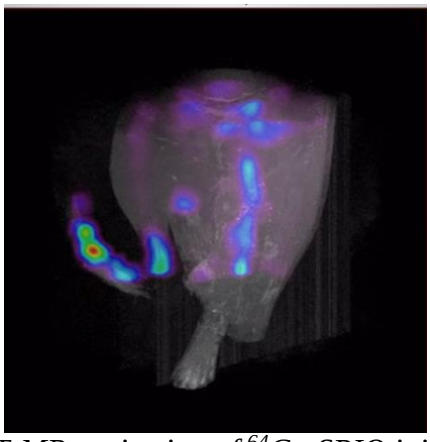

Figure 80: 3D coregistered PET-MR projection of ^{64}Cu-SPIO injected mouse. S.c. injection site is on the right paw. Several lymph nodes can be seen along the spine.

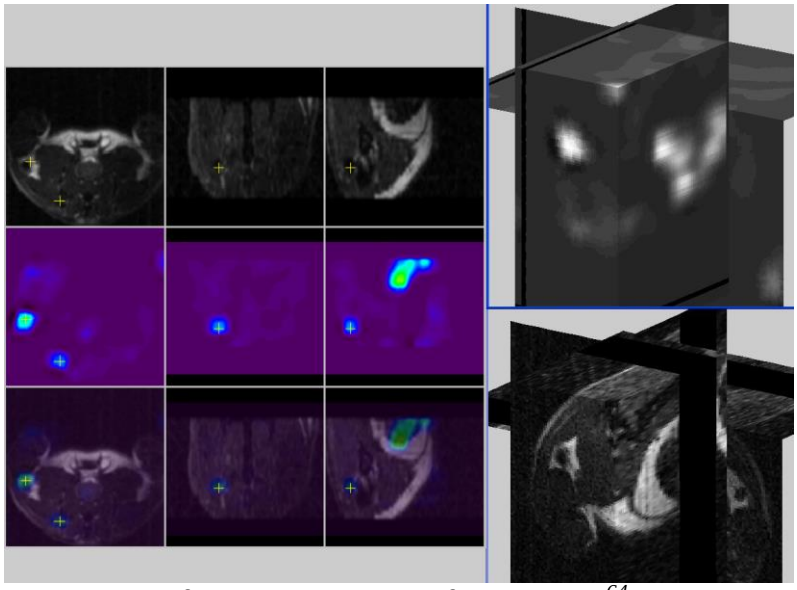

Figure 81: PET-MR images of lower pelvic area of a mouse in ^{64}Cu-SPIO s.c. injected mouse.

In figure 81, yellow crosshairs point out the sentinel lymph nodes on the mouse's right side. Both nodes show the same combined effects (radiotracer and SPIO accumulation in the

PET and MR images respectively), which suggests the binding of the radiotracer to the SPIO particle, and its sequestration by the sentinel lymph nodes. 3D view of image, using the three orthogonal views, can be seen in the right column.

3.2.3 RatCAP

^{18}F-FDG Studies Investigating Methylphenidate Treatment in Rats

In a collaborative effort with the Behavioral Neuropharmacology and Neuroimaging laboratory in Stony Brook University, the RatCAP was used for a series of experiments to explore the use of methylphenidate (MP, commonly known as Ritalin) in the treatment of Attention Deficit Hyperactivity Disorder (ADHD). The rat (Sprague Dawley) was used as an animal model in the investigation of orally administered doses of MP, and its effect on metabolic activity in the brain. By including the drug at varying concentrations in the drinking water of the rodent experimental groups (MP drinking paradigm) rather than administering it intravenously, the level of MP in the rodents' blood plasma throughout the timeline of the experiment is more comparable to the levels seen in the treatment of human patients[77]. This paradigm allows for extended studies, where the treatment period can last several months, and the metabolic response is measured weeks after the treatment period.

Figure 82: Experimental setup of the RatCAP with an anesthetized subject rat

The RatCAP was used to measure the metabolic response to the treatment period. On the day of the scan, the rat is injected intraperitoneally with ~700 µCi ^{18}F-FDG. After a 30 minute awake uptake period, the rat is anesthetized with isoflurane and placed inside the PET camera. The rat brain is then scanned for 30 minutes. For anatomical mapping, the resulting static PET image is registered with an MR image taken prior to the scan.

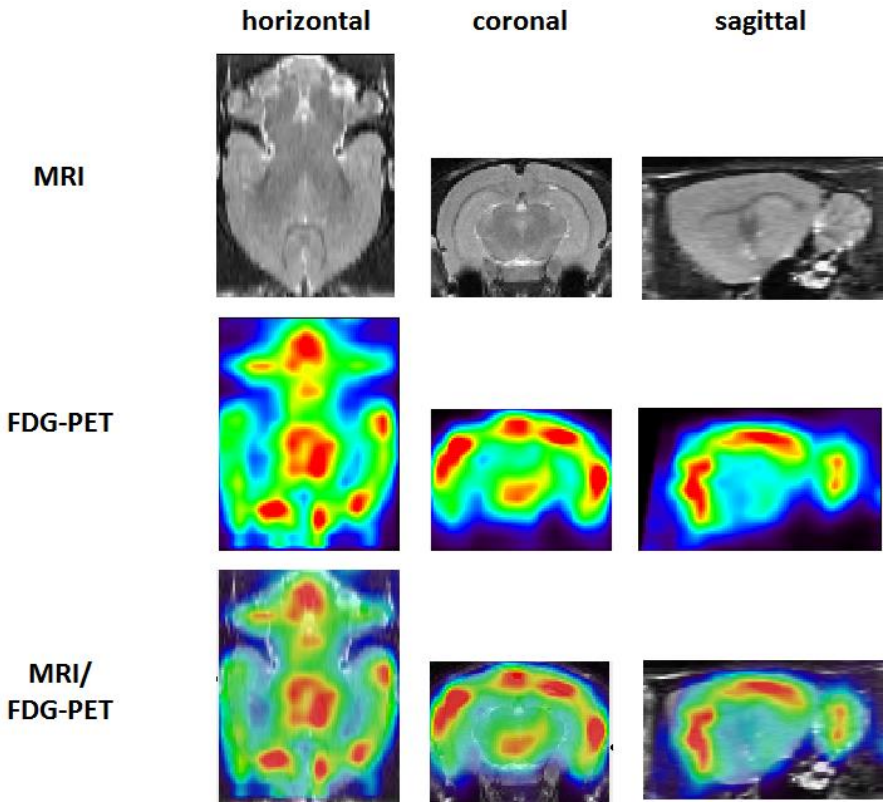

Figure 83: MR, PET, and co-registered images of rat brain from control group, i.p. injected with ^{18}F-FDG (MP not included in drinking water)

Metabolic activation was measured by isolating clusters in the brain image, and measuring the difference in uptake between the experimental and untreated control groups. Initial analysis shows that long term MP treatment can result in altered activity for regions in the brain involving reward, memory, and sensory processing.

Dopamine Studies in Rats

In addition to FDG studies which measure glucose metabolism, the RatCAP has also been used in radiotracer experiments that image neurotransmitter uptake in specific receptors in the rat brain. Dopaminergic transmission has been an important subject for neuroscience, because of its role in movement, cognition, addiction, and neurological diseases, such as schizophrenia and Parkinson's disease. Because of the ability to synthesize positron-emitting radioligands which bind to dopamine receptors, PET has emerged as an essential tool in the investigation of the dopamine pathway. In a collaboration with the Medical Department in BNL, our group has researched the use of ^{11}C-(+)-PHNO, an agonist radioligand with an affinity for one of the five G-protein coupled dopamine receptors, the D3R. Because of this specific receptor's role in motivation and reward, PHNO has been valuable in the investigation of addictive disorders[78,79].

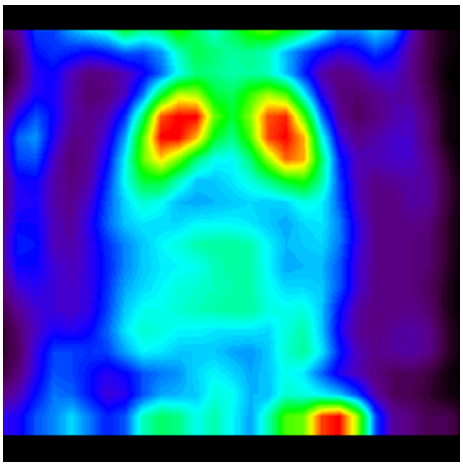

Figure 84: Coronal image of awake rat, i.v. injected with ^{11}C-(+)-PHNO

Our studies involved the rate of injection of the PHNO radioligand, in an effort to establish an uptake equilibrium in the striatum and cerebellum. The method of injecting a bolus of tracer, followed by a constant low infusion rate was used on an awake rat, and on the same rat under anesthesia the next day.

The ratio of bolus to constant infusion in this example was 30:70; 30% of the PHNO solution was injected at a maximum of 50 ul/min, and 70% of the solution was injected slowly throughout the entirety of the 90 min scan. Ketamine/xylazine was used in imaging the anesthetized rat. In both awake and anesthetized studies, the uptake was higher in the striatum

than the cerebellum. However, as seen with previous studies with the D2 antagonist radioligand ^{11}C-Raclopride, the uptake of radiotracer in the striatum in the anaesthetized rat appears to rise before reaching equilibrium.

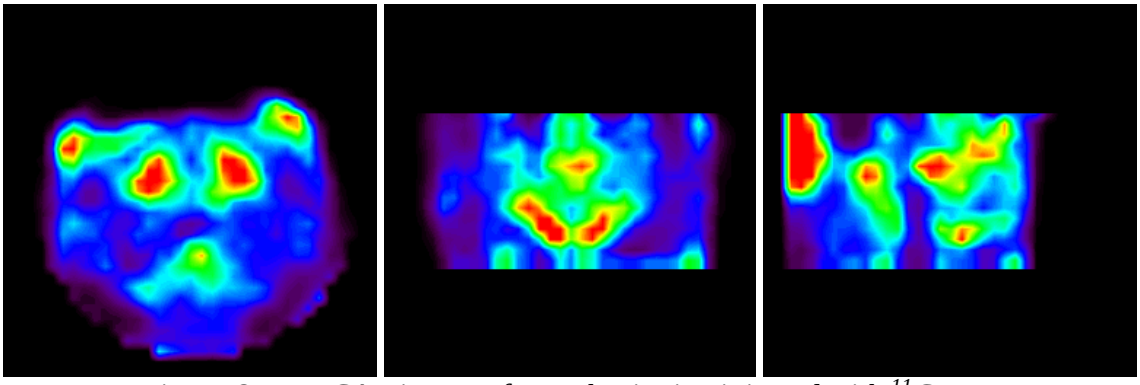

Figure 85: RatCAP image of a rat brain, i.v. injected with ^{11}C-FLB

The $D_{2/3}$ receptor antagonist ^{11}C-FLB has also been explored in awake animal imaging. With a higher affinity than ^{11}C-Raclopride, it is an effective radiotracer in the study of the role of dopamine in learning and reward[80]. A pilot experiment in collaboration with the Psychiatry Department in Yale University has been conducted to explore the possibility of using FLB in maze studies with the RatCAP. 1.1 mCi of the tracer was injected in 0.2 ul into the awake rat, followed by a 600 ul saline flush. The rat brain was imaged for 90 minutes. Figure 85 shows the results of the scan, displaying significant uptake in the striatum. Future experiments will correlate the tracer uptake with the behavior of the rat while it attempts the maze.

Bird Studies

In a collaboration with the American Museum of Natural History, the RatCAP was used to trace the evolutionary history that connects modern birds with the dinosaurs from which they descend. The project uses PET to localize the activities of the starling brain while flying in a wind tunnel, in order to better understand the neural mechanisms involved in flight. The findings of these studies will be compared with the fossil record of the brains of avian ancestors to investigate how different areas of the brain transformed over time to develop the capability of flight.

Figure 86: Wind tunnel used for flight experiments with the RatCAP

The starling was injected with ~750 µCi of ^{18}F-FDG, and placed in a windtunnel during a ten minute uptake period, where it would fly for several quick intervals of time. Afterwards, the RatCAP was attached to the starling head for awake animal imaging. The distribution of activity in the resulting images was compared with a video recording of the starling's various behaviors during the flying period.

For our pilot study, we tested the feasibility of the project with an anaesthetized starling, and scanned the brain during tracer injection. Because of the high levels of glucose in the starling bloodstream, the uptake of radiotracer is quickly diminished in the brain out after injection. To prevent FDG removal from the brain in later studies, the starling was injected with 0.1 mL of insulin 30 minutes prior to the ^{18}F-FDG injection. By using insulin in an anaesthetized starling study, the uptake of radiotracer was able to maintain an equilibrium after injection. The results of the anesthetized pilot study are shown in figures 87 and 88.

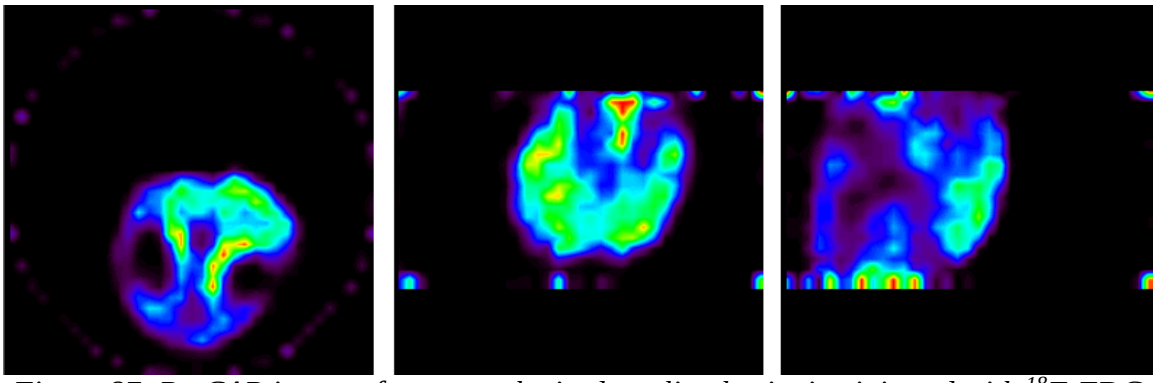

Figure 87: RatCAP image of an anaesthetized starling brain, i.v. injected with ^{18}F-FDG

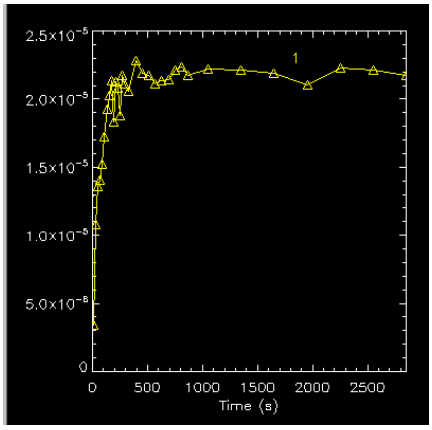

Figure 88: Time activity curve of anesthetized starling brain, during ^{18}F-FDG i.v. injection

4. Conclusions

4.1 FUTURE WORK

4.1.1 Upgrade to Plant Scanner Gantry

The current configuration of the Plant Scanner has a great advantage for studying plant physiology since it fits inside a plant growth chamber. Removing the plant from the controlled environment where it was maintained, transporting it over 100 meters to the PET facility and placing it in a horizontal orientation in more traditional PET scanners such as the MicroPET scanner are major disruptions that have physiological effects on the plant, which could possibly mask the effects of genotypes or treatments that we intend to study. With this Plant Scanner in the plant lab, we are able to keep the plant in a vertical orientation and maintain the carefully controlled environment while carrying out these studies. In addition, the moveable stage allows the scanner to move up and down the plant over a distance of about 1 meter. With this capability we can observe the dynamic transport of photoassimilates down to the roots or transport of materials from the roots upward in the plant[8].

Past experimental setups involved the investigator moving the stage to its highest position, sliding the plant into the scanner, and repositioning the PET camera to the area of the plant which the investigator intends to image. Since these experiments often involve larger plants, such as corn or sorghum, the process of moving the plant subject into position can often be difficult, and may potentially damage the plant. Taking advantage of the two flex-circuit configuration of the Plant Scanner, along with the two virtual blocks incorporated in data collection which places a short distance between the circuits, it is feasible to create an enclosure for the PET front-end, which can open and allow the plant to enter the FOV. Once positioned, the ring can then close, and begin scanning. Such an enclosure must be light tight to protect the APDs from ambient light, and consistently preserve its dimensions after every opening. The enclosure would use a hinge on one side, protected by an expandable light shield, and a locking mechanism on the other, which maintains the FOV diameter and relative distance between the block detectors.

4.1.2 Comparison with STIR Software

Since the beginning of the RatCAP project, the projection data from our scanners have been reconstructed using our own custom MLEM software. However, there is other software, using a variety of different reconstruction algorithms, available for image processing that may prove valuable in our analysis. In addition, until now, our scanners have been sufficiently small for our software to read in a system matrix from file and perform calculations on each of its elements for every iteration. Data from our Plant Scanner provided the most recent challenge to the software's capabilities, with 140777 voxels and 342784 LORs. Though LZO compression allowed us to significantly reduce the file size of the Plant Scanner system matrix, the dimensions of our biggest scanner, the BNL-UPenn System, may be too large for our current method of reconstruction.

To reconstruct data acquired from the BNL-UPenn System, we began using Software for Tomographic Image Reconstruction (STIR), an open source C++ library for 3D PET reconstruction[81]. Developed by Thielemans et al, it provides an array of analytical and iterative reconstruction algorithms that can be used on user-defined scanner geometries. Particularly useful for the BNL-UPenn System, included in the software package is a variation of Siddon's algorithm, allowing for the ray-tracing method in probability matrix operations. Using the ray-tracing method, the physical effects normally modelled by the system matrix, such as scanner geometry and attenuation, are calculated on-the-fly. The user can then reconstruct list-mode or sinogram data from any scanner, provided that the dimensions of the scanner are included.

We have currently used the ordered subset version of the one step late algorithm (OSMAPOSL) provided by STIR to reconstruct BNL-UPenn data. The one step late method is an expansion of MAP reconstruction, in which the partial derivative of the prior energy function is evaluated for the current image estimate in every iteration. Results have been promising, and in the future, it is possible to extend the use of STIR to all of our scanners, thus prompting a reevaluation of the means by which we consider scatter, attenuation, and geometric effects into our data.

4.1.3 SiPM-Based Detector Modules

The image resolution of our scanners is limited by the area of the discrete crystals within the block detectors. Using scintillators with finer crystal elements however would require the use of photodetectors that are capable of reading out such an array. Our group has investigated the possible use of SiPMs for medical imaging, which can potentially be coupled to a 128 LYSO crystal array and 128 channel ASIC.

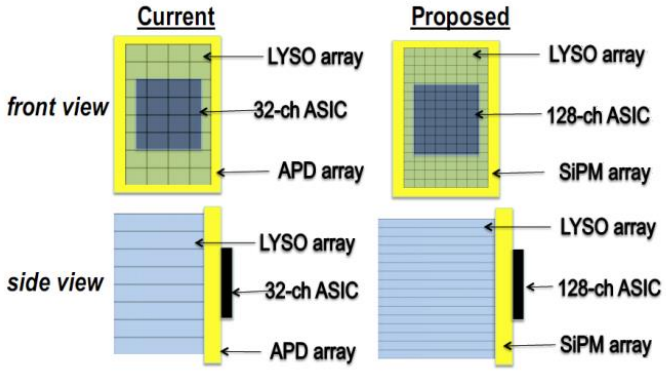

Figure 89: (Left) Current APD-based detector module and (Right) proposed SiPM-based detector module[82]

AdvanSiD has developed an 8x8 SiPM array with 1.5 mm pixel pitch that may be used in an updated RatCAP. This new system could have improved timing, and a spatial resolution below 1 mm. Initial tests have been conducted on a 4x4 LYSO SiPM detector, and results have shown the detector capable of resolving elements distanced 1.5 mm apart. Further tests are required for optimizing energy and time resolution.

4.2 DISCUSSION

In an effort to update our collection of PET scanners, quantitative data acquisition and processing methods that are robust and unified across all systems have been developed. The development of these techniques have been followed with the full characterization of the BNL imaging system for plant science. A summary of the improvements to our systems are shown here:

Hardware Upgrade: RatCAP and PET Insert have been upgraded to the tether-less flex circuit, and a second RatCAP for awake animal imaging has been assembled. Development on the BNL-UPenn System is complete, and with it, the new version of the time stamp and signal processing module. Adapter boards allow new TSPMs to work will all systems. Tethered RatCAP flex circuits are now used for Wrist Scanner, which has a dedicated TSPM adapter board and GPIB controller for LLD control.

Faster and more stable: The time resolution of our system clock has been improved to 2 ns, and removes the unreliable method of dividing timestamps into course and fine elements. Cross talk between channels, which was common in past systems, has been effectively removed with a simplified system of phase selection. The unstable G-Link system has been replaced with UDP communication using gigabit Ethernet, which has consistently run without downtime.

Capable of handling more data and integrating different kinds of data: With the development of the BNL-UPenn Scanner, our system needed the ability to receive data from four TSPMs. Our new data acquisition software RCDAQ is capable of receiving data packets from multiple sources and incorporating them into a single data stream. Different data can include calibration files, positioning photos, and scan metadata, such as cardiac or RF interference gating, count rates, packet and single event tracking numbers, and live time. This is possible due to the event handling system, developed at PHENIX, which allows processing software to identify data sources for each packet and maintain data integrity. Image stitching software can combine images from various scanning positions to extend the axial field of view.

Expandable to all systems, current and future: New software has been written for every aspect of the PET data processing chain for every scanner, including coincidence processing, threshold scan processing, calibration and efficiency correction calculation, sinogram

bin and time correction lookup table writers, and image editing. Scanner compatibility defined by easily appended classes and lookup tables.

Portable to other systems: Software works with different versions of Linux (Gentoo, Ubuntu, Red Hat, Scientific Linux), and is developed for use on data acquisition computers and servers.

Observable in realtime: Our new software uses the Pmonitor framework, which allows for the monitoring of data processing, both for data saved to disk and for incoming data from our scanners. This gives the user the ability to see projections and sinograms of the imaged subject formed in realtime, and to review past scans by playing back the acquisition process from file. Relevant metrics, such as coincidence rate, singles rate, and channel performance are reported in the monitor.

Easy, customizable, and reproducible: A graphical user interface have been written for controlling and customizing scanner calibration, data acquisition, coincidence processing, image reconstruction, realtime monitoring, and troubleshooting. Parallel processing across multiple processing units is available for image reconstruction.

Consistent in performance: Compressed, sparse system matrix format and image reconstruction software have been made compatible with data from all scanners. Efficiency correction software provides verifiable normalization for image reconstruction, with the ability to quickly edit for malfunctioning channels. Time correction software uses minimum number of crystal pairs for determining time-zero delay factors.

Transparent in its limitations: Transmission based deadtime, including transmission gap between UDP packets and lost packets, is calculated and reported in realtime. Singles-based gating is incorporated into the coincidence processing chain, and gating based deadtime is reported.

Comprehensive: Log files and header files for sinograms and images include all scan information and PET metrics, including data rates and deadtime at given time intervals throughout the scan. Header files are compatible with ASIPro, PMOD, and other commercial imaging viewing and editing software.

Our Plant Scanner was characterized and shows the following specifications: When using a lower level energy discriminator of 360 keV, and a timing window of 10 ns, the absolute sensitivity of the system is 0.6% at the center of the field of view. Its energy resolution and time resolution are 15.8% and 8 ns respectively. Using our MLEM image reconstruction software, we achieve a spatial resolution of 1.8 mm FWHM. The peak noise equivalent count rate is 25 kcps at 1.2 mCi. With activity filling the field of view, the system can handle 1 mCi with 6% deadtime; the gigabit Ethernet connection can acquire data up to 75 MB of singles data per second without significant losses (2.6% deadtime attributable to packet loss). Calibration factors have been applied to our data, which allow for the determination of activity concentration values across the image area during analysis.

With the development of new data acquisition and processing methods, we have created a series of tools ready for the challenges of functional medical imaging. Reliable and user friendly, our scanners have been used in a wide range of disciplines, from behavioral neuroscience to evolutionary biology. We have shown its use in investigating the lymphatic pathways of mice, dopaminergic transmission in rats, metabolic activation of birds in flight, and growth in pea plants. Our software has been packaged and ported to numerous laboratories, where it handles the path from raw data to image analysis independently. Able to incorporate different image modalities, and applicable to a variety of research methods, our scanners and software are flexible and viable for the imaging scientist, in the clinical or research setting.

Bibliography

1. Casey, M., Nutt, R. (1986) A multislice two-dimensional BGO detector system for PET, IEEE Trans. Nucl. Sci., vol. 33, no. 1, pp. 760–763. © 1986 IEEE
2. Carrier, C., Lecomte, R. (1990) Timing performance of scintillators read out by silicon avalanche photodiodes, Nucl. Instrum. Methods, vol. A299, pp. 115–118.
3. Pratte, J-F., et al. "The RatCAP front-end ASIC." *Nuclear Science, IEEE Transactions on* 55.5 (2008): 2727-2735. © 2008 IEEE
4. Schulz, Daniela, et al. "Simultaneous assessment of rodent behavior and neurochemistry using a miniature positron emission tomograph." *Nature methods* 8.4 (2011): 347-352.
5. Junnarkar, S. S., et al. (2005). An FPGA-based, 12-channel TDC and digital signal processing module for the RatCAP scanner. Nuclear Science Symposium Conference Record, 2005 IEEE, IEEE. © 2005 IEEE
6. Maramraju, S. H., et al. (2011). "Small animal simultaneous PET/MRI: initial experiences in a 9.4 T microMRI." Physics in Medicine and Biology 56(8): 2459.
7. Budassi, M., et al. "First results from the BNL/Penn PET-MRI system for whole body rodent imaging at 9.4 T." *Nuclear Science Symposium and Medical Imaging Conference (NSS/MIC), 2012 IEEE*. IEEE, 2012. © 2012 IEEE
8. Budassi, Michael, et al. "Imaging performance of the BNL PET imaging system for plant science." *Nuclear Science Symposium and Medical Imaging Conference (NSS/MIC), 203 IEEE*. IEEE, 2013. © 2013 IEEE
9. Ravindranath, B., et al. (2009). 3D tomographic wrist scanner for non-invasive determination of input function. Nuclear Science Symposium Conference Record (NSS/MIC), 2009 IEEE, IEEE. © 2009 IEEE
10. Ravindranath, B., et al. "Results from prototype II of the BNL simultaneous PET-MRI dedicated breast scanner." *Nuclear Science Symposium Conference Record (NSS/MIC), 2009 IEEE*. IEEE, 2009. © 2009 IEEE
11. Park, S-J., et al. "Digital coincidence processing for the RatCAP conscious rat brain PET scanner." *Nuclear Science, IEEE Transactions on* 55.1 (2008): 510-515. © 2008 IEEE
12. Eckelman, W. C. (2009). "Unparalleled contribution of technetium-99m to medicine over 5 decades." JACC: Cardiovascular Imaging 2(3): 364-368.

13. Patton, D. D. (2003). "The birth of nuclear medicine instrumentation: Blumgart and Yens, 1925." Journal of Nuclear Medicine 44(8): 1362-1365.
14. L'Annunziata, M. F. (2012). Handbook of radioactivity analysis, Academic Press.
15. Jacob, A. and L. Nourafchan (2013). "Radiological engineering in brain dysfunction imaging processes and neuro informatics." Journal of nuclear medicine & radiation therapy 4: 157.
16. Conti, P. S., et al. (1996). "PET and [18 F]-FDG in oncology: a clinical update." Nuclear medicine and biology 23(6): 717-735.
17. Zipursky, R. B., et al. (2007). "PET and SPECT imaging in psychiatric disorders." Canadian Journal of Psychiatry 52(3): 146.
18. Badawi, R. D., et al. (1999). "Randoms variance reduction in 3D PET." Physics in Medicine and Biology **44**(4): 941.
19. Hoffman, E. J., et al. (1981). "Quantitation in positron emission computed tomography: 4. Effect of accidental coincidences." Journal of computer assisted tomography **5**(3): 391-400.
20. Ollinger, J. M. (1995). "Detector efficiency and Compton scatter in fully 3D PET." Nuclear Science, IEEE Transactions on **42**(4): 1168-1173. © 1995 IEEE
21. Bushberg, J. T. and J. M. Boone (2011). The essential physics of medical imaging, Lippincott Williams & Wilkins.
22. Maher, K. (2001) "The Compton Effect." <https://en.wikibooks.org/wiki/Basic_Physics_of_Digital_Radiography/The_Patient#/media/File:ComptonEffect.jpg>
23. Nelson, G. and D. Reilly (1991). "Gamma-ray interactions with matter." Passive Nondestructive Analysis of Nuclear Materials, Los Alamos National Laboratory, NUREG/CR-5550, LAUR-90-732: 27-42.
24. Cherry, S. R., et al. (2012). Physics in nuclear medicine, Elsevier Health Sciences.
25. Menefee, J., et al. (1967). "Sodium Activated Cesium Iodide as a Gamma Ray and Charged Particle Detector." Nuclear Science, IEEE Transactions on **14**(1): 464-467. © 1967 IEEE
26. Wernick, M. N. and J. N. Aarsvold (2004). Emission tomography: the fundamentals of PET and SPECT, Academic Press.
27. Knoll, G. F. (2010). Radiation detection and measurement, John Wiley & Sons.
28. Bailey, D. L., et al. (2005). Positron emission tomography, Springer.

29. Ramirez, R., et al. (2012). New PMT-Quadrant-Sharing shallow block detector development for high performance TOF PET applications. Nuclear Science Symposium and Medical Imaging Conference (NSS/MIC), 2012 IEEE, IEEE. © 2012 IEEE
30. Greenfield, Josh. "Detectors." *UCDavis Chemwiki*. <http://chemwiki.ucdavis.edu/Analytical_Chemistry/Instrumental_Analysis/Spectrometer/Detectors/Detectors> (Link to license: <http://creativecommons.org/licenses/by-nc-sa/3.0/us/legalcode>)
31. Roncali, E. and S. R. Cherry (2011). "Application of silicon photomultipliers to positron emission tomography." Annals of Biomedical Engineering **39**(4): 1358-1377.
32. Mikhantiev, E. (2009) "APD." <https://commons.wikimedia.org/wiki/File:APD.png>
33. Adam, L.-E., et al. (2000). "Energy-based scatter correction for 3-D PET scanners using NaI (Tl) detectors." Medical Imaging, IEEE Transactions on **19**(5): 513-521. © 2000 IEEE
34. Kataoka, J., et al. (2009). Versatile APD-based PET modules for high resolution, fast medical imaging. Nuclear Science Symposium Conference Record (NSS/MIC), 2009 IEEE, IEEE. © 2009 IEEE
35. Leahy, R. M. and J. Qi (2000). "Statistical approaches in quantitative positron emission tomography." Statistics and Computing 10(2): 147-165.
36. Kostmo. (2008) "Radon Transform." <https://en.wikipedia.org/wiki/Radon_transform>
37. Bendriem, B. and D. W. Townsend (2013). The theory and practice of 3D PET, Springer Science & Business Media.
38. Thompson, C., et al. (2005). "Under-sampling in PET scanners as a source of image blurring." Nuclear Instruments and Methods in Physics Research Section A: Accelerators, Spectrometers, Detectors and Associated Equipment 545(1): 436-445.
39. Fahey, F. H. (2002). "Data acquisition in PET imaging." Journal of nuclear medicine technology 30(2): 39-49.
40. Conti, M. (2011). "Focus on time-of-flight PET: the benefits of improved time resolution." European journal of nuclear medicine and molecular imaging **38**(6): 1147-1157.
41. Smith, S. W. (1997). Special Imaging Techniques. The scientist and engineer's guide to digital signal processing.

42. Maher, K. (2006) “Demonstration of Simple Back Projection” <https://en.wikibooks.org/wiki/Basic_Physics_of_Digital_Radiography/The_Applications#/media/File:NM19_3.gif>
43. Lyra, M. and A. Ploussi (2011). "Filtering in SPECT image reconstruction." Journal of Biomedical Imaging 2011: 10.
44. Maher, K. (2006) “A ramp function and a Butterworth function (of variable order and cut-off frequency) are multiplied to form the Fourier filter used in the FBP process.” <https://en.wikibooks.org/wiki/Basic_Physics_of_Nuclear_Medicine/Fourier_Methods#/media/File:NM16_14.gif>
45. Shepp, L. A. and Y. Vardi (1982). "Maximum likelihood reconstruction for emission tomography." Medical Imaging, IEEE Transactions on **1**(2): 113-122. © 1982 IEEE
46. Lange, K. and R. Carson (1984). "EM reconstruction algorithms for emission and transmission tomography." Journal of computer assisted tomography **8**(2): 306-316.
47. Qi, J. and R. M. Leahy (2006). "Iterative reconstruction techniques in emission computed tomography." Physics in Medicine and Biology **51**(15): R541.
48. Leahy, R. and R. Clackdoyle (2010). Computed Tomography. Handbook of image and video processing. A. C. Bovik, Academic Press.
49. Hudson, H. M. and R. S. Larkin (1994). "Accelerated image reconstruction using ordered subsets of projection data." Medical Imaging, IEEE Transactions on **13**(4): 601-609. © 1994 IEEE
50. Levitan, E. and G. T. Herman (1987). "A maximum a posteriori probability expectation maximization algorithm for image reconstruction in emission tomography." Medical Imaging, IEEE Transactions on **6**(3): 185-192. © 1987 IEEE
51. Budinger, T. F. (1998). PET instrumentation: what are the limits? Seminars in nuclear medicine, Elsevier.
52. Cherry, Simon R., and Magnus Dahlbom. "PET: physics, instrumentation, and scanners." *PET*. Springer New York, 2006.
53. Levin, C. S. and E. J. Hoffman (1999). "Calculation of positron range and its effect on the fundamental limit of positron emission tomography system spatial resolution." Physics in Medicine and Biology 44(3): 781.

54. Saha, G. B. (2010). Performance characteristics of PET Scanners. Basics of PET Imaging, Springer: 97-116.
55. Moisan, C., et al. (1997). Segmented LSO crystals for depth-of-interaction encoding in PET. Nuclear Science Symposium, 1997. IEEE, IEEE. © 1997 IEEE
56. Rahmim, A., et al. (2013). "Resolution modeling in PET imaging: Theory, practice, benefits, and pitfalls." Medical physics **40**(6): 064301.
57. Bai, B., et al. (2002). "Model-based normalization for iterative 3D PET image reconstruction." Physics in Medicine and Biology **47**(15): 2773.
58. Bailey, D. L., et al. (1996). "An investigation of factors affecting detector and geometric correction in normalization of 3-D PET data." Nuclear Science, IEEE Transactions on **43**(6): 3300-3307. © 1996 IEEE
59. Badawi, R. D. and P. K. Marsden (1999). "Developments in component-based normalization for 3D PET." Physics in Medicine and Biology 44(2): 571.
60. Goertzen, A. L., et al. (2012). "NEMA NU 4-2008 comparison of preclinical PET imaging systems." Journal of Nuclear Medicine **53**(8): 1300-1309.
61. Tai, Y.-C., et al. (2002). MicroPET II: an ultra-high resolution small animal PET system. Nuclear Science Symposium Conference Record, 2002 IEEE, IEEE. © 2002 IEEE
62. Judenhofer, M. S., et al. (2008). "Simultaneous PET-MRI: a new approach for functional and morphological imaging." Nature medicine 14(4): 459-465.
63. Kume, T., et al. (1997). "Uptake and transport of positron-emitting tracer (18 F) in plants." Applied radiation and isotopes **48**(8): 1035-1043.
64. Jahnke, S., et al. (2009). "Combined MRI–PET dissects dynamic changes in plant structures and functions." The Plant Journal 59(4): 634-644.
65. Streun, M., et al. (2007). PlanTIS: a positron emission tomograph for imaging 11 C transport in plants. Nuclear Science Symposium Conference Record, 2007. NSS'07. IEEE, IEEE. © 2007 IEEE
66. ROOT Homepage <https://root.cern.ch/drupal/>
67. Purschke M.L., et al. Readout technologies for the BNL-UPenn MRI Compatible PET scanner for rodents. In Nuclear Science Symposium and Medical Imaging Conference (NSS/MIC), 2011 IEEE, pages 617 –620, Oct. 2011. © 2011 IEEE

68. Purschke M.L., "Online and Offline Computing systems in the PHENIX experiment." *arXiv preprint hep-ex/0305103* (2003).
69. Purschke, M. L. "The DAQ and online system of the PHENIX experiment at RHIC." *Nuclear Science Symposium Conference Record, 2003 IEEE*. Vol. 2. IEEE, 2003. © 2003 IEEE
70. Purschke ML, B.M., Cao T., Fried J., Ravindranath B., Schlyer D., Stoll S.P., Vaska P., Woody C., 2012. Managing the Computing-Intensive Image Reconstruction for the BNL Plant PET Scanner. In: IEEE Nuclear Science Symposium and Medical Imaging Conference, Anaheim, CA. © 2012 IEEE
71. ASI Pro VM™ Micro PET Analysis software quick guide. <http://mips.stanford.edu/aboutus/facilities/clark/img_quant_resource/pdfs/ASI_Pro_VM-quick_guide.pdf>
72. PMOD Home Page < https://www.pmod.com/web/>
73. University of Washington, SimSET Home Page <http://depts.washington.edu/simset/html/simset_main.html>
74. Velmex (2013) "Motorized BiSlide Assemblies" <http://www.velmex.com/bislide/motor_bislide.html>
75. NEMA (2008). NEMA Standards Publication NU 4 – 2008: Performance Measurements of Small Animal Positron Emission Tomographs.
76. Gu, Z., et al. "NEMA NU-4 performance evaluation of PETbox4, a high sensitivity dedicated PET preclinical tomograph." *Physics in medicine and biology* 58.11 (2013): 3791.
77. Thanos, P. K., et al. (2015). "A pharmacokinetic model of oral methylphenidate in the rat and effects on behavior." Pharmacology Biochemistry and Behavior **131**: 143-153.
78. Tziortzi, A. C., et al. (2011). "Imaging dopamine receptors in humans with [11 C]-(+)-PHNO: dissection of D3 signal and anatomy." NeuroImage **54**(1): 264-277.
79. Rabiner, E. A., et al. (2009). "In vivo quantification of regional dopamine-D3 receptor binding potential of (+)-PHNO: Studies in non-human primates and transgenic mice." Synapse **63**(9): 782-793.
80. Okauchi, T., et al. (2001). "Effect of endogenous dopamine on extrastriatal [11C] FLB 457 binding measured by PET." Synapse **41**(2): 87-95.
81. Thielemans, K., et al. (2012). "STIR: software for tomographic image reconstruction release 2." Physics in Medicine and Biology **57**(4): 867.

82. Kapoor, B. (2013). Characterization of Silicon Photomultipliers for Positron Emission Tomography Imaging. Biomedical Engineering, Stony Brook University. **Master of Science**.
83. Stevens, W. R., et al. (2004). UNIX network programming, Addison-Wesley Professional.
84. Bin, Z. (2012). "An Efficient Implementation of PET Image Reconstruction from List-Mode Data." Procedia Engineering **29**: 3403-3407.
85. Hamamatsu Photonics, K. (2006). "Si APD Array S8550."
86. Iliff, J. J., et al. (2013). "Brain-wide pathway for waste clearance captured by contrast-enhanced MRI." The Journal of clinical investigation **123**(123 (3)): 1299-1309.
87. Derenzo, S. E., et al. (1975). "Analytical study of a high-resolution positron ring detector system for transaxial reconstruction tomography." Journal of nuclear medicine: official publication, Society of Nuclear Medicine **16**(12): 1166-1173.
88. Moon, T. K. (1996). "The expectation-maximization algorithm." Signal processing magazine, IEEE **13**(6): 47-60. © 1996 IEEE
89. Daube-Witherspoon, M. E., et al. (2002). "PET performance measurements using the NEMA NU 2-2001 standard." Journal of Nuclear Medicine **43**(10): 1398-1409.
90. Cañadas, M., et al. (2011). "NEMA NU 4-2008 performance measurements of two commercial small-animal PET scanners: ClearPET and rPET-1." Nuclear Science, IEEE Transactions on **58**(1): 58-65. © 2011 IEEE
91. Beyer, T., et al. (2011). "The future of hybrid imaging—part 3: PET/MR, small-animal imaging and beyond." Insights into imaging 2(3): 235-246.
92. Hamamatsu Photonics, K. (2007). "Photomultiplier tubes: Basics and applications." Edition 3a.
93. PerkinElmer (2006) "Avalanche Photodiode: A User Guide, Understanding Avalanche Photodiode for Improving System Performance."
94. Kriplani, A., et al. "Non-invasive and selective measurement of the arterial input function using a PET wrist scanner." *Nuclear Science Symposium Conference Record, 2006. IEEE*. Vol. 6. IEEE, 2006. © 2006 IEEE